

Accepted to ApJS 2015 June 27

The Brown Dwarf Kinematics Project (BDKP). IV. Radial Velocities of 85 Late-M and L dwarfs with MagE

Adam J. Burgasser¹, Sarah E. Logsdon², Jonathan Gagné³, John J. Bochanski⁴, Jacqueline K. Faherty^{5,6,7}, Andrew A. West⁸, Eric E. Mamajek⁹, Sarah J. Schmidt¹⁰, and Kelle L. Cruz^{6,11,12}

ABSTRACT

Radial velocity measurements are presented for 85 late M- and L-type very low mass stars and brown dwarfs obtained with the Magellan Echellette (MagE) spectrograph. Targets primarily have distances within 20 pc of the Sun, with more distant sources selected for their unusual spectral energy distributions. We achieved precisions of $2\text{--}3\text{ km s}^{-1}$, and combined these with astrometric and spectrophotometric data to calculate UVW velocities. Most are members of the thin disk of the Galaxy, and velocity dispersions indicate a mean age of 5.2 ± 0.2 Gyr for sources within 20 pc. We find significantly different kinematic ages between late-M dwarfs (4.0 ± 0.2 Gyr) and L dwarfs (6.5 ± 0.4 Gyr) in our sample that are contrary to predictions from prior simulations. This difference appears to be driven by a dispersed population of unusually

¹Center for Astrophysics and Space Science, University of California San Diego, La Jolla, CA, 92093, USA; aburgasser@ucsd.edu

²Department of Physics and Astronomy, UCLA, 430 Portola Plaza, Box 951547, Los Angeles, CA 90095-1547, USA

³Institute for Research on Exoplanets (iREx), Université de Montréal, Département de Physique, C.P. 6128 Succ. Centre-ville, Montréal, QC H3C 3J7, Canada

⁴Rider University, 2083 Lawrenceville Road, Lawrenceville, NJ 08648, USA

⁵Department of Terrestrial Magnetism, Carnegie Institution of Washington, Washington, DC 20015, USA

⁶Department of Astrophysics, American Museum of Natural History, Central Park West at 79th Street, New York, NY 10034, USA

⁷Hubble Postdoctoral Fellow

⁸Department of Astronomy, Boston University, 725 Commonwealth Ave Boston, MA 02215 USA

⁹Department of Physics & Astronomy, University of Rochester, Rochester, NY 14627, USA

¹⁰Department of Astronomy, Ohio State University, 140 West 18th Avenue, Columbus, OH 43210, USA

¹¹Department of Physics and Astronomy, Hunter College, 695 Park Avenue, New York, NY10065, USA

¹²Department of Physics, Graduate Center, City University of New York, 365 Fifth Avenue, New York, NY 10016, USA

blue L dwarfs which may be more prevalent in our local volume-limited sample than in deeper magnitude-limited surveys. The L dwarfs exhibit an asymmetric U velocity distribution with a net inward flow, similar to gradients recently detected in local stellar samples. Simulations incorporating brown dwarf evolution and Galactic orbital dynamics are unable to reproduce the velocity asymmetry, suggesting non-axisymmetric perturbations or two distinct L dwarf populations. We also find the L dwarfs to have a kinematic age-activity correlation similar to more massive stars. We identify several sources with low surface gravities, and two new substellar candidate members of nearby young moving groups: the astrometric binary DENIS J08230313–4912012AB, a low-probability member of the β Pictoris Moving Group; and 2MASS J15104786-2818174, a moderate-probability member of the 30-50 Myr Argus Association.

Subject headings: stars: low-mass, brown dwarfs; stars: kinematics and dynamics; methods: statistical; techniques: radial velocities

1. Introduction

Very low-mass (VLM) stars and brown dwarfs with masses $\lesssim 0.1 M_{\odot}$ comprise a significant fraction of stars in our Galaxy ($\gtrsim 20\%$; Chabrier 2003; Bochanski et al. 2010). Their ubiquity and extremely long lifetimes make them an important probe of Galaxy structure, chemical evolution and star formation history (Burgasser 2004; Bochanski et al. 2007a; Pirzkal et al. 2009; Pineda et al. 2013). However, the low luminosities and temperatures of these M, L, T and Y dwarfs (Kirkpatrick 2005), and the steady cooling of substellar VLM dwarfs over time, has made it difficult to identify and study them in statistically significant numbers. Fortunately, the completion of wide-field red-optical and infrared sky surveys such as the DEep Near-Infrared Survey of the Southern Sky (DENIS; Epchtein et al. 1997), the Two Micron All Sky Survey (2MASS; Skrutskie et al. 2006), the Sloan Digital Sky Survey (SDSS; York et al. 2000), the Canada-France Hawaii Telescope Legacy Survey (CFHTLS; Delorme et al. 2008), and United Kingdom Infrared Telescope Deep Sky Survey (UKIDSS; Lawrence et al. 2007); and the ongoing Wide-field Infrared Survey Explorer (WISE; Wright et al. 2010), Panoramic Survey Telescope and Rapid Response System (Pan-STARRS; Kaiser et al. 2002), and Visible and Infrared Survey Telescope for Astronomy (VISTA; Emerson et al. 2004) have uncovered roughly 10,000 VLM dwarfs within 100 pc of the Sun¹. The detector technologies enabling these surveys have also led to advances in spectroscopic instrumentation, allowing detailed characterization of spectral energy distributions and corresponding physical parameters for increasingly larger samples of VLM dwarfs (e.g., Reid et al. 2008; Schmidt et al. 2010; West et al. 2011; Kirkpatrick et al. 2012).

¹Current compilations are maintained by C. Gelino at <http://dwarfarchives.org> and J. Gagne at <https://jgagneastro.wordpress.com/list-of-ultracool-dwarfs>.

Characterizing VLM dwarfs as a population relies on accurate measures of their individual characteristics, including kinematics. While most stars in the disk of the Milky Way form in the mid-plane, with Galactic orbits similar to that of the Sun (low inclination, low eccentricity), dynamical encounters with giant molecular clouds, spiral structure and other gravitational potential gradients scatter stars stochastically (Spitzer & Schwarzschild 1953; Toomre 1964; Junqueira et al. 2013). Individual orbits may be chaotic, but the population as a whole evolves toward greater velocity dispersion over time (Wielen 1977). The age- velocity dispersion relation has been used extensively in studies of Galactic star formation history with nearby main sequence stars (e.g., Dehnen & Binney 1998; Binney et al. 2000; Aumer & Binney 2009). Stellar kinematics also segregate large-scale Galactic populations—the thin disk, thick disk and halo—which trace Galactic structure, formation history and chemical enrichment (e.g., Gilmore & Reid 1983; Reid & Majewski 1993; Carollo et al. 2008). Young moving groups (YMGs) near the Sun can also be revealed by coherently moving stars with common spectral signatures of low surface gravity or abundance patterns (e.g., Zuckerman & Song 2004; López-Santiago et al. 2006; Torres et al. 2006; Gagné et al. 2014). Finally, periodicity in motion identifies low-mass companions that can be used to make direct mass measurements and test substellar/exoplanet evolutionary models (Martin et al. 1999; Dupuy et al. 2009a; Konopacky et al. 2010; Sahlmann et al. 2013).

Full characterization of the three-dimensional motions of VLM dwarfs requires radial velocities (RVs), and hence high resolution spectroscopy, observations which have proven challenging for these faint sources. Only a small fraction of the known VLM population has sufficiently precise ($<5 \text{ km s}^{-1}$) RV measurements necessary for robust membership assignment or RV variability detection (e.g., Tinney & Reid 1998; Reid et al. 2002b; Basri & Reiners 2006; Blake et al. 2007, 2010; Zapatero Osorio et al. 2007; Reiners & Basri 2009; Seifahrt et al. 2010; Tanner et al. 2012). Nevertheless, these studies have identified several remarkable—and in some cases conflicting—kinematic trends among the population. Zapatero Osorio et al. (2007) examined the velocity dispersions for 31 late-M and 21 L and T dwarfs, finding the latter to be less dispersed and hence marginally younger, $1.2_{-0.7}^{+1.1}$ Gyr versus $3.8_{-1.9}^{+2.8}$ Gyr based on the age-dispersion relation of Wielen (1977). This age difference is qualitatively consistent with population synthesis simulations that predict that L dwarfs should be on average younger due to brown dwarf cooling (Burgasser 2004; Allen et al. 2005). However, a large fraction ($\sim 40\%$) of the L and T dwarfs examined in that study were also identified as kinematic members of the 0.4–2 Gyr Hyades Stream, which may have biased their collective ages downward. More recent work by Reiners & Basri (2009); Seifahrt et al. (2010) and Blake et al. (2010), based on precise RV measurements for roughly 150 M and L dwarfs and more accurate application of the Wielen relations, find mean ages of 3 Gyr and 5 Gyr for late-M and L dwarfs, respectively; i.e., the reverse trend. Tangential velocity studies by Faherty et al. (2009) and Kirkpatrick et al. (2010), and a larger but lower-precision RV sample by Schmidt et al. (2010), find equivalent ages for M, L and T dwarfs, of order 3–8 Gyr, with no statistically significant difference.

Faherty et al. (2009) and Schmidt et al. (2010) also report color-dependent trends in VLM dwarf kinematics, with sources identified as unusually blue in near-infrared colors being more

widely dispersed than those with unusually red colors. These differences were attributed to age and/or metallicity effects, in particular increased collision-induced H₂ absorption in the atmospheres of sources with high surface gravities and/or subsolar metallicities (cf. Burgasser et al. 2008; Jameson et al. 2008;Looper et al. 2008). However, Kirkpatrick et al. (2010) found no difference in dispersions between red and blue outliers among a proper-motion selected sample of L dwarfs, with both sets appearing to be drawn from an older population.

To address these disagreements in the velocity dispersions and age determinations for the local VLM dwarf population, we report RV measurements for 85 late-type M and L dwarfs based on data obtained with the Magellan Echelle spectrograph (MagE; Marshall et al. 2008). These include measurements for 30 dwarfs without previously reported RVs. In Section 2 we describe our sample, observations, and data reduction methods. In Section 3 we discuss our RV measurement procedures in detail, comparing the accuracy and precision of three common methods. In Section 4 we merge our RV measurements with proper motion and distance determinations to calculate UVW space velocities, and assign membership to Galactic thin and thick disk populations. We also examine velocity dispersions, probability distributions and kinematic ages for the full sample and subsamples based on spectral class, color and activity. In Section 5 we focus on the distinct velocity distributions of M and L dwarfs in our sample, and use population synthesis plus orbit simulations in an attempt to reproduce the asymmetries in the *U* velocity distribution of the latter. In Section 6 we consider kinematic and spectroscopic evidence for association in nearby YMGs, and report two new brown dwarf candidate members. In Section 7 we highlight additional individual sources of interest in detail. Results are summarized in Section 8.

2. Observations

2.1. Sample

Our observational sample is summarized in Table 1. We initially selected 85 late-type dwarfs with published optical spectral types M7 through L5, primarily from the Palomar/MSU Survey (Reid et al. 1995; Hawley et al. 1996; Reid et al. 2002a); the 2MASS surveys of Kirkpatrick et al. (1999, 2000); Gizis (2002); Cruz et al. (2003, 2007) and Reid et al. (2008); the SDSS surveys of Bochanski et al. (2005); West et al. (2008, 2011) and Schmidt et al. (2010); the DENIS surveys of Delfosse et al. (1999); Martín et al. (1999); Kendall et al. (2004, 2007) and Phan-Bao et al. (2008); and other individual discoveries. The majority of our sample were selected to have declinations $\delta \leq 25^\circ$ (Figure 1) and distances $d \lesssim 20$ pc, the latter based on either astrometric parallax measurements (Tinney et al. 1995; van Altena et al. 1995; Dahn et al. 2002; Costa et al. 2005, 2006; Henry et al. 2006; Andrei et al. 2011; Faherty et al. 2012; Dieterich et al. 2014) or spectrophotometric distance estimates based on 2MASS *J*-band photometry and the M_J /spectral type relation of Cruz et al. (2003). Sources within 20 pc (1σ) comprise 82% of our sample. Fifteen sources are at larger distances, most due to previously underestimated distances (e.g., due to multiplicity, misclas-

sification), but several were specifically targetted due to their unusual spectral features indicative of surface gravity, metallicity or cloud effects. There were also several well-resolved binaries selected (e.g., J2200–3038AB²) and sources with unusually large tangential velocities (e.g., J0923+2340). We emphasize that while our sample was primarily designed to be volume-limited, it is not volume-complete. Space density estimates from Cruz et al. (2007) predict \sim 160 late-M dwarfs and \sim 125 L dwarfs within 20 pc, so the 70 sources in our sample satisfying this distance limit represents \sim 25% of the total local population. Figure 2 displays a breakdown of our sample by spectral type (based on updated classifications; see below); 56% are late-type M dwarfs, 44% are L dwarfs. We also display the 2MASS $J - K_s$ colors of our targets as compared to the median color relations of Schmidt et al. (2010) and West et al. (2011) based on SDSS sources. There appears to be a systematic offset in the $J - K_s$ colors of our sample relative to these surveys, with our M dwarfs being on average redder and our L dwarfs being on average bluer. The red offset in our M dwarfs is likely due to our more local sample, as the M dwarfs from West et al. (2011) extend to $>$ 100 pc above/below the Galactic disk, and are likely to be on average more metal-poor. The blue color offset for our L dwarfs, however, is unclear. We compiled published proper motions and tangential velocities, or in the absence of a measurement compared multi-epoch astrometry between 2MASS and WISE, yielding typical precisions of 5–15 mas yr⁻¹; see Gagné et al. (2015) for details.

As of March 2015, 43 sources in our sample had RV measurements reported in the literature with precisions $\sigma_{RV} \leq 3$ km s⁻¹ (Tinney & Reid 1998; Mohanty & Basri 2003; Reiners & Basri 2009; Blake et al. 2010; Gálvez-Ortiz et al. 2010; Seifahrt et al. 2010; Tanner et al. 2012); these values are listed in Table 1. We made use of these prior measurements in our RV measurement analysis (Section 3.3).

2.2. MagE Observations

All sources were observed with the MagE spectrograph, mounted on the Magellan 6.5m Landon Clay Telescope at Las Campanas Observatory. A complete observing log is given in Table 2. Data were obtained in 15 nights over a 2.5-year period (November 2008 through March 2011) in a variety of seeing and weather conditions. We used the 0''.7 slit aligned with the parallactic angle, providing 3200–10050 Å spectroscopy at an average resolution $\lambda/\Delta\lambda \approx 4100$ ($\Delta RV = 73$ km s⁻¹) and dispersion of \sim 0.5 Å pixel⁻¹ at 6000 Å. Exposure times varied according to source brightness and weather conditions, and ranged from 150–3600 s. Most sources were observed in a single exposure, although a handful were observed in multiple exposures or over multiple nights to improve data quality. In addition to the target, we obtained nightly observations of spectrophotometric standards from Hamuy et al. (1994) for flux calibration. ThAr lamps were observed after each source observation for wavelength calibration, and internal quartz and dome flat field lamps were obtained

²Source identifications in the text are given in shorthand notation based on the sexagesimal right ascension and declination, Jhhmm \pm ddmm. Full source names and coordinates are listed in Table 1.

on each night for pixel response calibration. Data were reduced using the MASE reduction pipeline (Bochanski et al. 2009), following standard procedures for order tracing, flat field correction, wavelength calibration (including correction to heliocentric motion), optimal source extraction, order stitching, and flux calibration. We did not perform any correction for telluric absorption on these data, which caused a problem for the flux calibration for several of the spectra around the 7500–7600 Å O₂ telluric band, which resides near an echelle order boundary. This region is ignored in subsequent analyses. We also note that the spectrum of J0148–3024 was affected by poor flux calibration in the 8300–8700 Å band, and the region is also ignored in the analysis of this source.

2.3. Spectral Features and Classification

The red optical components of our spectra (6000–9000 Å) are shown in Figure 3. The data are generally of high quality, with signal-to-noise ratios (S/N) of 20–200 at 8600 Å (mean S/N = 60). We see all of the characteristic features of late-type dwarfs, including strong TiO, VO, CaH and metal line absorption in the late-M dwarfs. The features fade in the L dwarf spectra and FeH, CrH, and various alkali lines emerge, including the heavily pressure-broadened Na I and K I doublets centered at 5500 Å and 7700 Å, respectively (Kirkpatrick et al. 1991, 1999; Martín et al. 1999).

We revisited the optical classifications for all of our sources by comparing directly to the SDSS M and L dwarf templates from Bochanski et al. (2007b) and Schmidt et al. (2014) over the 7100–8800 Å range (excluding the 7500–7600 Å O₂ band). The best-match template ($T(\lambda)$) was identified as that with the minimum squared deviation from the observed spectrum ($f(\lambda)$):

$$\sigma^2 = \sum_{\lambda=7100 \text{ \AA}}^{8800 \text{ \AA}} (f(\lambda) - \alpha T(\lambda))^2 \quad (1)$$

where

$$\alpha = \frac{\sum_{\lambda=7100 \text{ \AA}}^{8800 \text{ \AA}} f(\lambda)T(\lambda)}{\sum_{\lambda=7100 \text{ \AA}}^{8800 \text{ \AA}} T(\lambda)^2} \quad (2)$$

is the optimal scale factor. For most of our sample, these classifications are within 1 subtype of those reported in the literature. The six discrepant sources (J0041–5621AB, J0123–6921, J0331–3042, J0641–4322, J0751–2530, J0823–4912AB) were re-examined by eye and the revised classification confirmed. Note that three of these discrepant sources exhibit signatures of low surface gravity, as discussed below.

2.4. Emission and Absorption Line Features

For the majority of our sources, we also detect Balmer line emission, including H α , H β and H γ lines. Figure 4 displays the fraction of sources with detectable H α emission as a function of spectral

type. Similar to previous studies (e.g., Gizis et al. 2000; Kirkpatrick et al. 2000; West et al. 2004, 2008; Schmidt et al. 2007, 2014) we find a decline in the frequency of emission between the late-M dwarfs (96% active) and the L dwarfs (54% active), although a trend with spectral type is difficult to quantify given the relatively small sample.

We computed the relative H α luminosities ($\log_{10} L_{H\alpha}/L_{bol}$) by two methods. First, we used the sources’ 2MASS J magnitudes and mean $i - J$ colors as a function of spectral type from Schmidt et al. (2010) and West et al. (2011) to scale the spectra and convert H α emission into apparent flux units. We then used J -band bolometric corrections from Liu et al. (2010) to compute apparent bolometric fluxes. The bolometric corrections are based on the Mauna Kea Observatory (MKO) filter system (Simons & Tokunaga 2002; Tokunaga et al. 2002), so we computed a spectral type-dependent correction between 2MASS J and MKO J using spectrophotometry from 533 optically-classified M6–L7 dwarfs in the SpeX Prism Library (Burgasser 2014), as described in the Appendix. The ratio of apparent H α flux to apparent bolometric flux yields $\log_{10} L_{H\alpha}/L_{bol}$. As a second approach, we used the spectral type-dependent χ -factor defined by Walkowicz et al. (2004), with updated values from Douglas et al. (2014) and Schmidt et al. (2014). Both methods gave consistent results, and values from the first method are listed in Table 3. As in previous studies, we find that the strength of emission monotonically declines from M7 to L5, ultimately falling below our detection limits. However, two L dwarfs, the L3 J2036+1051 and the L5 J1315–2649AB, stand out as being unusually active. The latter is a “hyperactive” L dwarf observed to have strong H α , alkali line and radio emission (Hall 2002b,a; Gizis 2002; Kirkpatrick et al. 2008; Burgasser et al. 2011, 2013). We also identify J2037–1137 as the only M8 dwarf in our sample to show no sign of H α emission to a stringent limit ($\log_{10} L_{H\alpha}/L_{bol} < -6.7$). Both J2036+1051 and J2037–1137 are discussed further in Section 7.

Table 3 also lists equivalent widths (EWs) for alkali lines observed in the MagE data. Of particular note is Li I absorption detected in the spectra of nine sources, all shown in detail in Figure 5. We confirm the detection of Li I in J0041–5621AB, J0123–6921, J0823–4912, J1139–1159, J1411–2119 and J2045–6332 (Tinney 1998; Mohanty et al. 2003; Reiners & Basri 2009; Gálvez-Ortiz et al. 2014; Sahlmann et al. 2015), and find marginal evidence of absorption previously reported in J0339–3525 (Reiners & Basri 2009). We report the first identification of Li I in the spectra of the M9 dwarfs J0652–2534 and J1510–2818. This line is a key age and mass indicator, as it is only present in cool dwarfs less massive than $0.06 M_\odot$ and/or younger than ~ 200 Myr (Magazzu et al. 1993; Bildsten et al. 1997; Burke et al. 2004). The presence of Li I absorption in the spectra of these dwarfs therefore indicates that they are likely to be young brown dwarfs.

2.5. Low Surface Gravity Indicators

As described in previous studies (e.g., Martín et al. 1999; Kirkpatrick et al. 2008; Cruz et al. 2009; Allers & Liu 2013), young brown dwarfs with low surface gravities and low photospheric

pressures exhibit enhanced TiO and VO absorption, weak metal hydride bands, and weak alkali lines compared to their equivalently-classified field dwarf counterparts. Building on work by Cruz et al. (2009), we quantified these features using the Na-a, Na-b, TiO-b, CrH-a, and FeH-a indices defined in Kirkpatrick et al. (1999), which sample the 8183 Å and 8194 Å Na I doublets, 8400 Å TiO band, and 8580 Å CrH and 8660 Å FeH bands. We defined a new index (VO7900) sampling the 7900 Å VO band as the ratio of integrated flux between 7950–8000 Å over that between 7825–7875 Å. Table 4 lists the mean and standard deviations of these index combinations as a function of spectral type for sources without Li I absorption.

We identified sources in our sample for which alkali or metal-hydride bands are consistently weaker, and VO or TiO bands consistently stronger, than these spectral type means. These sources are listed in Table 5. Five show clear signatures of low surface gravity as compared to SDSS templates (Figure 6). Three of these sources exhibit Li I absorption and three have been identified as candidate kinematic members of the YMGs TW Hydreae (J1139–3159; Gizis 2002) and β Pictoris (J2000–7523, J2045–6332; Gálvez-Ortiz et al. 2010; Gagné et al. 2014). An additional six sources (Figure 7) exhibit weak signatures of low surface gravity. All of these have Li I absorption, and three are previously noted as candidate kinematic members of the Tucana Horologium, Castor and Argus YMGs (Ribas 2003; Gálvez-Ortiz et al. 2010; Gagné et al. 2014). The low-gravity sources are discussed in further detail below.

2.6. Metallicity Indicators

For all of our late-M dwarfs, we computed the metallicity index ζ defined in Lépine et al. (2007). Within our sample, there is very little variation in ζ , with all but one source (the M9.5 J0024–0158; $\zeta = 0.56 \pm 0.03$) falling into the “subdwarf” classification. Even this source is a poor metal-poor candidate given its late spectral type, although it is unusual in its combination of rapid rotation and sporadic (and occasionally flaring) magnetic emission (Basri & Marcy 1995; Reid et al. 1999; Berger 2002; Berger et al. 2010). No H α emission from this source was detected in our data.

3. Radial Velocity Measurements

To obtain the most precise radial velocity measurements for UVW space motion analysis, we examined three different measurement methods. For interested readers, we detail these methods here; final results are summarized in Table 6.

3.1. Line Center Measurements

Our first approach was to measure Doppler shifts for the prominent absorption and emission lines present in the data: K I, Rb I, Na I, Cs I, and H α . Line centers were determined by fitting Gaussian profiles to each line using the IRAF³ routine *splot*, and these were compared to vacuum wavelengths obtained from the National Institute of Standards and Technology (NIST) Atomic Spectra Line database⁴. After rejecting poor line fits, we computed the average and standard deviation of the corresponding velocity shifts (Table 6).

Figure 8 compares our measured line center RVs to literature values for those sources with previous high precision measurements ($\sigma_{RV} \leq 3 \text{ km s}^{-1}$). Overall we find good agreement between these measurements, with a mean offset of $1.0 \pm 4.2 \text{ km s}^{-1}$ (line center measurements are slightly more positive). In only one case, J0517–3349, do we find a significant discrepancy between our measurement ($-36 \pm 7 \text{ km s}^{-1}$) and that reported by Reiners & Basri (2009, 31.4 km s^{-1}), which we attribute to a sign reversal in that study. The median measurement uncertainties from this analysis are 7 km s^{-1} , roughly one-tenth our nominal resolution but still unacceptably large for kinematic analysis.

3.2. Cross-correlation with SDSS Templates

To make better use of the full spectrum, we performed a cross-correlation analysis comparing to two sets of RV standards: the zero-velocity, low-resolution M7–L0 SDSS spectral templates of Bochanski et al. (2007b) and MagE observations of VLM dwarfs with published RV measurements. In both cases, we used the IDL⁵ *xcorl* package (Mohanty & Basri 2003; West & Basri 2009) to cross-correlate spectral pairs over five bands sampling distinct spectral features: H α emission (6500–6600 Å); the 7050 Å TIO absorption band (7150–7250 Å); K I and Rb I doublets (7685–7885 Å); the 8183/8195 Å Na I doublet (8150–8250 Å); and TiO, VO and Cs I absorption (8350–8550 Å). For each source/template pair and spectral region, cross-correlation functions were visually inspected and poor correlations rejected.

For the SDSS template sample, we used the non-active templates to compare against our M7–L0 sources. As the templates have a lower resolution ($\lambda/\Delta\lambda \approx 1800$) than our MagE data, we smoothed the MagE data to an equivalent resolution using a Gaussian kernel and interpolated onto a common wavelength scale. Each source was compared to the template with the equivalent type;

³Image Reduction and Analysis Facility (Tody 1986). IRAF is distributed by the National Optical Astronomy Observatory, which is operated by the Association of Universities for Research in Astronomy, Inc., under cooperative agreement with the National Science Foundation

⁴http://physics.nist.gov/PhysRefData/ASD/lines_form.html

⁵Interactive Data Language

for sources with half-subtype classifications, we compared to both the lower and higher integer subtype template. Velocity shifts from each band (and multiple templates) were then averaged and the standard deviation used as an estimate of the uncertainty. The latter were typically $\sim 5 \text{ km s}^{-1}$, slightly smaller than our line center uncertainties.

Figure 8 compares our RVs based on this method to literature values. Unlike the line center measurements, we find a marginally significant offset in our measurements of $6.5 \pm 3.7 \text{ km s}^{-1}$ (excluding J0517–3349), with the SDSS measurements being consistently more positive. To assess whether this was a consequence of our smoothing function, we performed the same cross-correlation on unsmoothed data and found a comparable offset. As the SDSS templates are shifted to a zero velocity rest frame in vacuum wavelengths using several of some of the same lines employed in our line centering analysis (K I, Na I and H α), we are unable to identify the origin of this offset.

3.3. Cross-correlation with MagE Radial Velocity Standards

Our third approach was to use the spectra of 40 sources in our sample with independently measured, high-precision RVs as cross-correlation standards. We matched sources to standards that had equivalent spectral types to within ± 1 subtype (excluding the source itself if it was a standard), shifted the standards to zero velocity, and cross-correlated in the five spectral regions listed above. This resulted in up to 50 measurements per source, more for the late-M dwarfs. Following the same rejection and averaging procedures above, our reported values are listed in Table 6. Typical uncertainties are $\sim 1.3 \text{ km s}^{-1}$, with over half of the sources having uncertainties below 1 km s^{-1} ; however, mid-type L dwarfs like J1750–0016 have higher uncertainties due to the fewer RV standards available with equivalent spectral types.

Figure 8 compares these measurements to the literature values, and we find that they are overall consistent, deviating on average by $0.2 \pm 2.7 \text{ km s}^{-1}$ (again excluding J0517–3349). However the χ^2 deviation is somewhat high in this case ($\chi^2 = 123$, $N=55$, $p = 4 \times 10^{-7}$), suggesting that our uncertainties are underestimated. We therefore include a 2 km s^{-1} systematic uncertainty in our reported values, added in quadrature with the standard deviations, which lowers the χ^2 to a value consistent with no deviation ($p = 0.1$). The MagE cross-correlation measurements are also in agreement with the line center measurements (average deviation $-0.8 \pm 3.2 \text{ km s}^{-1}$) but differ from the SDSS measurements ($-6.6 \pm 4.5 \text{ km s}^{-1}$). Given the smaller uncertainties and overall fidelity with prior measurements, we adopt the MagE standard cross correlations with an additional systematic uncertainty as our final RV measurements. The only exception is J1750–0016, whose large uncertainty (14 km s^{-1}) was due to lower S/N data (~ 23 at 7400 \AA) and the availability of only one RV standard; for this source alone we adopt the line center value (Table 6).

3.4. Discrepant Radial Velocities

In addition to J0517–3349, there are three sources whose measured velocities differ by about 3σ or more from previously published values. The L dwarfs J0500+0330 and J0835+0819 have radial velocities from Blake et al. (2010) that are more than 10 km s^{-1} different from our cross-correlation measures, our values being higher and lower, respectively. For these sources, the lack of mid-L dwarf MagE templates, and noise in some spectral regions used for cross-correlation, resulted in only 3-5 cross-correlation measurements. Hence, we conclude that our measurement uncertainties are likely underestimated. For the M8 J2351–2537, our value ($-12 \pm 3 \text{ km s}^{-1}$) deviates by 2.8σ from that of Seifahrt et al. (2010, $-3.0 \pm 1.1 \text{ km s}^{-1}$), but is in agreement with that of Reiners & Basri (2009, $-10 \pm 3 \text{ km s}^{-1}$). Hence, either the Seifahrt measure is in error or this source is binary RV variable. Additional observations are warranted to test the latter hypothesis.

4. Analysis

4.1. UVW Space Motions and Kinematic Populations

We combined our RV measurements with the proper motions and distances listed in Table 1 to compute heliocentric UVW^6 space velocities in the Local Standard of Rest (LSR), following Johnson & Soderblom (1987). We adopted a right-handed coordinate system centered on the Sun, with U toward the Galactic center, V in the direction of Galactic rotation, and W in the direction of the Galactic north pole. Velocities were corrected to the LSR assuming a solar velocity $(U, V, W)_\odot = (11.1, 12.24, 7.25) \text{ km s}^{-1}$ (Schönrich et al. 2010). Uncertainties were propagated through Monte Carlo sampling, assuming normal distributions for all measurement uncertainties. We report the means and standard deviations of these calculations in Table 7.

Figure 10 displays the UVW velocities for our M and L dwarfs and compares them to the 2σ velocity spheroids of the Galactic thin disk, thick disk and halo populations as tabulated in Bensby et al. (2003). Most of our sources cluster around $(U, V, W) = (0, 0, 0)$, with broader dispersions in U and V as compared to W . There is also an asymmetric offset in V which correlates with total LSR velocity; this is attributable to asymmetric drift (Strömgren 1924). There is a noticeable trend between U and V among the L dwarfs in our sample, with $U < 0$ sources tending to also have $V < 0$ and vice versa. We measure a correlation coefficient of $r = 0.43 \pm 0.03$; a weaker trend is also seen among the M dwarfs ($r = 0.21 \pm 0.03$). These trends are discussed in detail below.

We find that the majority of our sources, as expected, fall within the thin disk spheroid, consistent with ages $\lesssim 5$ Gyr. However, several sources fall well outside of this volume. To assess kinematic population membership, we used the method of Bensby et al. (2003) to calculate relative probabilities, $P(\text{TD})/P(\text{D})$ of membership between the thick (TD) and thin (D) disks.

⁶For clarity, all UVW velocities reported in this study are reported in the LSR.

Memberships were assigned as thin disk ($P(\text{TD})/P(\text{D}) < 0.1$), thick disk ($P(\text{TD})/P(\text{D}) > 10$) or intermediate thin/thick disk ($0.1 < P(\text{TD})/P(\text{D}) < 10$). The relative probabilities and population assignments are listed in Table 7. Only one source, J0707–4900, falls fully into the thick disk category, while eleven others are intermediate sources, evenly split between late-M and L dwarfs. We also calculated relative probabilities for halo to thick disk membership, but none exceeded 0.002.

4.2. Velocity Dispersions and Kinematic Ages

As discussed in Section 1, the total velocity dispersion of a stellar population,

$$\sigma_v^2 \equiv \sigma_U^2 + \sigma_V^2 + \sigma_W^2 \quad (3)$$

increases over time as dynamical scattering perturbs Galactic orbits. This produces a correlation between group dispersion and average age. For our analysis, we considered two empirical laws for velocity diffusion. The first is the time-dependent decaying relation of Wielen (1977):

$$\tilde{\sigma}_v(\tau)^3 = \tilde{\sigma}_{v,0}^3 + 1.5\gamma_{v,p}T_\gamma \left(e^{\tau/T_\gamma} - 1 \right), \quad (4)$$

where $\tilde{\sigma}_{v,0} = 10 \text{ km s}^{-1}$, $\gamma_{v,p} = 1.1 \times 10^4 (\text{km s}^{-1})^3 \text{ Gyr}^{-1}$, $T_\gamma = 5 \text{ Gyr}$, $\tilde{\sigma}_v$ is the $|W|$ -weighted total velocity dispersion⁷ measured in km s^{-1} , and τ is the statistical age measured in Gyr. The second is a power-law relation,

$$\sigma_v(\tau) = v_{10} \left(\frac{\tau + \tau_1}{10 \text{ Gyr} + \tau_1} \right)^\beta \quad (5)$$

(cf. Binney & Tremaine 2008), where σ_v is the unweighted total velocity dispersion, and we used all six best-fit parameter sets in Aumer & Binney (2009, Table 2): $55.179 \leq v_{10} \leq 57.975 \text{ km s}^{-1}$, $0.148 \leq \tau_1 \leq 0.261 \text{ Gyr}$ and $0.349 \leq \beta \leq 0.385$.

Table 8 lists the mean velocities, unweighted and weighted dispersions, and corresponding diffusion ages for various subsets of our sample. Uncertainties for all values were propagated forward through Monte Carlo sampling, assuming Gaussian errors for our UVW measurements. For both the full sample (85 sources) and 20 pc sample (70 sources), we find nearly identical results, with unweighted total velocity dispersions around 44 km s^{-1} and equivalent ages of $4.8 \pm 0.2 \text{ Gyr}$ and $5.2 \pm 0.2 \text{ Gyr}$, respectively, based on the Aumer & Binney (2009) relation (the Wielen 1977 relation gives similar ages). The derived ages are in good agreement with the radioisotopic age of the Sun, and are generally consistent with mean age estimates for M and L dwarfs from prior studies (e.g., Reid et al. 2002b; Reiners & Basri 2009; Seifahrt et al. 2010; Blake et al. 2010).

⁷Wielen (1977) defines the $|W|$ -weighted velocity dispersion as having components $\tilde{\sigma}_x^2 = \alpha_x \sum_i |W_i|(X_i - \bar{X})^2 / \sum_i |W_i|$ and $\alpha_x = \{1, 1, 0.5\}$ for $x = \{U, V, W\}$. As noted in Reiners & Basri (2009) and Seifahrt et al. (2010), the weighted dispersion is required to make proper use of the Wielen relations.

4.2.1. Spectral Class Variations

Separating the sample into late-M dwarfs (57 sources) and L dwarfs (28 sources), we find the former to be 1.0–2.5 Gyr younger, depending on the relation used. This result is robust even if the 11 low surface gravity sources, which may be members of YMGs, are rejected (see Section 6): the corresponding ages are 5.0 ± 0.2 Gyr for late-M dwarfs versus 7.1 ± 0.4 Gyr for L dwarfs based on the Aumer & Binney relation. These age differences are statistically significant, and similar to results by Seifahrt et al. (2010) and Blake et al. (2010) who found their L dwarf samples to be kinematically more dispersed than the late-M dwarf samples of Reid et al. (2002b) and Reiners & Basri (2009). Our identical conclusion with a uniformly-analyzed sample confirms this unexpected trend, which we analyze in detail in Section 5.

We note that the ages inferred between the Wielen (1977) and Aumer & Binney (2009) relations are discrepant by $2\text{--}3\sigma$ for these two subsamples; the relations produce more significantly discrepant ages for the unusually blue and inactive L dwarf samples described below. For most subsamples, $\tilde{\sigma} \gtrsim \sigma$, as the inclusion of $|W|$ -weighting tends to increase the inferred dispersion for that component. However, for the L dwarfs, $\tilde{\sigma}_V < \sigma_V$, driving down the total dispersion and hence Wielen ages. Wielen (1977) included $|W|$ -weighting to account for an observed correlation between V^2 and $|W|$; i.e., the correlation between Galactic orbital eccentricity and inclination. For our M and L dwarfs, we find correlation coefficients $r = 0.40 \pm 0.04$ and 0.01 ± 0.07 between these parameters; i.e., there is no correlation for the L dwarfs, which leads to a biased age assessment using the $|W|$ -weighting. For this reason, where the inferred ages between the Wielen (1977) and Aumer & Binney (2009) relations diverge, we favor the latter.

4.2.2. Color Deviants

Late M and L dwarfs are known to exhibit broad variations in near-infrared color within a given subtype, variously attributed to surface gravity, metallicity and cloud effects (e.g., Geballe et al. 2002; Knapp et al. 2004; Burgasser et al. 2008; Kirkpatrick et al. 2008;Looper et al. 2008). As noted in Section 1, analysis of the velocity dispersions of color outliers have led to conflicting conclusions as to the relative ages of unusually red and blue M and L dwarfs (Faherty et al. 2009; Schmidt et al. 2010; Kirkpatrick et al. 2010).

We defined color deviants in our sample as having $J - K_s$ colors more than 0.15 mag redder or bluer than the median color for their optical spectral type, as delineated in the SDSS samples of Schmidt et al. (2010) and West et al. (2011). The threshold color offset was chosen because it is comparable to the scatter in median color versus spectral type in these studies, is at least three times the color uncertainties of the vast majority of our sample ($\sigma_{J-K_s} = 0.03\text{--}0.04$ mag), and provides a small but statistically robust sample of outliers (i.e., 10–15% of the sample). As $J - K_s$ colors generally become more dispersed toward later spectral types (e.g., Kirkpatrick et al. 2008), a constant threshold value may probe more “extreme” M dwarfs as compared to L dwarfs;

however, as shown below, our L dwarf color outliers appear to be more kinematically distinct. Due to the systematic differences in the colors of our sources compared to the Schmidt et al. (2010) and West et al. (2011) trends (Figure 2), all but one of our unusually red dwarfs (9 sources) are M dwarfs (J0835–0819 is the sole red L dwarf) and all of our unusually blue dwarfs are L dwarfs (11 sources).

For the unusually red dwarfs, we find a kinematic age of 2.0 ± 0.2 Gyr for the Aumer & Binney (2009) dispersion relation, considerably younger than the full sample. Remarkably, only one of these red sources, J2045–6332, exhibits Li I absorption and is identified as a low surface gravity dwarf. The remaining sources may have thicker photospheric condensate clouds and/or comprise a coherent, and possibly metal-rich, stream. The unusually blue L dwarfs, on the other hand, have a large velocity dispersion (61 km s^{-1}) and dispersion age of 12.4 ± 0.9 Gyr (for the Wielen 1977 relation the dispersion age is a more reasonable 7.0 ± 0.2 Gyr). Roughly 45% of these sources are also identified as intermediate thin/thick disk stars. The fact that the kinematically colder red dwarfs are mostly type M and the kinematically warmer blue dwarfs are all of type L provides a possible explanation for the age offsets between these spectral classes. Indeed, when color deviants are excluded, the kinematic ages of the late-M dwarfs (4.0 ± 0.2 Gyr) and L dwarfs (3.4 ± 0.3) conform to expectations from population simulations (see below). Thus, we have evidence that the age discrepancy between late-M and L dwarfs originates as a color discrepancy. Section 5.2 discusses this insight in further detail.

4.2.3. Magnetically Active and Inactive Dwarfs

Nonthermal magnetic emission is a common metric for low-mass stellar ages, as emission declines in strength as stars spin down through wind-driven angular momentum loss (e.g., Wilson 1963; Skumanich 1972; Soderblom et al. 1993; Fleming et al. 1995). This process appears to be less efficient for late-M and L dwarfs based on the longer timescales inferred for magnetic field decay (West et al. 2006; Schmidt et al. 2007; West et al. 2008; Reiners & Basri 2008) and faster rotation rates among older L dwarfs (Mohanty & Basri 2003; Reiners & Basri 2006, 2010). There has also been evidence of a reversal in the standard age-activity relation in the L dwarf regime, with only the older and more massive stellar L dwarfs having sufficient field energy to drive nonthermal emission (Gizis et al. 2000; Reiners & Christensen 2010; Burgasser et al. 2011).

As discussed in Section 2.4, while the majority of our sample exhibits H α emission, the L dwarfs are roughly evenly split between active and inactive sources. Comparing these subsets, we find that active L dwarfs have a significantly smaller overall dispersion ($45.9 \pm 1.1 \text{ km s}^{-1}$) than the non-active L dwarfs ($51.5 \pm 0.7 \text{ km s}^{-1}$) and a correspondingly younger dispersion age (5.6 ± 0.4 Gyr versus 7.8 ± 0.5 Gyr for the Aumer & Binney relation). This would appear to confirm an underlying age-activity relation that is similar to earlier-type stars; i.e., older L dwarfs are less active.

4.2.4. Li-bearing and Low Surface Gravity Brown Dwarfs

The nine late M and L dwarfs exhibiting Li I absorption exhibit the smallest velocity dispersions in our sample, with $\sigma_v = 10.4 \pm 0.5$ km s $^{-1}$. Both age dispersion relations are undefined for this value, yielding effective upper limits of order 100 Myr. This is qualitatively in line with evolutionary model predictions from Baraffe et al. (2003), as a Li-bearing M7.5 (versus L1.5) dwarf with an estimated⁸ $T_{eff} \approx 2600$ K (versus 2050 K) and mass below $0.06 M_\odot$ should have an age of no more than 120 Myr (versus 570 Myr). Several of these sources show low surface gravity features in their optical spectra (Section 2.5) and are kinematic members of nearby young moving groups with ages of 10–100 Myr (Section 5). Hence, the velocity dispersions are consistent with overall spectral properties. Similarly, the total velocity dispersion for the 11 low surface gravity sources is 11.9 ± 0.6 km s $^{-1}$, again implying ages $\lesssim 100$ Myr.

4.3. Velocity Probability Distributions

The ages estimated in the previous section are contingent on the velocity distributions being Gaussian. However, both visual examination of the UVW plots in Figure 10 and discrepancies between the age-dispersion relations used argue that non-Gaussian effects are likely present (see also Binney et al. 2014). We therefore constructed probability (“probit”) plots for our various subsamples for each of the U , V and W coordinates, following procedures described in previous studies (Lutz & Upgren 1980; Reid et al. 2002a; Bochanski et al. 2007a; Reiners & Basri 2009). Probit plots are a rank order mapping of velocity to Gaussian probability, generating a straight line for a single Gaussian distribution with a slope equal to the standard deviation. Deviations from Gaussian emerge as variations in the slope.

Figure 11–13 displays UVW probit plots for our 20 pc, late-M dwarf and L dwarf subsamples. It is clear that only the U distributions for the 20 pc and late-M dwarf samples are single Gaussian distributions; both V and W distributions show significant slope variations beyond $\pm 1\sigma$, with those in W being more pronounced. Following Bochanski et al. (2007a), we performed a piece-wise fit to these trends, over “core” ($|\sigma| \leq 1$) and “wing” components ($|\sigma| > 1$), sampling the data uncertainties through Monte Carlo analysis. Table 8 lists the resulting UVW and total velocity dispersions (unweighted) and corresponding ages based on the Aumer & Binney (2009) relation. In general, core components have dispersions and ages just below those of the full sample analysis above, while the wing components have greater dispersions and older kinematic ages. The V probit plots exhibit extended tails to negative velocities and curvature at positive velocities, which again can be attributed to asymmetric drift.

Focusing on the M and L dwarf subsamples, we find clear differences in the velocity distri-

⁸ Based on the T_{eff} /spectral type relation of Stephens et al. (2009).

butions for all three components, most notably in U . Here, the L dwarfs exhibit both a nonzero mean velocity ($\langle U \rangle = 14.7 \pm 0.5 \text{ km s}^{-1}$) and a pronounced asymmetry about this mean. The offset indicates a net flow of L dwarfs toward the Galactic center, and persists even when color deviants are excluded ($\langle U \rangle = 10.1 \pm 0.8 \text{ km s}^{-1}$). The slope change in the probit plot across the mean is not seen in any of the other velocity components or subsamples. This pattern is remarkable and, along with the correlation between U and V and lack of correlation between V^2 and $|W|$, suggests that the kinematics of L dwarfs in our sample are distinct, either intrinsically or though sample bias. We focus on this problem in Section 5.

4.4. Galactic Orbits

As a final examination of the statistical properties of our sample, we used the UVW velocities and Galactocentric coordinates to compute Galactic orbits in a static, axisymmetric potential. We followed the same strategy as described in Bochanski et al. (2011), converting heliocentric velocities to cylindrical velocities (V_R , V_ϕ , V_Z) in the Galactic frame of rest, assuming an LSR azimuthal motion of 240 km s^{-1} (Reid et al. 2014; Antoja et al. 2015). We computed Galactic spatial coordinates for our sources relative to an assumed solar position of $(X, Y, Z)_\odot = (-8.43, 0, 0.027) \text{ kpc}$ (Chen et al. 2001; Reid et al. 2014), with XYZ defined in the same manner as UVW . For the Galactic potential, we adopted static, axisymmetric oblate Plummer’s sphere models for the Galactic halo, bulge and disk, using the forms described in Kuzmin (1956) and Miyamoto & Nagai (1975), with parameters from Dauphole & Colin (1995). A fourth-order Runge-Kutta integrator was used to calculate the orbit over a period of $\pm 250 \text{ Myr}$ about the current epoch in 10 kyr steps, and both energy and the Z -component of angular momentum were conserved to better than one part in 10^{-3} . To sample measurement uncertainties, we computed 100 orbits for each source, varying the initial distances and velocities in a Monte Carlo fashion assuming normal distributions scaled to the uncertainties listed in Tables 1 and 7.

Figure 14 displays the distributions of inferred orbital elements for our sample: minimum and maximum Galactic radius, maximum absolute vertical displacement, eccentricity ($e \equiv [R_{max} - R_{min}]/[R_{max} + R_{min}]$), and maximum inclination ($\tan i \equiv Z/\sqrt{X^2 + Y^2}$). As expected for a sample dominated by the thin disk population, the majority of our sources exhibit circular ($e \lesssim 0.15$) and planar orbits ($i \lesssim 2^\circ$), although the core of the eccentricity distribution extends to 0.2. Figure 15 shows the orbits of the two sources with the largest values of $P(\text{TD})/P(\text{D})$, the M8.5 J0707–4900 and the L1 J0921–2104. Both have fairly eccentric orbits ($e = 0.4$) which carry them to perigals just outside the spherical bulge ($R \approx 4 \text{ kpc}$; Binney & Tremaine 2008), suggesting that they may be scattered bulge stars. In contrast, several sources currently near perigal reach Galactic radii of over 14 kpc (e.g., the D/TD dwarfs J1539–0520 and J2331–2749). Our local VLM dwarf population therefore samples a significant region of the Galaxy, a point returned to in Section 5. Note that all of the orbits are prograde, consistent with formation in the disk (e.g., Carollo et al. 2008).

Given the distinct velocity distributions of the M and L dwarfs in our sample, we examined

whether their Galactic orbits differed as well. Figure 16 compares the distributions of minimum and maximum Galactic radii for these two subsamples. The L dwarfs have a broader distribution of Galactic radii, with a notable skew to higher maximum radii. Median values for R_{max} for M and L dwarfs are 9.5 kpc and 10.3 kpc, respectively; while median eccentricities are 0.11 and 0.16. In contrast, the median values of $|Z_{max}|$ and orbital inclination are the same for both groups. It appears that the L dwarfs in our sample are distributed more broadly in Galactocentric radius than the late-M dwarfs, which is directly attributable to their unusual U velocity distribution.

5. Discussion: Why are Local L Dwarfs Blue and Dispersed?

The confirmation that nearby L dwarfs appear to be, on average, more dispersed and kinematically older than nearby late-M dwarfs, and that this dispersion is driven by a large fraction of unusually blue L dwarfs, suggests that there is something unusual about the local L dwarf population. Most notable is the asymmetric U distribution of this population that remains even when color outliers are rejected, and indicates the existence of a net radial flow of L dwarfs that is not matched by the late-M dwarfs. Asymmetries in the radial motions of local stars have been observed, and are generally attributed to resonances with Galactic structures; e.g., the Galactic bar and/or spiral arm patterns (Dehnen & Binney 1998; Dehnen 2000; Sellwood & Binney 2002; De Simone et al. 2004; Quillen & Minchev 2005; Famaey et al. 2007; Minchev & Famaey 2010; Quillen et al. 2011). Recent large-scale RV surveys, most notably the RAdial Velocity Experiment (RAVE; Steinmetz et al. 2006; Siebert et al. 2011; Williams et al. 2013; Binney et al. 2014; Sharma et al. 2014) have measured statistically significant RV gradients of order $3\text{--}10 \text{ km s}^{-1} \text{ kpc}^{-1}$ directed toward the Galactic center. Antoja et al. (2015) also find that thin disk stars in the RAVE survey ($[\text{M}/\text{H}] \geq -0.1$, $|Z| < 0.5 \text{ kpc}$) exhibit a correlation between radial and azimuthal motions, with trailing sources ($V_\phi < 0$) streaming outward ($V_r < 0$) and leading sources ($V_\phi > 0$) streaming inward ($V_r > 0$). They attribute this correlation to the local Outer Lindblad Resonance with the Galactic bar, which also builds the Hercules stream (Kalnajs 1991; Dehnen 2000; Antoja et al. 2014). We see precisely this same trend among the L dwarfs in their U and V velocities (Figure 10), but curiously not among the late-M dwarfs.

Given prior evidence of radial motion gradients among local stars, we hypothesize that the variance between the late-M and L dwarfs in our sample arises from two possible sources: (1) an inherent asymmetry in the ages and velocity distribution of local L dwarfs made manifest by brown dwarf thermal evolution; and (2) a bias among the L dwarfs in our sample or in the local 20 pc population. We consider each of these hypotheses in turn.

5.1. Is There an Inherent Asymmetry in L Dwarf Ages and Kinematics?

The lowest-order inherent asymmetry in the distribution of stars in the Galactic disk is the radial density distribution, which increases toward the Galactic center. To test whether this spatial asymmetry, coupled with brown dwarf evolution, could drive an asymmetry in the radial motions of L dwarfs, we performed a Monte Carlo population simulation combining brown dwarf evolution, age-dependent velocity dispersions, radial mixing through Galactic orbital motion, and selection biases inherent to a local sample.

A population of stars and brown dwarfs was generated as described in Burgasser (2004, 2007), assuming an initial mass function

$$\frac{dN}{dM} \propto M^{-\alpha} \quad (6)$$

and age distribution (star formation rate)

$$\frac{dN}{d\tau} \propto e^{\beta(\tau-T_0)}. \quad (7)$$

Here, M is mass, constrained to $0.01 M_{\odot} \leq M \leq 0.20 M_{\odot}$; τ is age, constrained to $0.2 \text{ Gyr} \leq \tau \leq 8 \text{ Gyr}$; N is the number density of stars in a given volume; $\alpha = \{-0.5, 0.0, 0.5, 1.0\}$ is the mass function power-law index; $\beta = \{-0.5, 0.0, 0.5, 1.0\}$ is the star formation rate power-law index; and $T_0 = 8 \text{ Gyr}$ was adopted as the oldest age of stars in the Solar Neighborhood (Haywood et al. 2013). Note that $\alpha > 0$ yields a population dominated by lower-mass objects ($\alpha \approx 0.5$ in nearby clusters; see Bastian et al. 2010 and references therein), while $\beta > 0$ yields a population dominated by older objects ($\beta = 0$ is a common assumption for Galactic population simulations, $\beta = 1$ is consistent with the integrated star formation rate history of field galaxies; see Madau et al. 1998; Aumer & Binney 2009). Drawing 10^5 values of M and τ from these distributions, we inferred the present-day effective temperatures of each source using the evolutionary models of Burrows et al. (2001), and converted these to spectral types using the empirical relation of Stephens et al. (2009). We limited our analysis to those sources with spectral types between M7 and L5, which represents 6-17% of the original simulation sample depending on α and β . We did not consider the role of multiplicity.

Asymmetry in the Galactic stellar distribution and radial mixing were implemented by assigning initial Galactic radii in the range 5.5–11.5 kpc, drawing from a radial exponential distribution

$$\frac{dN}{dR} \propto e^{(R_{\odot}-R)/L} \quad (8)$$

where R is the radial coordinate, $R_{\odot} = 8.43 \text{ kpc}$ is the solar Galactic radius (Reid et al. 2014), and $L = 2.1 \text{ kpc}$ is the radial scaleheight (Jurić et al. 2008). We then assigned UVW velocities in the LSR based on normal distributions centered on zero and with standard deviations determined from the assigned age and the Aumer & Binney (2009) age-dispersion relations above. We also included an asymmetric drift term

$$V_a = \frac{\sigma_R^2}{74 \text{ km/s}} = 23.7 \left(\frac{\tau}{10 \text{ Gyr}} \right)^{0.614} \text{ km/s} \quad (9)$$

based on Aumer & Binney (2009). The assigned velocities and initial Galactic coordinates (assuming $Y = Z = 0$) were used as initial conditions to compute orbits over 500 Myr in steps of 1 Myr in an axisymmetric potential as described in Section 4.4. From these orbit calculations we identified all timesteps among all sources for which $|R - R_\odot| \leq 50$ pc and $|Z| \leq 50$ pc. These 7,000–30,000 orbital snapshots (the number depending on simulation parameters) comprised our “local” sample, and included multiple instances of sources which repeatedly fell within the Galactic Solar torus.

Figure 17 summarizes the results of our baseline simulation with $\alpha = 0.5$ and $\beta = 0.0$, comparing distributions between the initial simulation sample to the dynamically-evolved and locally-selected sample. Independent of selection mechanism, these calculations affirm prior results that the L dwarf population should be on average 0.2–0.4 Gyr younger than the late-M dwarf population due to the loss (through thermal evolution) of old brown dwarfs. This confirms the results for our “normal” color populations, but not the full sample of late-M and L dwarfs. Dynamical evolution and local selection results in a uniformly younger “observed” population, with both late-M and L dwarfs being 0.3–0.6 Gyr younger than the initial simulation sample. This offset stems from preferential selection of young objects originating near R_\odot , while most of the older objects scatter outward and are not fully replaced by older objects scattered into R_\odot . We note that the mean ages of locally-selected late-M and L dwarfs in this baseline simulation are somewhat younger than the ages inferred from our velocity analysis; indeed, a value of β between 0.0 and 0.5 appears to be more consistent with the data, suggesting a decline in the VLM star/brown dwarf formation rate over the age of the Galaxy. Nevertheless, we see no evidence of a distinct, highly-dispersed population of L dwarfs for any of the simulation parameters examined.

To produce a sample in which L dwarfs are on average older than late-M dwarfs, we explored cases where the star formation history differed between stars and brown dwarfs. A divergent formation history could arise from mass-dependence in the Galactic birth rate. Figure 18 shows the results for a simulation assuming $\beta = 0.5$ for brown dwarfs ($M < 0.07 M_\odot$) and $\beta = 0.0$ for stars ($M > 0.07 M_\odot$); we also considered the opposite β assignments. The simulation with older brown dwarfs does indeed produce a more dispersed and kinematically older population of L dwarfs by 0.4–0.7 Gyr, although the mean dispersion ages are again younger for both M and L dwarfs than those observed in our full sample.

One possible resolution to the divergent results between simulated and observed kinematic dispersion ages is error in the evolutionary models used to predict the timescales for brown dwarf cooling in our simulations. If the cooling rates are slower than these models predict, we would expect VLM sources to remain L dwarfs for longer periods of time, bringing the simulations into agreement with our observations. Indeed, recent observations of L-type binaries with orbital mass measurements have shown that these sources are 60–100% more luminous than models predict (Dupuy et al. 2009a; Konopacky et al. 2010; Dupuy et al. 2014), so this is a valid concern for our simulations.

The simulations generated two clear asymmetries in the spatial and velocity properties of late-

M and L dwarfs. First, the majority of locally-selected dwarfs in all of the simulations originate (or are at least initially placed) within the Solar radius, with an average offset of ~ 1 kpc. This largely reflects the assumed exponential decline in stellar density with Galactic radius. Second, the azimuthal velocity distributions are skewed to negative velocities, reflecting both the initial radial distribution of stars (which lose azimuthal speed as they climb out of the Galactic potential) and our input azimuthal drift term. However, there are no significant differences between the late-M and L dwarfs for these two parameters, nor for radial and vertical velocity distributions, which are symmetric about and centered on zero. This is true even for separate values of β between stars and brown dwarfs. It appears that we cannot reproduce Galactic radial velocity asymmetries with an axisymmetric potential, as individual stars passing through the local volume have nearly the same probability of moving radially inward as outward on this scale.

Hence, while an older population of L dwarfs can be produced with an assumption of different star formation rates between stars and brown dwarfs, or may be reproduced if there are errors in the evolutionary models; an inherent asymmetry in the U velocity distribution of L dwarfs appears to require perturbations from a non-axisymmetric source; i.e., the Galactic bar and spiral structure. Analysis of these hypotheses are left to more detailed simulations in a future publication, although it is important to assert that any radial mixing induced by Galactic structure must influence M and L dwarfs differently to match our results and those of Seifahrt et al. (2010) and Blake et al. (2010).

5.2. Is There Sample or Cosmic Bias in the Local L Dwarf Population?

A more mundane explanation for our results is that the sample considered here is kinematically biased in its construction. The sample was drawn primarily from all-sky imaging and proper motion surveys, which continue to be incomplete in the Solar Neighborhood (e.g., Luhman 2013; Scholz 2014; Pérez Garrido et al. 2014). Incompleteness is particularly an issue along the Galactic plane due to source crowding. For our sample, we also have a declination limit imposed by the observing site ($\delta < 25^\circ$; Figure 1). To assess whether these “pointing” asymmetries produce velocity trends, Figure 19 displays the distributions of XYZ coordinates for our sample. The M and L dwarfs have similar distributions in X and Y , but in Z the L dwarfs are more centrally concentrated with a slight bias toward positive Z (both subsamples have fewer sources at $Z = 0$ due to Galactic plane exclusion). However, our simulations show no correlation between local Z position and U velocity; simulations by Faure et al. (2014) which include spiral perturbations are similarly symmetric about the Galactic plane. It is therefore unclear what role this difference in vertical spatial distribution would play in producing an asymmetric radial velocity distribution.

Another possible bias is the contribution of YMG members in our sample. At least 8 of the sources investigated here are kinematically associated with YMGs, 7 of which are late-M dwarfs (Section 6). Similarly, 9 of the 11 low surface gravity dwarfs and 8 of the 9 sources exhibiting Li I absorption are late-M dwarfs. There is clearly a “youth bias” between the M and L dwarf

subsamples. However, as noted in Section 4.2.1, while rejecting sources which exhibit low surface gravity features slightly increases the velocity dispersion for the late-M dwarfs and brings their kinematic age closer to (but still less than) the L dwarfs, editing out the low gravity sources does not change the underlying U velocity distributions. Late-M dwarfs remain symmetrically distributed about $U = 0$, and L dwarfs asymmetric and offset. Indeed, removal of the two low gravity L dwarfs in our sample increases the mean velocity offset of the remainder. Hence, contamination by YMGs does not appear to resolve the velocity differences between the M and L dwarfs.

A third possibility is that the local sample itself has an inherent cosmic bias. As described in Section 4.2.2, the unusually blue dwarfs, which are all L dwarfs, are far more dispersed than the unusually red dwarfs, which are predominantly late-M dwarfs. The unusually blue L dwarfs represent 39% of all the L dwarfs in our sample. This suggests a selection effect. However, the identification of color deviants is based on mean near-infrared colors from the optically-selected SDSS surveys, which as discussed in Schmidt et al. (2010) are less color-biased than 2MASS samples and tend to identify bluer sources. It is therefore remarkable that a plurality of the L dwarfs examined here, mostly identified in the 2MASS survey, are bluer still. Evidence that this color skew may actually be a local effect emerges from the fact that 10 of the 11 unusually blue L dwarfs are within 20 pc (the exception is J0923+2340), which is a higher fraction (91%) than the remainder of the L dwarf sample (65%). In other words, the unusually blue L dwarfs are more representative of the local volume than the “normal-color” L dwarfs delineated in Schmidt et al. (2010). It is possible that we are seeing two distinct populations of L dwarfs in the 20 pc volume: a “disk” group whose dispersions conform to simulation expectations, and a “dispersed” group drawn from an older, possibly thick disk VLM population. Given the relatively small number of L dwarfs examined in this study, this speculative hypothesis must be confirmed through a larger study.

6. Candidate Kinematic Members of Nearby Moving Groups and Associations

Several of our sources exhibit Li I absorption and/or spectral features indicative of low surface gravity, and as such are potential members of YMGs. To assess which YMGs these sources are affiliated with, and their probability of affiliation, we used the Bayesian Analysis for Nearby Young AssociatioNs II tool (BANYAN II; Gagné et al. 2014) which uses spatial and velocity coordinates and photometry to assess the probability of membership (P_M) and field contamination (P_C) for individual sources. Our YMG sample included the TW Hydreae Association (TWA; Kastner et al. 1997; de la Reza et al. 1989, Zuckerman & Song 2004; 10 Myr; Weinberger et al. 2013), the β Pictoris Moving Group (β PMG; Zuckerman et al. 2001; 20 – 26 Myr; Mamajek & Bell 2014, Malo et al. 2014, Binks & Jeffries 2014), the Tucana-Horologium Association (THA; Torres et al. 2000, Zuckerman & Webb 2000; 40 Myr; Kraus et al. 2014), the Carina association (CAR; 20 – 40 Myr; Torres et al. 2008), the Columba association (COL; 20 – 40 Myr; Torres et al. 2008), the Argus/IC 2391 association (ARG; 30 – 50 Myr; Torres et al. 2008), and the AB Doradus moving group (ABD; Zuckerman et al. 2004;

110 – 130 Myr ; Luhman et al. 2005, Barenfeld et al. 2013). We adopt the spatial and kinematic models for each of these associations given in Gagné et al. (2014), and include distances in our comparison for those sources with trigonometric parallax measurements.

Table 10 lists the membership and contamination probabilities of sources with membership probabilities $P_M > 10\%$. We also list the spatial (ΔD) and velocity (ΔV) offsets from the respective centers of the best-match association. In the following discussion on individual candidates, we used the effective temperature (T_{eff})/spectral type calibration of Stephens et al. (2009) and the evolutionary models of Baraffe et al. (2003) to estimate physical parameters.

6.1. Previously Known Candidate Members

J0041–5621AB (M6.5 + M9): The combined-light spectrum of this resolved binary displays H α emission, Li I absorption, and weak low surface gravity features. It was previously identified as a possible member of either THA or β PMG by Reiners & Basri (2009) on the basis of its Li I absorption, kinematics and evidence of ongoing accretion. Gagné et al. (2014) favored association with THA based on a BANYAN II analysis of the same data, and our revised analysis supports that conclusion, with a membership probability $P_M > 99.9\%$ and $P_C < 0.1\%$. While this source does not have a trigonometric parallax, the BANYAN II tool predicts a statistical distance of 41^{+2}_{-3} pc if it is a member of THA, placing it 7 pc and 1.4 km s^{-1} away from the center of the spatial and kinematic model. Reiners et al. (2010) resolved the system into a 142.8 ± 0.5 mas binary and estimated component types of M6.5+M9 and masses of $30 M_{Jup}$ and $15 M_{Jup}$ for an age of 10 Myr. Our combined-light spectrum is considerably later than M6.5 (Figure 7), suggesting that the primary may be cooler than inferred in that study. Adopting effective temperatures of 2500 K and 2400 K based on component types of M8+M9, a THA age of 40 Myr, a distance of 41 pc, and the evolutionary models of Baraffe et al. (2003), we predict masses of $40 M_{Jup}$ and $35 M_{Jup}$, a projected separation of 6 AU, and an orbit period of 50 yr. The last value is less than half that estimated by Reiners et al. (2010), and suggests that orbital motion could be detectable over the coming decade.

J0123–6921 (M9) was proposed as a THA member by Gagné et al. (2014), and our reanalysis supports this conclusion ($P_M > 99.9\%$ and $P_C < 0.1\%$). Like J0041–5621AB, this source exhibits Li I absorption, H α emission and weak signatures of low surface gravity. We again infer a significantly later spectral type for this source than the M7.5 reported in Reiners & Basri (2009), and we estimate its mass to be $35 M_{Jup}$.

J0339–3525 (LP 944-20, M9) has been identified by Ribas (2003) as a candidate member of the controversial Castor “association” (CAS; Barrado y Navascués 1998). In contrast, Gagné et al. (2014) identify J0339–3525 was a candidate member of ARG using BANYAN II, but note that its XYZUVW coordinates are much closer to CAS. Our findings show a weak membership probability for ARG ($P_M = 16.7\%$) but low field contamination ($P_C = 0.3\%$), suggesting that it is likely

part of a different association. The spectrum of J0339–3525 shows weak features of low surface gravity, with particularly enhanced VO absorption at 7400 Å and weak and narrow alkali lines, H α emission, and weak Li I absorption (Tinney 1998; Reiners & Basri 2009). All of these observations point to either a very young ($\lesssim 30$ Myr) low-mass brown dwarf or, as argued by Tinney (1998), Ribas (2003) and Pavlenko et al. (2007) an “intermediate”-aged (≈ 300 –600 Myr) brown dwarf with partial Li depletion. It has been recently argued that hypothesized CAS “members”, which have included Fomalhaut ABC (440 ± 40 Myr; Mamajek 2012) and Vega (455–700 Myr; Yoon et al. 2010; Monnier et al. 2012), do not share a common origin or composition, and is likely a dynamical stream (e.g., Mamajek et al. 2013; Mamajek 2012; Monnier et al. 2012; Zuckerman et al. 2013). Indeed, Mamajek et al. (2013) specifically note that J0339–3525’s current proximity to Fomalhaut may be short-lived. J0339–3525 may therefore be a “juvenile” brown dwarf caught up in a Galactic dynamical pattern rather than a member of a bona-fide association.

J1139–3159 (TWA 26, M9 γ) is a previously reported member of TWA (Gizis 2002), and our results are consistent with this assignment ($P_M = 99.6\%$ and $P_C = 0.1\%$). With strong signatures of low surface gravity, Li I absorption and a full complement of H α , H β and H γ emission, this source is an unambiguous young brown dwarf.

J2000–7523 (M9) is a previously reported candidate of β PMG (Gagné et al. 2014) or CAS (Gálvez-Ortiz et al. 2010) with pronounced low surface gravity features. Our BANYAN analysis favors the β PMG assignment ($P_M = 99.0\%$, $P_C = 4.1\%$). Notably, this source does not show Li I absorption, an effect likely related to weak alkali lines in low surface gravity photospheres as posited by Kirkpatrick et al. (2008). That study suggests an age of $\lesssim 30$ Myr for such sources, which is consistent with β PMG membership.

J2045–6332 (M9) was identified in Gálvez-Ortiz et al. (2010, 2014) as a high-probability member of CAS (note discussion above). We confirm the presence of Li I absorption reported in those studies, and also note H α and H β in emission and strong low surface gravity spectral features, implying a young source. Like J2000–7523, we find this source to have a better membership match to β PMG ($P_M = 87\%$, $P_C = 0.2\%$), which is also supported by its strongly suppressed alkali lines, although the peculiar motion is somewhat large (7 km s^{-1}).

6.2. New Candidate Members

J0823–4912AB (L3) is a low-probability candidate member of β PMG based on our analysis ($P_M = 30\%$, $P_C = 0.4\%$). This source exhibits both Li I absorption and spectral features consistent with low/intermediate surface gravity. Its distance and proper motion measurements give it relatively large peculiar motion relative to β PMG (7 km s^{-1}). Sahlmann et al. (2013, 2015) have identified this source as an astrometric binary with a mid-to-late L dwarf companion, and it is possible that the orbital motion of this system is skewing the inferred systemic motion in the radial direction (tangential motion is likely averaged out). Sahlmann et al. (2015) also report Li I in

absorption and the presence of low-surface gravity features in its near-infrared spectrum. However, based on comparison of the system mass function, component classifications and evolutionary models, the Sahlmann et al. (2015) study supports an age in the range 70–470 Myr for J0823–4912AB, considerably older than β PMG. J0823–4912AB may therefore be an interloping member of a older YMG or stream, perhaps CAS.

J1510–2818 (M9) is identified as a modest-probability candidate member of ARG ($P_M = 60\%$ and $P_C = 34\%$). The source exhibits H α emission and strong signatures of low surface gravity in its spectrum, but no Li I. Again, the absence of Li I may be related to weak surface gravity at an age $\lesssim 30$ Myr, which is marginally consistent with the 30–50 Myr age estimate for ARG. A trigonometric distance measurement could confirm or refute ARG membership; BANYAN II predicts a statistical distance of 27_{-3}^{+2} pc for ARG membership, and 35_{-7}^{+11} pc for membership in the field.

6.3. Interlopers

J1456–2809 (LHS 3003, M7) emerged as a candidate member of ABD in our analysis ($P_B = 94.3\%$, $P_C = 4.3\%$). However, this source displays no signs of low surface gravity in either its optical or near-infrared spectra (Bardalez Gagliuffi et al. 2014), and no Li I absorption, implying an age $\gtrsim 500$ Myr. Its H α emission does not provide a good constraint on its age; chromospheric activity lasts up to 8 Gyr in late-M dwarfs (West et al. 2011). With its close proximity to the locus of ABD members (21.2 pc and 2.5 km s^{-1} from the center of our model), J1456–2809 highlights the importance of identifying signs of youth before assigning YMG membership.

6.4. Candidate Young Brown Dwarfs Not Assigned to a Young Moving Group

Three additional sources exhibiting spectral signatures of low surface gravity were not found to be members of the well-characterized young associations listed above. We performed a second-order check of additional systems based exclusively on UVW velocities: the Octans Association (≈ 30 –40 Myr; Murphy & Lawson 2015); the Ursa Major Moving Group (≈ 500 Myr; King et al. 2003); the Hercules-Lyrae Moving Group (≈ 250 Myr; Eisenbeiss et al. 2013); Carina-Near Moving Group (≈ 200 Myr; Zuckerman et al. 2006); and various streams listed in Zuckerman & Song (2004), including CAS.

J0652–2534 (M9) has a spectrum similar to J0339–3525, with somewhat weakened alkali absorption (including narrow K I doublet lines) and enhanced VO absorption at 7900 Å, both suggesting a modestly low surface gravity. In addition, the spectrum exhibits Li I absorption, but no H α emission. Given these features, J0652–2534 is likely a few hundred Myr old. Its closest match in UVW space is Octans, but the source is about 20 km s^{-1} discrepant from that association’s UVW center and is probably too old. This “juvenile” brown dwarf must be a member of an association

or stream not considered here, or may be an unassociated system.

J0909–0658 (L1) exhibits strong signatures of low surface gravity, most notably enhanced VO absorption at 7400 Å and 7900 Å, weak FeH and CrH bands, and somewhat narrower K I lines. This source does not exhibit Li I absorption, and the presence of clear Na I, Rb I and Cs I lines argues against low surface gravity being the reason. Assuming a mass greater than $0.06 M_{\odot}$ and $T_{eff} = 2100$ K, this implies an age of at least 500 Myr. Of all the kinematic groups listed above, ARG has the closest association in UVW space, but J0909–0658 is clearly too old for that group. If this source is a young brown dwarf, it must be a member of an older association or stream or solivagant. Alternately, its unusual metal-oxide and metal-hydride features may reflect non-solar (possibly super-solar) composition. Thorough analysis of this source’s full spectral energy distribution is warranted.

J1411–2119 (M9), like J0339–3525 and J0652–2534, exhibits weak spectral signatures of low surface gravity (weak Na I absorption at 8183/8195 Å) and Li I absorption, as well as pronounced H α and H β emission. Its closest match in UVW space is the ≈ 500 Myr Ursa Majoris Group, but J1411–2119 remains about 13 km s $^{-1}$ apart from the cluster motion center, and it is positioned far from other members of the group (King et al. 2003). Again, this brown dwarf may be part of an as-yet unrecognized moving group or unassociated.

7. Additional Sources of Interest

J0707–4900 (M8.5) is remarkable in its conflicting kinematic, activity and color indicators of age. Originally identified by Ruiz et al. (1991) as a brown dwarf candidate in the Hyades moving group, this source has a large radial velocity (113 ± 2 km s $^{-1}$) and its UVW velocity components identify it as an intermediate thin/thick disk star (see also Dupuy et al. 2009b). It has the most negative V velocity in our sample, and its prograde Galactic orbit is highly eccentric (0.46 ± 0.01) but with a modest inclination ($2^\circ 5 \pm 1^\circ 0$). However, its spectrum exhibits no obvious signatures of metal-deficiency, and its near-infrared color is unusually red for its spectral type. The weak H α emission detected in our spectrum ($\log_{10} L_{H\alpha}/L_{bol} = -5.33 \pm 0.06$) is somewhat lower than prior detections ($\log_{10} L_{H\alpha}/L_{bol} = -4.9$ by Tinney & Reid 1998; $\log_{10} L_{H\alpha}/L_{bol} = -4.4$ by Mohanty & Basri 2003), but consistent with a star whose magnetic dynamo has weakened but persists. Mohanty & Basri (2003) report $v \sin i = 10$ km s $^{-1}$ for this source, making it a relatively rapid rotator with weak magnetic emission. That study attributes the anomalous behavior of J0707–4900 to a low surface gravity associated with low mass and youth. Hence, the kinematics and low level of activity suggest an old age for J0707–4900, while its color and rapid rotation supports a young age. It is possible that the red color of this source indicates the presence of a mid-to-late L dwarf companion as yet unresolved. The stability in its radial and astrometric motion (three measurements by Ianna & Fredrick 1995; Tinney 1996 and Henry et al. 2004) argues against the existence of a $\lesssim 0.3$ AU binary, but this source is clearly anomalous and merits further attention.

J2036+1051 (L3) is one of two unusually active L dwarfs identified in our program. It was first observed by Schmidt et al. (2007) and found to have no H α emission to a limit of EW > -6.3 \AA . In contrast, we measure EW = $-11.5 \pm 3.0\text{ \AA}$ (H β and H γ lines were too weak to be detected). It appears that we caught this rapidly rotating dwarf ($v \sin i = 67.1 \pm 1.5\text{ km s}^{-1}$; Blake et al. 2010) in a flare state. We note that the alkali lines in this source are a little weak compared to other L3 dwarfs in the sample (with the exception of J0823–4912AB), but the kinematics are consistent with an older disk source. The alkali lines may have been filled in by continuum emission from the flare.

J2037–1137 (M8) is the earliest-type source in our sample to exhibit no detectable H α emission, to an EW limit of $>-0.3\text{ \AA}$ and $\log_{10} L_{H\alpha}/L_{bol} < -6.74$. In contrast, prior studies have consistently detected emission in the range $-5.51 \lesssim \log_{10} L_{H\alpha}/L_{bol} \lesssim -4.48$ (Schmidt et al. 2007; Reiners & Basri 2010; Lee et al. 2010). Unlike J2036+1051, this slowly rotating dwarf ($v \sin i \leq 3 \pm 2\text{ km s}^{-1}$; Reiners & Basri 2009) may have been observed during a minimum in its magnetic emission cycle, or in an orientation exhibiting a relatively quiescent surface.

8. Summary

This paper has reported the radial velocities of 85 VLM stars and brown dwarfs of spectral types M6–L6 with MagE with typical precisions of 2–3 km s $^{-1}$. Combining these with previously published proper motions and distances, we computed UVW velocities and examined velocity dispersions as a function of spectral type, color and magnetic activity. We find that unusually blue objects are more dispersed than unusually red objects, in support of color effects being driven by higher surface gravities and/or slightly subsolar metallicities among an older, low-mass stellar population. We also find that magnetically inactive L dwarfs are more dispersed than magnetically active L dwarfs, following the age-activity relations of earlier-type stars. The most interesting finding is the greater dispersions and U velocity offset (net radial flow) of L dwarfs as compared to late-M dwarfs. The greater dispersions of L dwarfs affirms prior results by Seifahrt et al. (2010) and Blake et al. (2010), but we speculate that this may be driven by a large fraction of unusually blue L dwarfs in local 20 pc sample as compared to deeper imaging surveys. Population simulations incorporating brown dwarf evolution, Galactic dynamics in an axisymmetric potential, and local selection still predict that L dwarfs should be younger than late-M dwarfs, although this can be reversed if brown dwarfs have had a different formation history than stars (or alternately, evolve more quickly than evolutionary models predict). However, these simulations cannot reproduce the distinct U velocity distribution of L dwarfs, which is either driven by non-axisymmetric Galactic structure (e.g., bar, spiral arms) or the existence of a distinct, dispersed population of L dwarfs in the Solar Neighborhood. We also identify 8 kinematic members of nearby YMGs, including new candidates J0823–4912AB in the β Pictoris Moving Group (although likely part of an older association/stream) and J1510–2818 in the Argus Association. Three additional sources, J0652–2534, J0909–0658 and J1411–2119 have evidence of low surface gravities but no YMG assignment; these may be members of older moving

groups or streams, or simply solivagant \sim 500 Myr-old brown dwarfs.

The ultimate goal of the Brown Dwarf Kinematics Project is a complete kinematic sampling of the lowest-mass stars and brown dwarfs in the vicinity of the Sun. With 25% of the 20 pc late-M and L dwarf sample studied here, we are likely still missing additional members of nearby YMGs, and we may still be subject to (unknown) selection biases due to incompleteness. Work is underway to complete the RV sampling of the local VLM population. Given preliminary evidence of distinct kinematic populations of L dwarfs in the Solar Neighborhood, examining the kinematics of T dwarfs (all of which are substellar) may provide an important anchor for disentangling the mass function and star formation history of our local mixed stellar/substellar population.

9. Acknowledgements

The authors would like to thank Jorge Araya, Mauricio Martinez, Hernan Nunez, and Geraldo Vallardes for assistance in the observations. We acknowledge useful discussions with John Gizis during the preparation of the manuscript. A.A.W acknowledges funding from NSF grants AST-1109273 and AST-1255568 and support from the Research Corporation for Science Advancement's Cottrell Scholarship; E.E.M acknowledges support from NSF grant AST-1313029. This publication makes use of data products from the Two Micron All Sky Survey, which is a joint project of the University of Massachusetts and the Infrared Processing and Analysis Center/California Institute of Technology, funded by the National Aeronautics and Space Administration and the National Science Foundation. This research has benefitted from the M, L, and T dwarf compendium housed at DwarfArchives.org and maintained by Chris Gelino, Davy Kirkpatrick, and Adam Burgasser. It has also made use of the SIMBAD database and VizieR service, operated at CDS, Strasbourg, France. This article has also made use of data from the Sloan Digital Sky Survey. Funding for the SDSS and SDSS-II has been provided by the Alfred P. Sloan Foundation, the Participating Institutions, the National Science Foundation, the U.S. Department of Energy, the National Aeronautics and Space Administration, the Japanese Monbukagakusho, the Max Planck Society, and the Higher Education Funding Council for England. The SDSS Web Site is <http://www.sdss.org/>. The SDSS is managed by the Astrophysical Research Consortium for the Participating Institutions. The Participating Institutions are the American Museum of Natural History, Astrophysical Institute Potsdam, University of Basel, University of Cambridge, Case Western Reserve University, University of Chicago, Drexel University, Fermilab, the Institute for Advanced Study, the Japan Participation Group, Johns Hopkins University, the Joint Institute for Nuclear Astrophysics, the Kavli Institute for Particle Astrophysics and Cosmology, the Korean Scientist Group, the Chinese Academy of Sciences (LAMOST), Los Alamos National Laboratory, the Max-Planck-Institute for Astronomy (MPIA), the Max-Planck-Institute for Astrophysics (MPA), New Mexico State University, Ohio State University, University of Pittsburgh, University of Portsmouth, Princeton University, the United States Naval Observatory, and the University of Washington.

Facilities: Magellan:Clay

A. Conversion between 2MASS and MKO JHK_s Magnitudes

To compute the bolometric fluxes for our sources, we made use of their 2MASS J -band photometry and MKO J -band bolometric corrections from Liu et al. (2010). This required a small correction between filter magnitude systems due to the highly structured spectra of late M and L dwarfs. Stephens & Leggett (2004) have previously reported corrections for L and T dwarfs as a function of spectral type, but did not include late-M dwarfs in their sample; we therefore computed a new conversion relation spanning types M6 to L7. We selected 533 low-resolution, near-infrared spectra from the SpeX Prism Library (SPL; Burgasser 2014) with reported optical classifications between M6 and L7 and median S/N > 100. We computed spectrophotometric magnitudes in both 2MASS and MKO JHK_s systems following the procedures described in Stephens & Leggett (2004) and Cushing et al. (2005). Figure 20 displays the magnitude differences ($\Delta = \text{MKO}-\text{2MASS}$) in J , H and K_s as a function of spectral type. We fit all three filter differences to second-order polynomials (higher orders did not significantly improve the fits), iteratively rejecting 3σ outliers. The polynomial coefficients and dispersions are listed in Table 11. Both J and H show significant (and opposing) trends, and the polynomial fits produce a residual scatter of 0.005–0.008 mag.

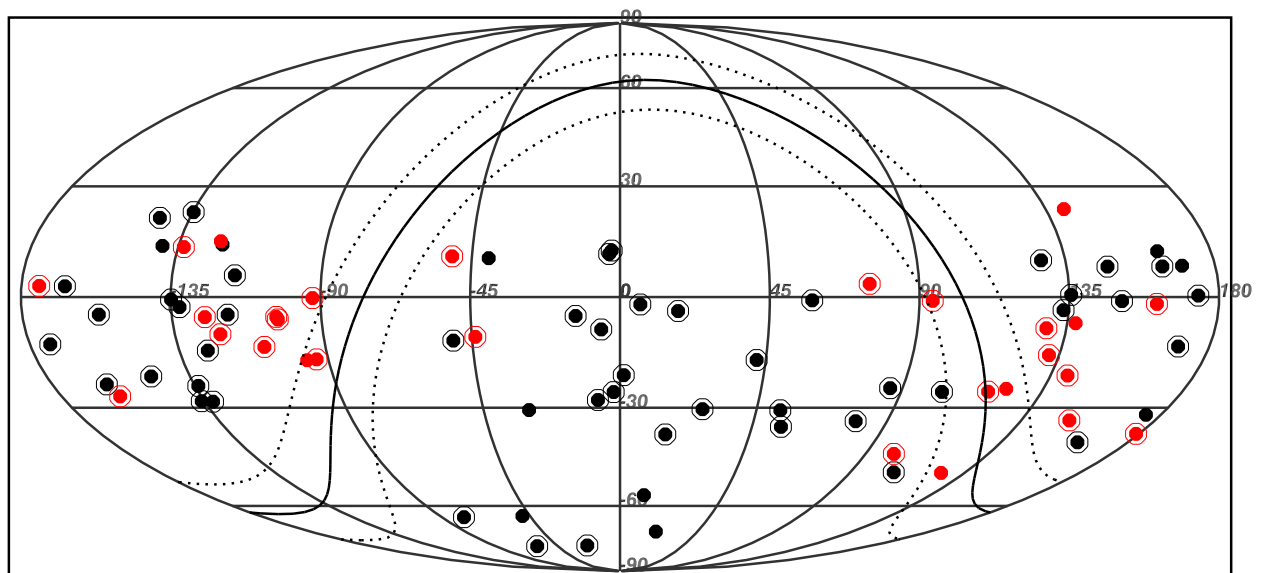


Fig. 1.— Mollweide projection equatorial map of late-M dwarfs (black) and L dwarfs (red) in our sample. Sources within 20 pc are encircled. The Galactic plane and $\pm 10^\circ$ about the plane are indicated by the solid and dotted lines, respectively.

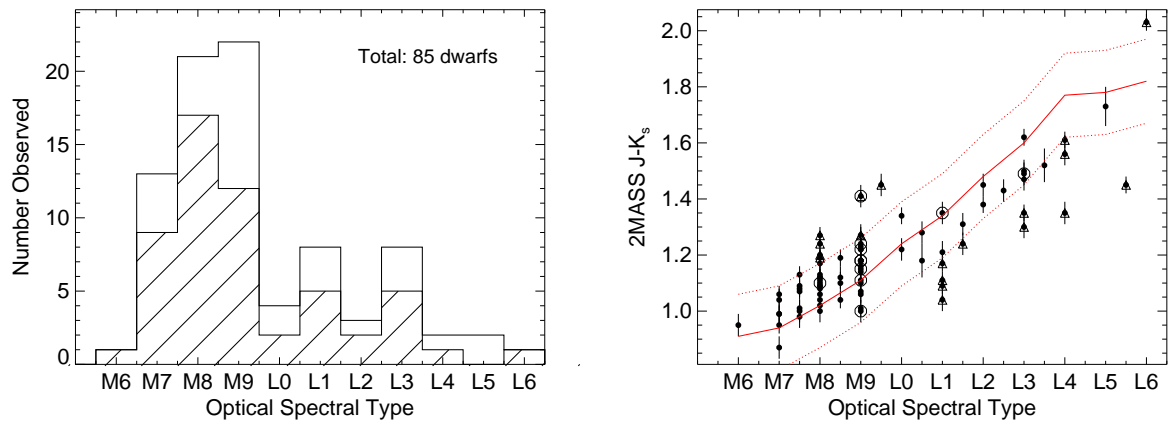


Fig. 2.— (Left): Distribution of optical spectral types for the 85 observed sources, sampled by whole subtype bins. The open histogram refers to all sources observed; the hatched histogram refers to those sources with previously published radial velocities. (Right): 2MASS $J - K_s$ colors of our targets compared to the mean colors of M6–L6 dwarfs (red line) from Schmidt et al. (2010) and West et al. (2011). Our ± 0.15 mag threshold for unusually red and blue dwarfs are indicated by dotted lines, and those sources are highlighted by open triangles. Young sources in our sample are highlighted with open circles.

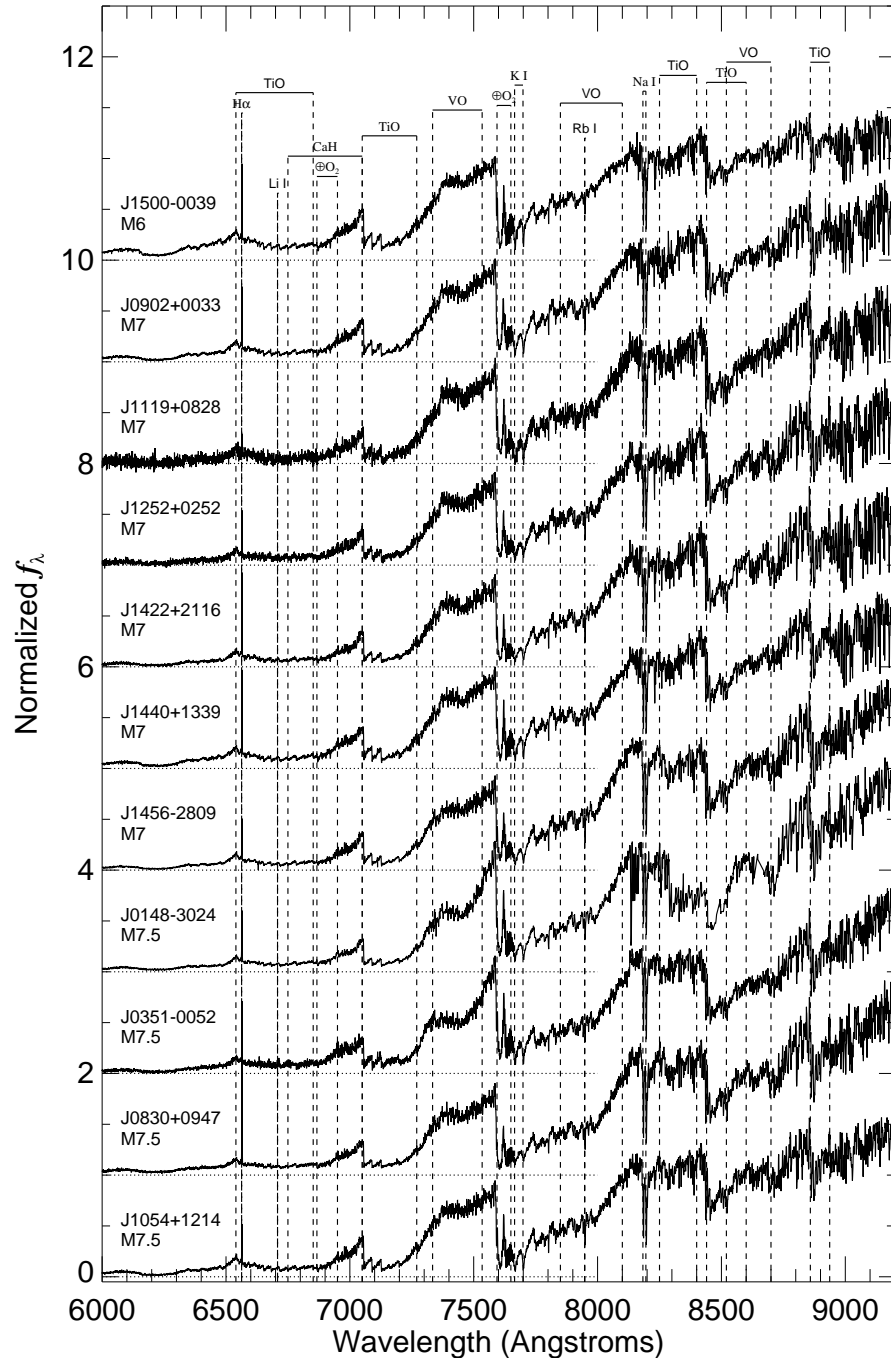


Fig. 3.— Observed MagE spectra of our sample, ordered by spectral type and right ascension. Data are normalized in the 8200–8600 Å range and each spectrum offset by a constant for clarity. Major spectral features from Li I, K I, Na I, Rb I, Cs I, TiO, VO, CrH, FeH, CaH and H I emission are labeled, as is telluric O₂ absorption.

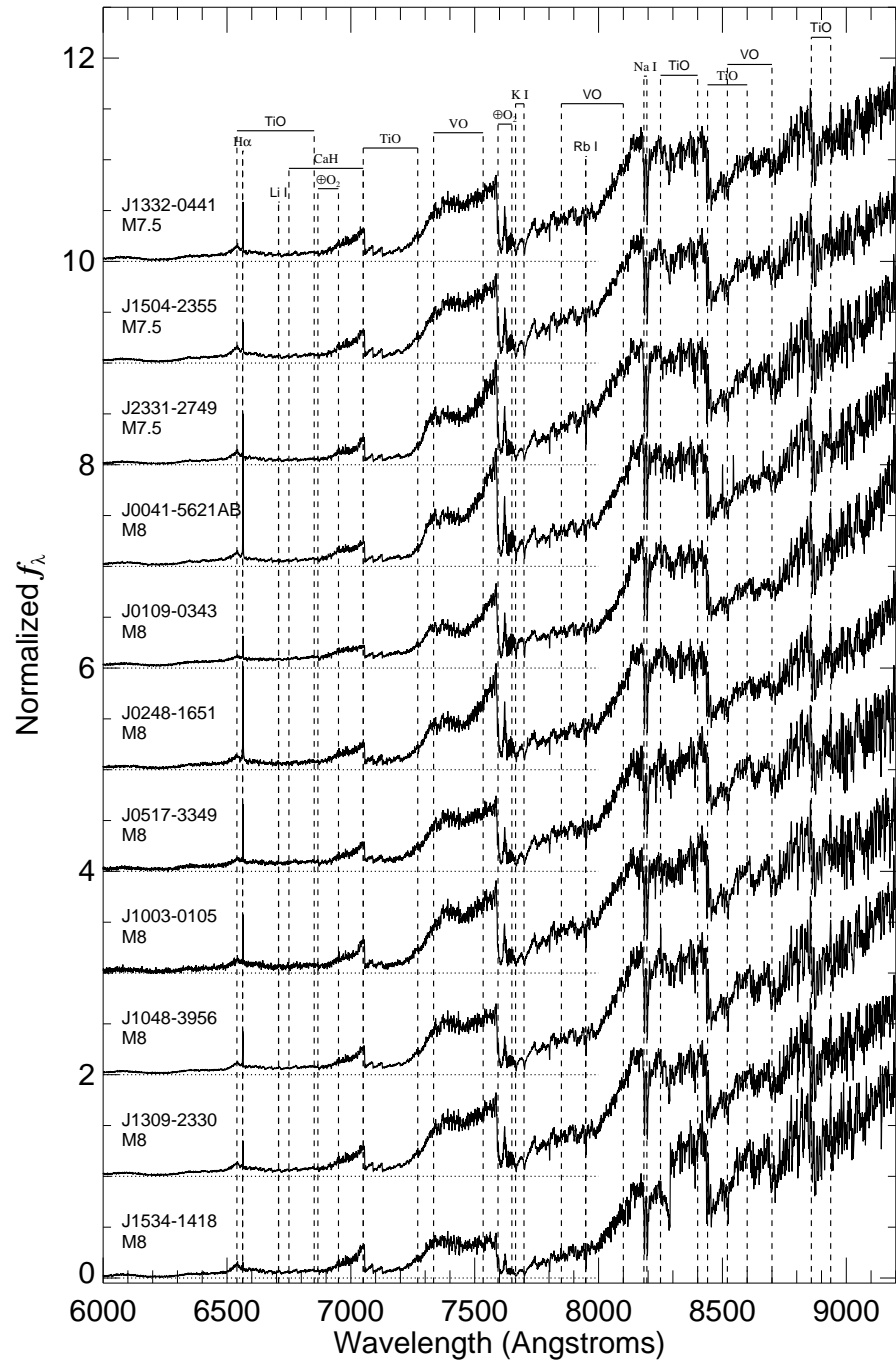


Fig. 3.— Cont.

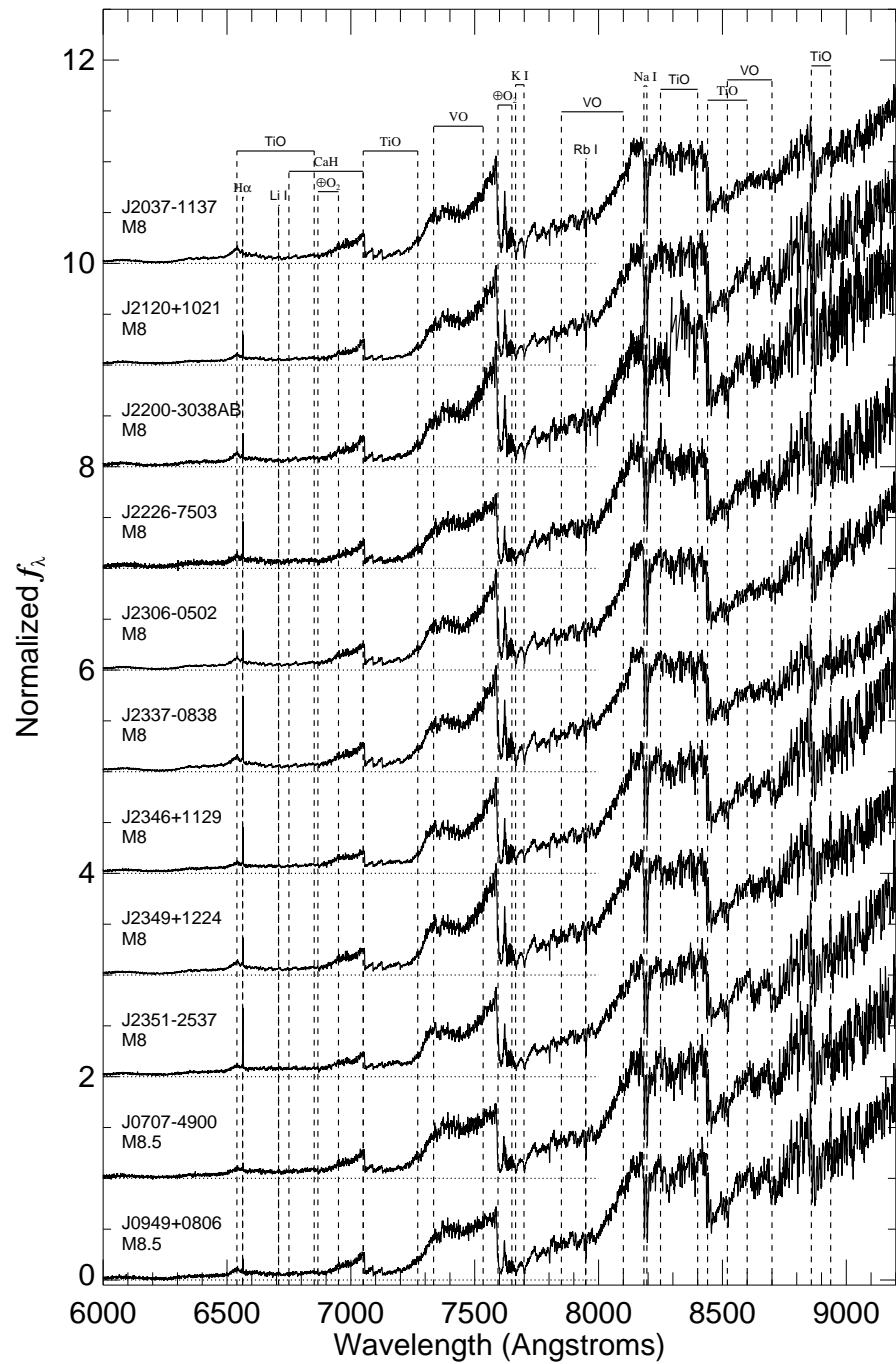


Fig. 3.— Cont.

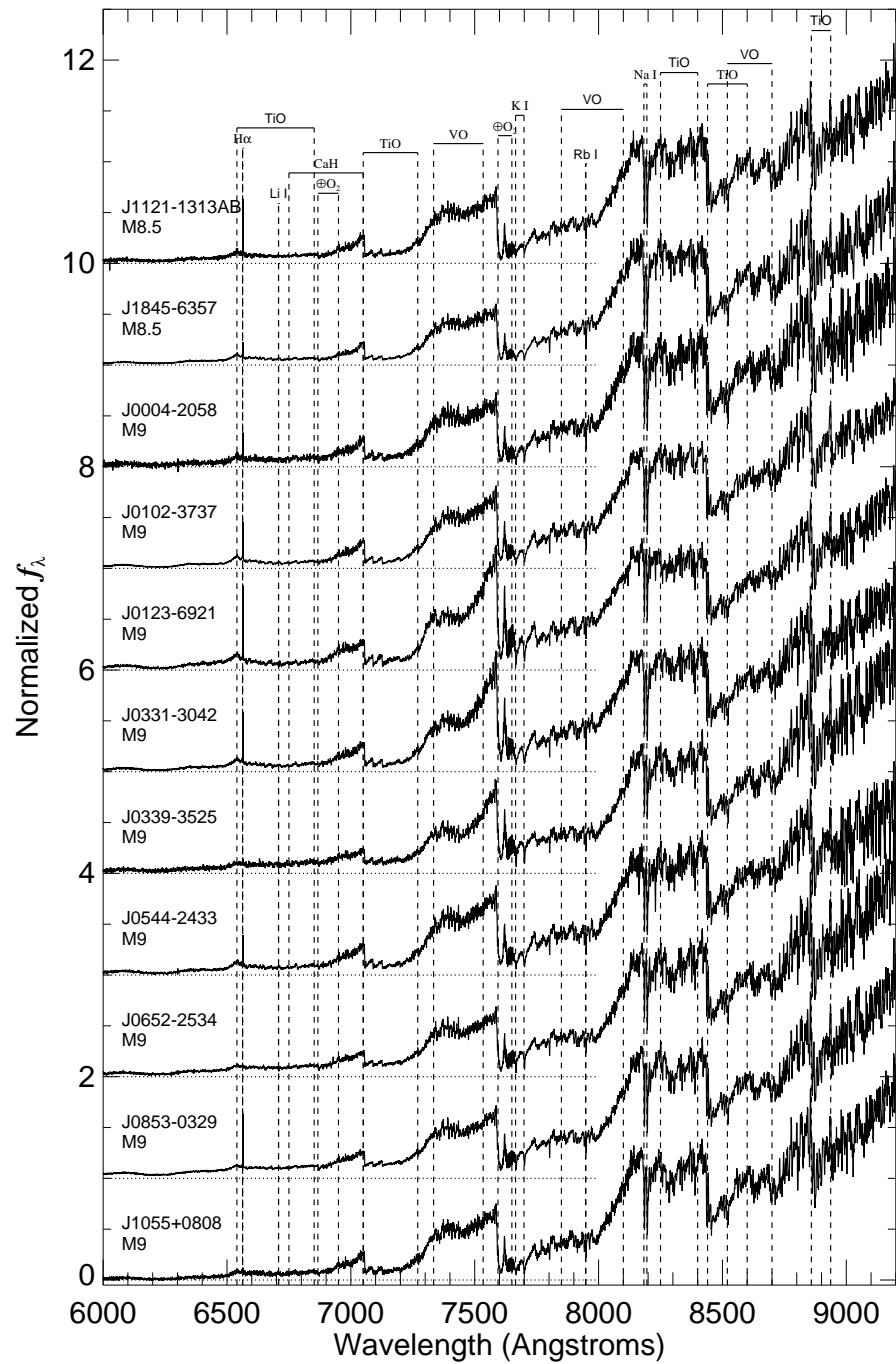


Fig. 3.— Cont.

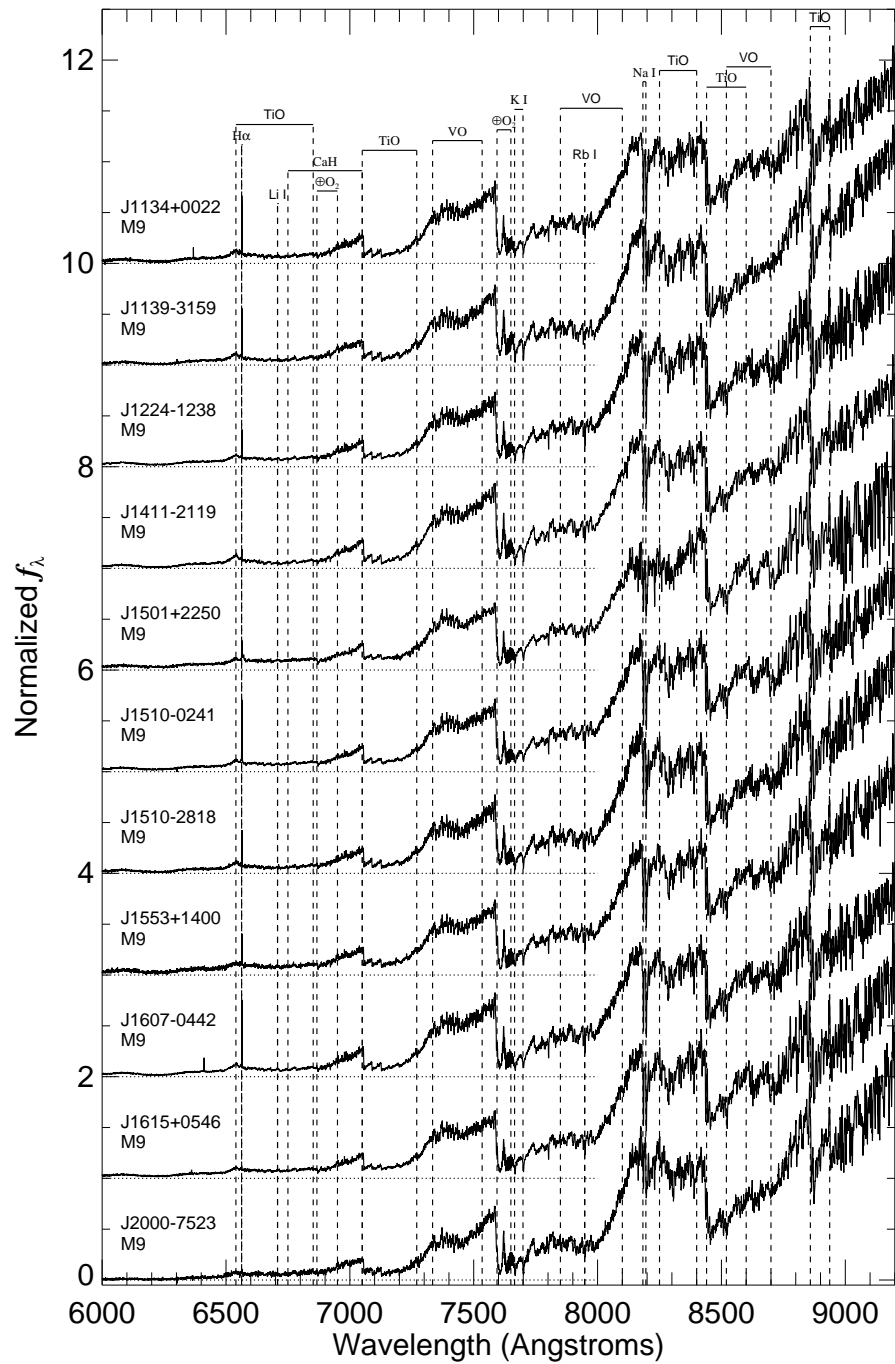


Fig. 3.— Cont.

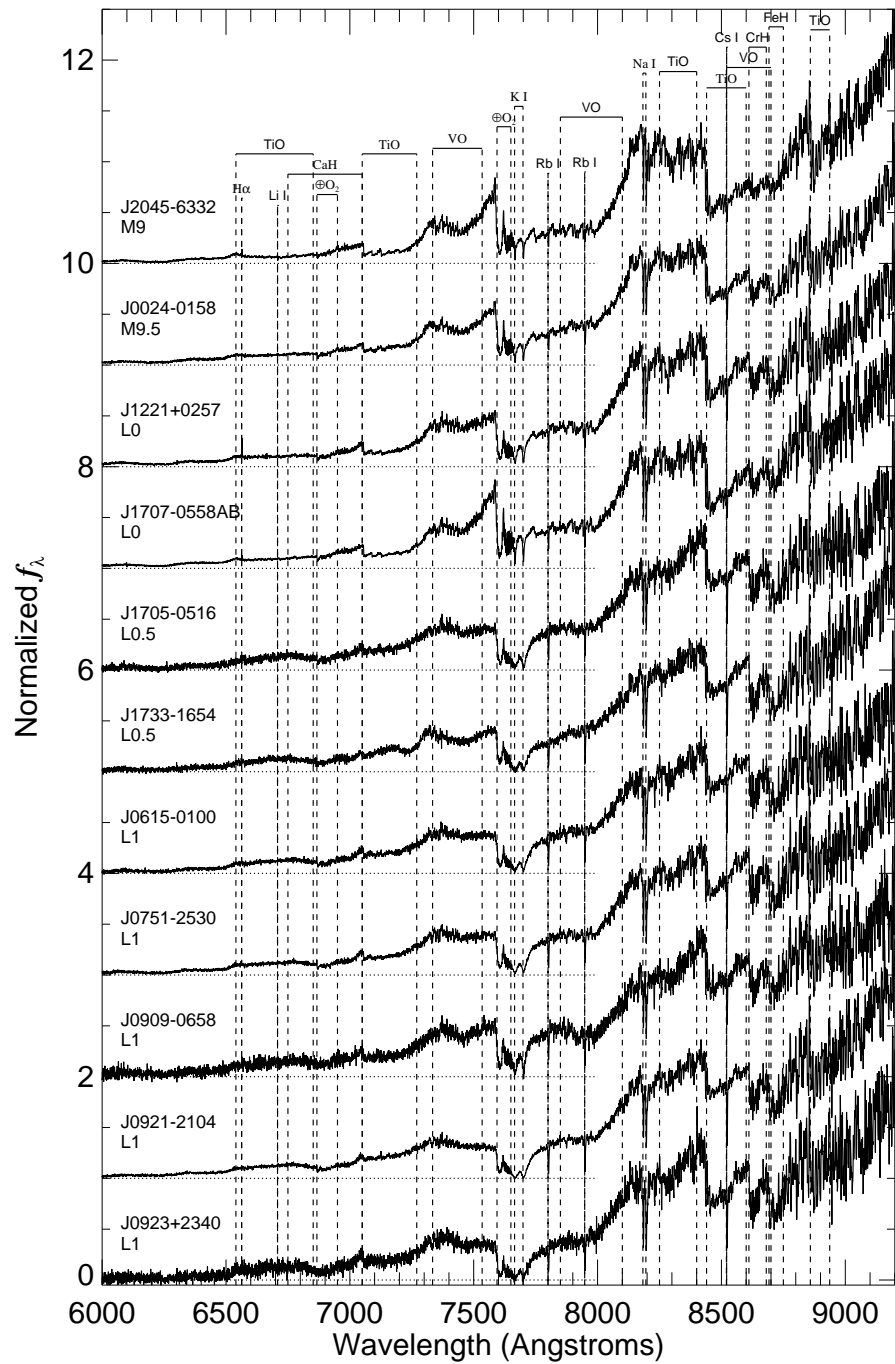


Fig. 3.— Cont.

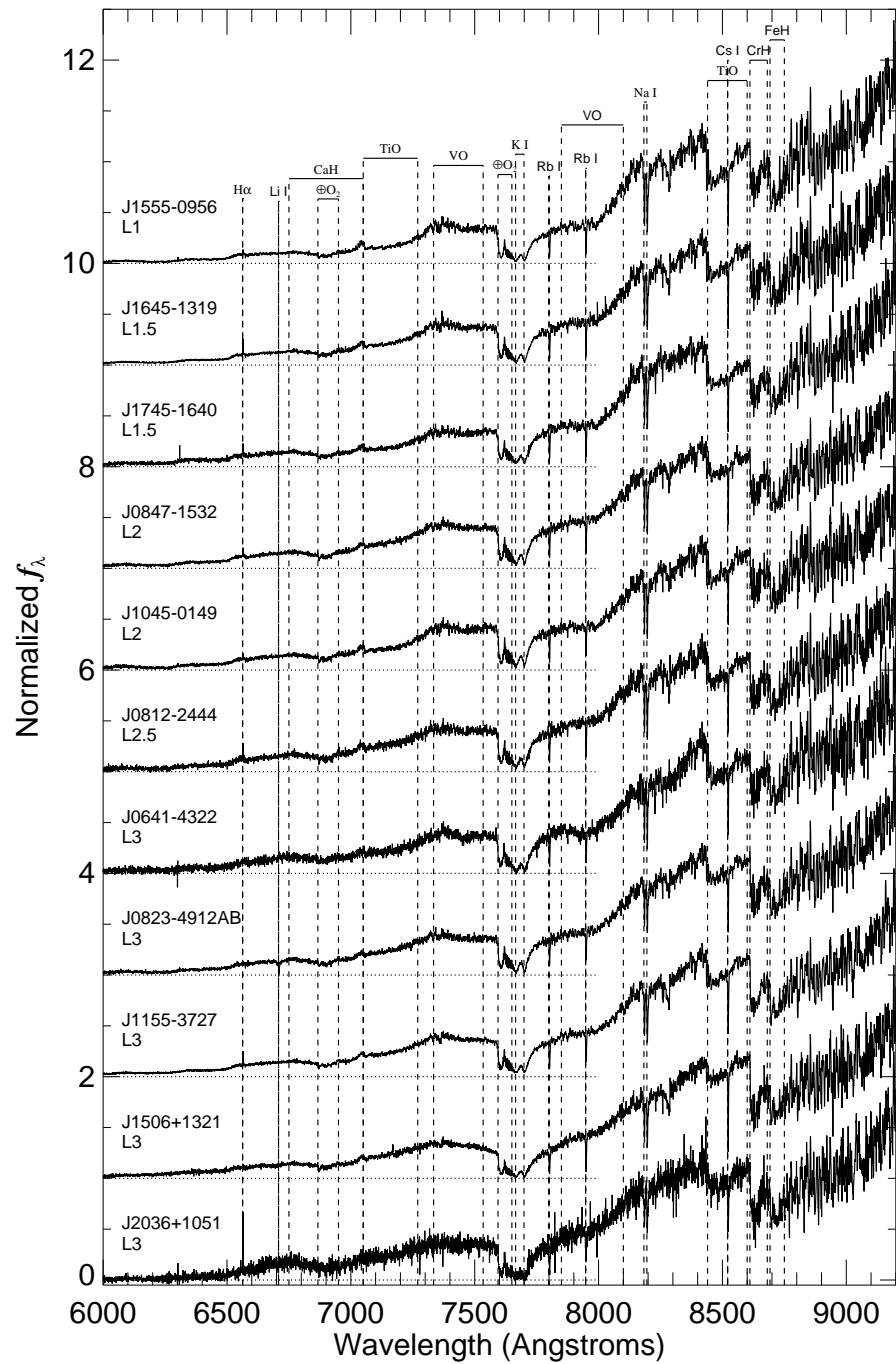


Fig. 3.— Cont.

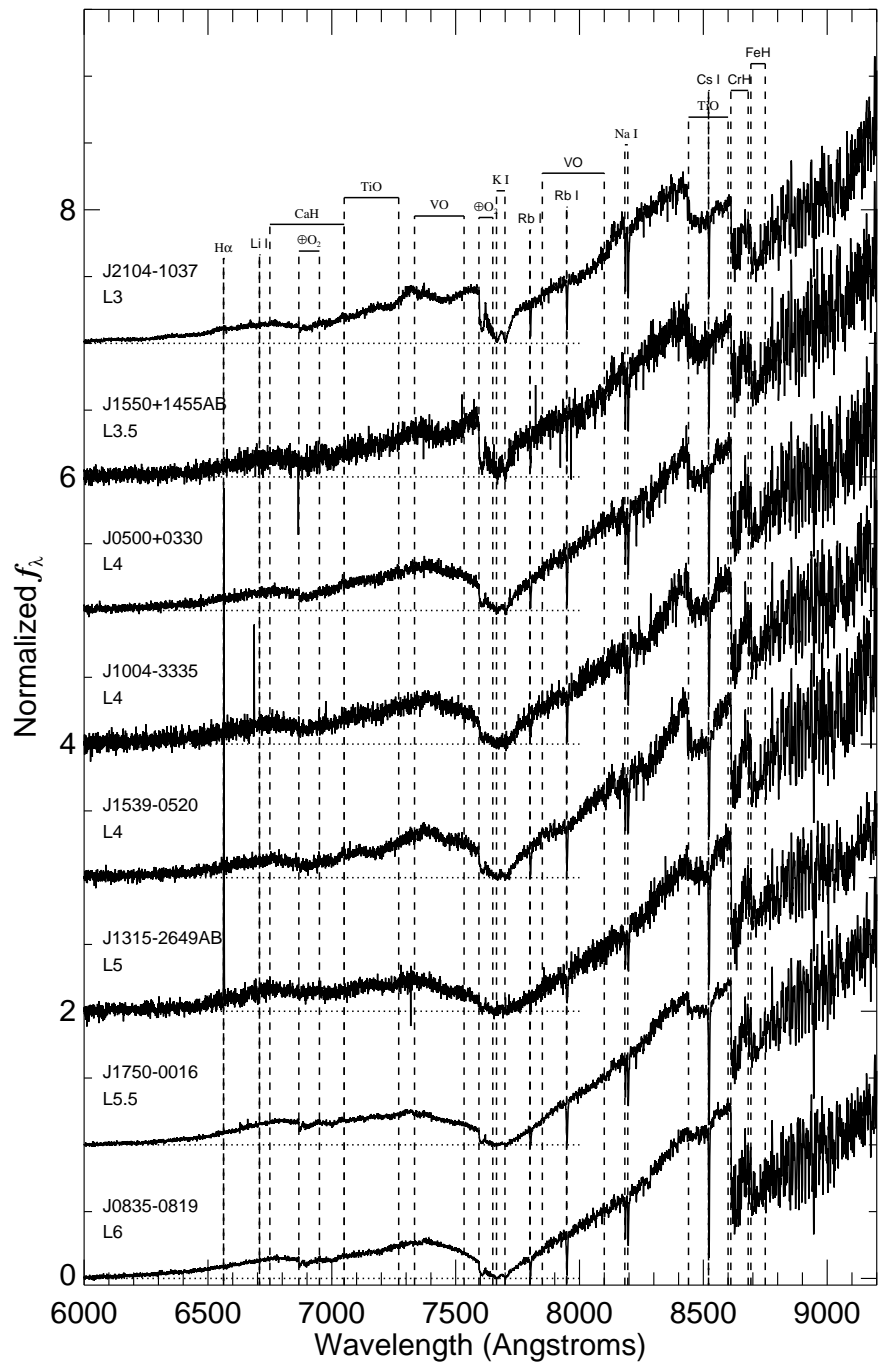


Fig. 3.— Cont.

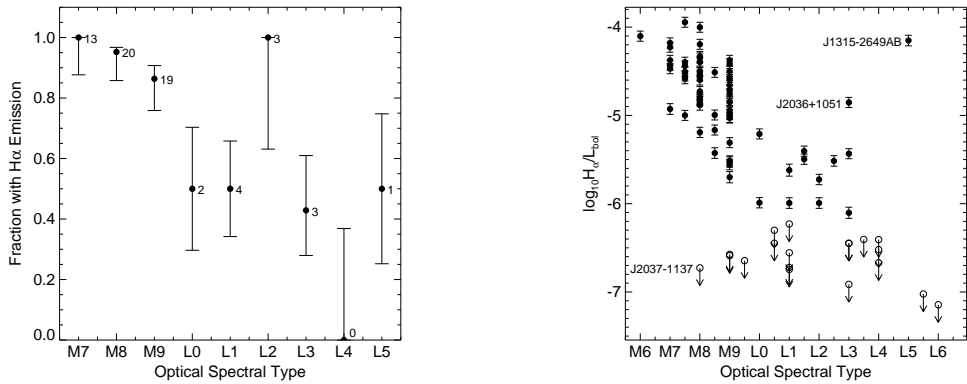


Fig. 4.— (Left): Fraction of sources in our sample exhibiting H α emission as a function of spectral type. Uncertainties are based on binomial statistics, with the numbers next to each point indicating the total number of objects exhibiting H α in that subtype bin. (Right): $\log_{10} L_{H\alpha}/L_{bol}$ as a function of spectral type; upper limits are indicated by downward arrows. The two unusually active L dwarfs J2036+1051 and J1315–2649 are labeled, as is the unusually inactive M8 dwarf J2037–1137.

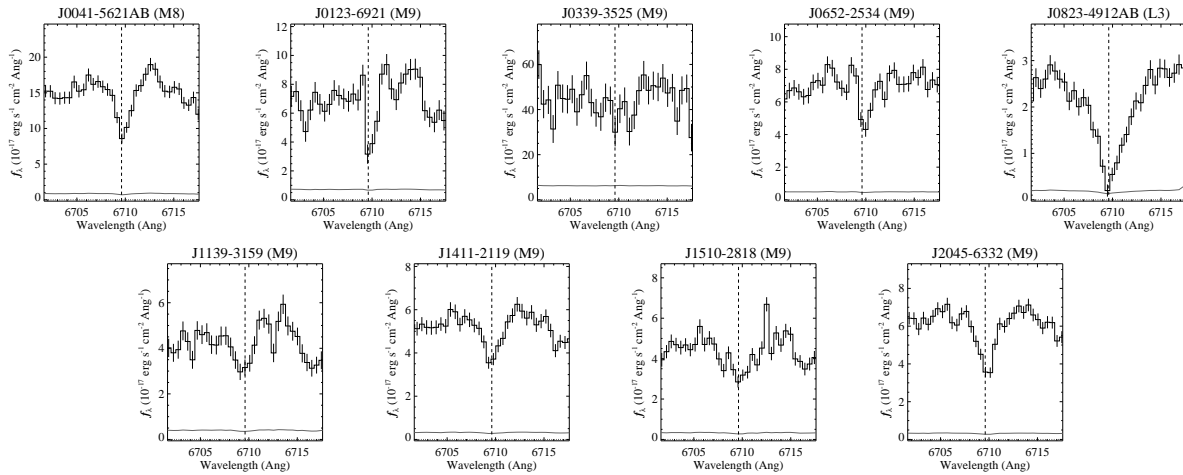


Fig. 5.— 6700–6720 Å spectra of nine sources in our sample that show significant or marginal absorption from the 6710 Å Li I line, indicating that they are young brown dwarfs.

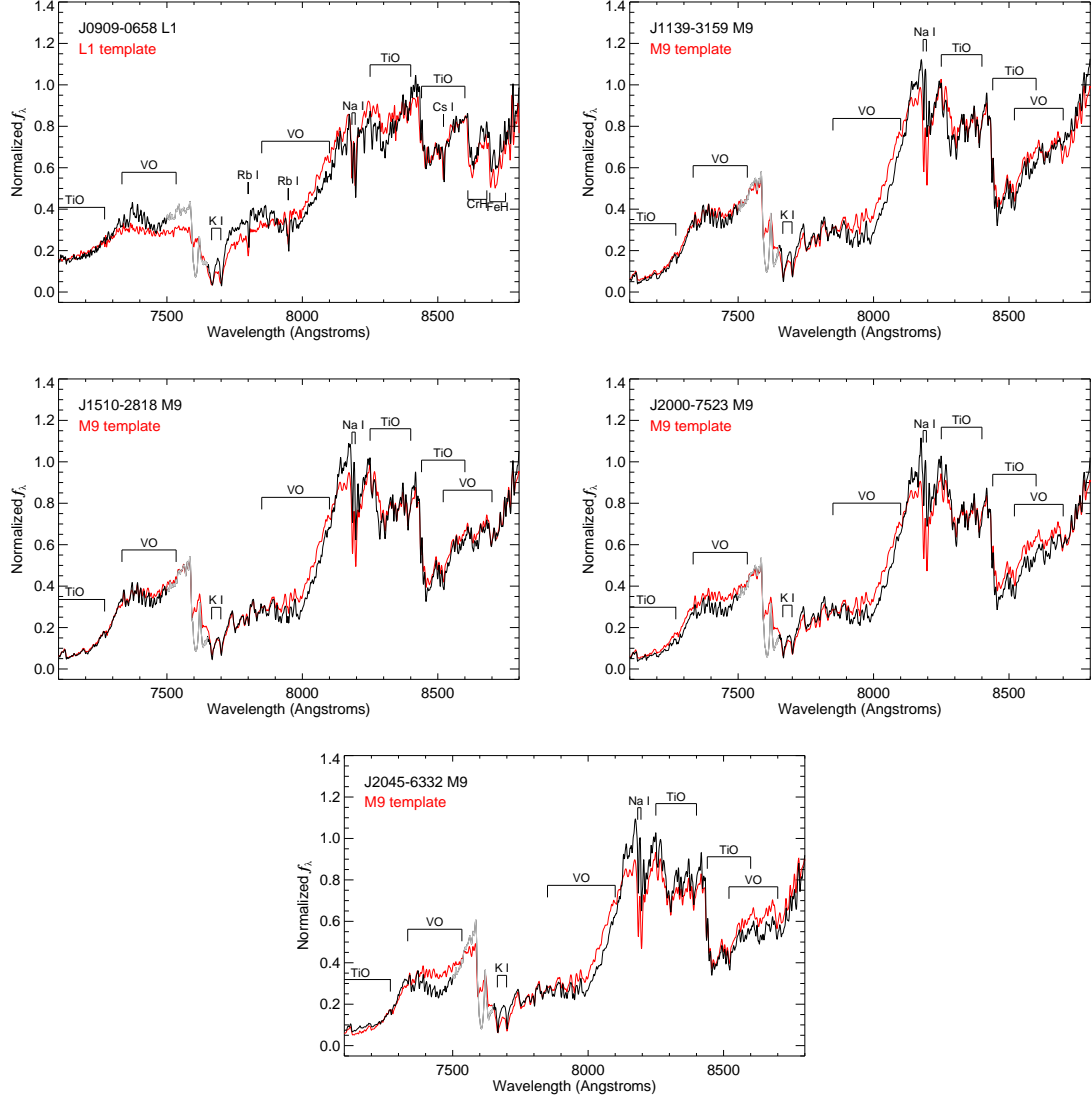


Fig. 6.— 7100–8800 Å spectra of five sources (black) exhibiting strong features of low surface gravity, compared to equivalently-classified SDSS templates (red). Spectra are normalized at 8200 Å; the 7500–7600 Å region affected by poor flux calibration is indicated in gray and should be ignored.

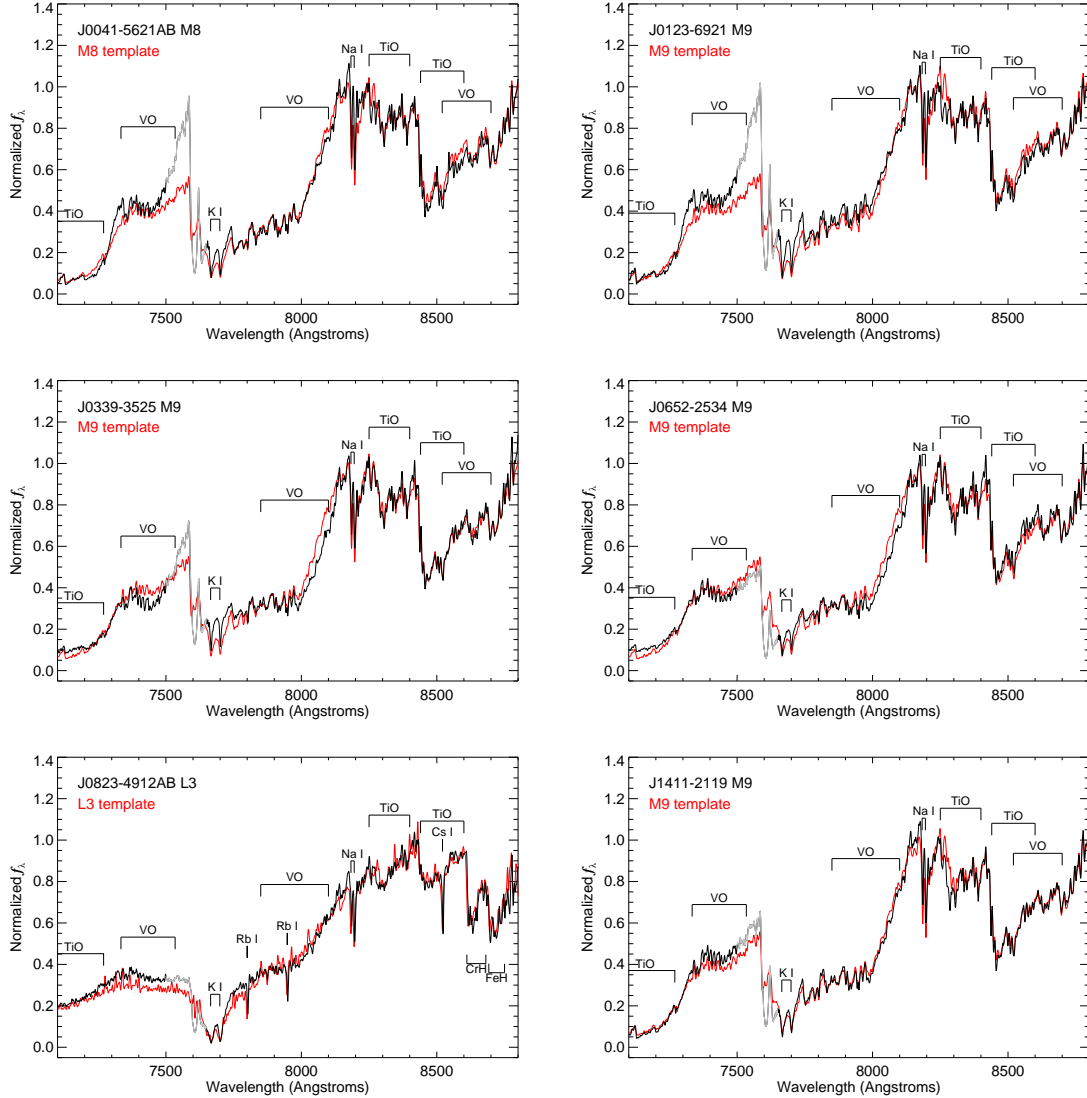


Fig. 7.— Same as Figure 6, showing sources exhibiting weak signatures of low surface gravity.

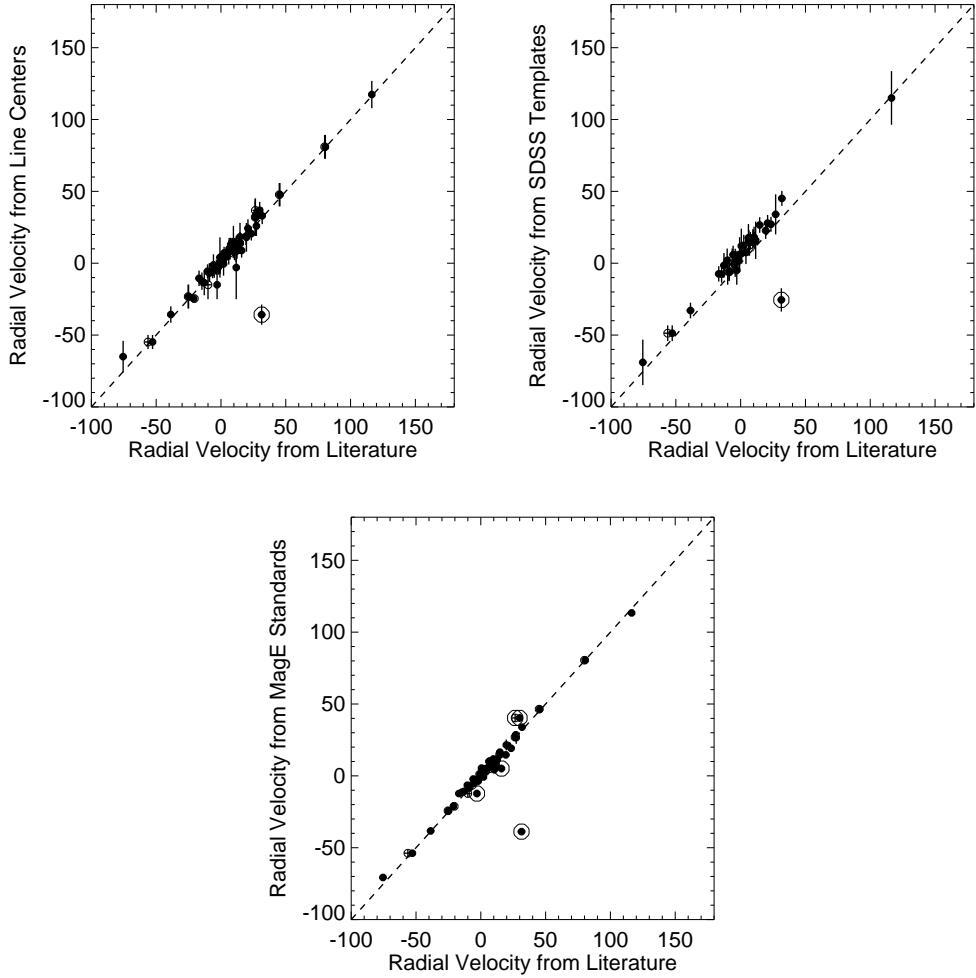


Fig. 8.— Comparison of RVs measured from line centers (upper left panel), cross-correlation with SDSS templates (upper right panel) and cross-correlation with MagE RV standards (lower panel) to previously published high precision measurements ($\leq 3 \text{ km s}^{-1}$; Table 1). The consistent deviant, J0517–3349, is highlighted by an open circle; this appears to be a sign reversal in the RV reported by Reiners & Basri (2008). The other deviants in the lower panel, J0500+0330, J0835+0819 and J2351–2537, are discussed further in Section 3.4.

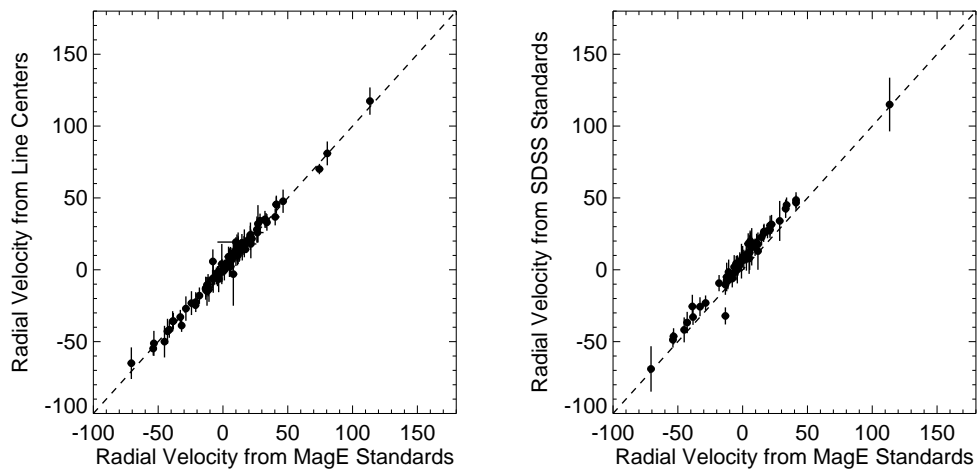


Fig. 9.— Comparison of RV measurements between line centers, SDSS templates, and MagE RV standards.

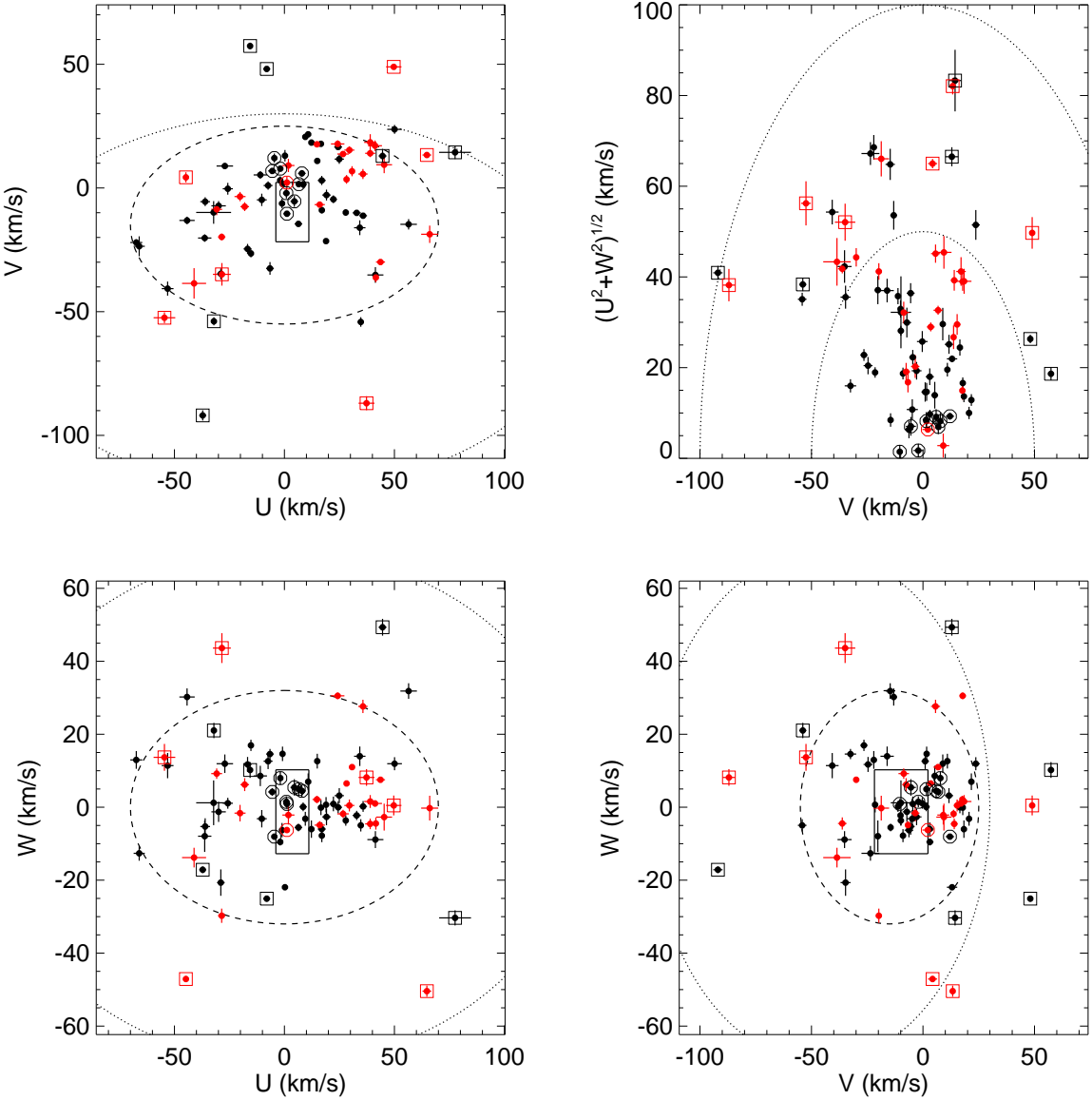


Fig. 10.— UVW space motions for our sample in the Local Standard of Rest. Upper left, lower left and lower right plots compare velocity components to the 2σ velocity means and dispersions of Galactic thin disk (dashed lines) and thick disk (dotted lines) populations from Bensby et al. (2003). Also shown is the “good box” of Zuckerman & Song (2004), a rough locus of nearby YMG members. The upper right panel shows a Toomre plot, with dotted lines delineating 50 km s^{-1} steps of constant $v_{tot} = (U^2 + V^2 + W^2)^{1/2}$. Late-M dwarfs are indicated by black symbols, L dwarfs by red symbols. Sources identified as intermediate thin/thick disk stars are highlighted by open squares; sources exhibiting Li I absorption are highlighted by open circles.

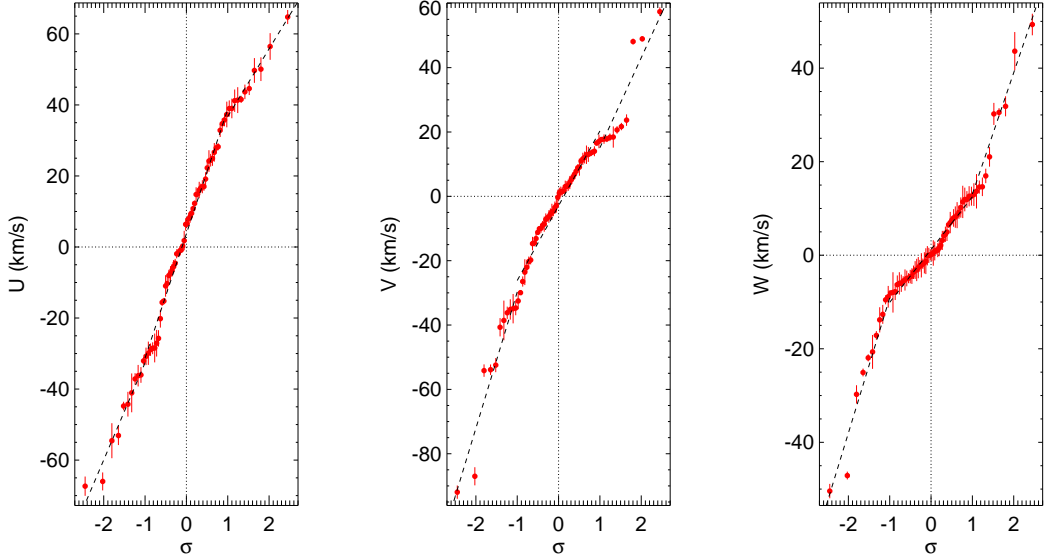


Fig. 11.— Probit plots for U , V , and W velocity components for sources in our sample within 20 pc of the Sun. Individual velocity measurements and uncertainties are indicated in red. Separate linear fits are shown for core ($|\sigma| < 1$) and warm ($|\sigma| > 1$) populations. Dotted lines mark the mean of the velocity distributions ($\sigma = 0$) and zero velocity.

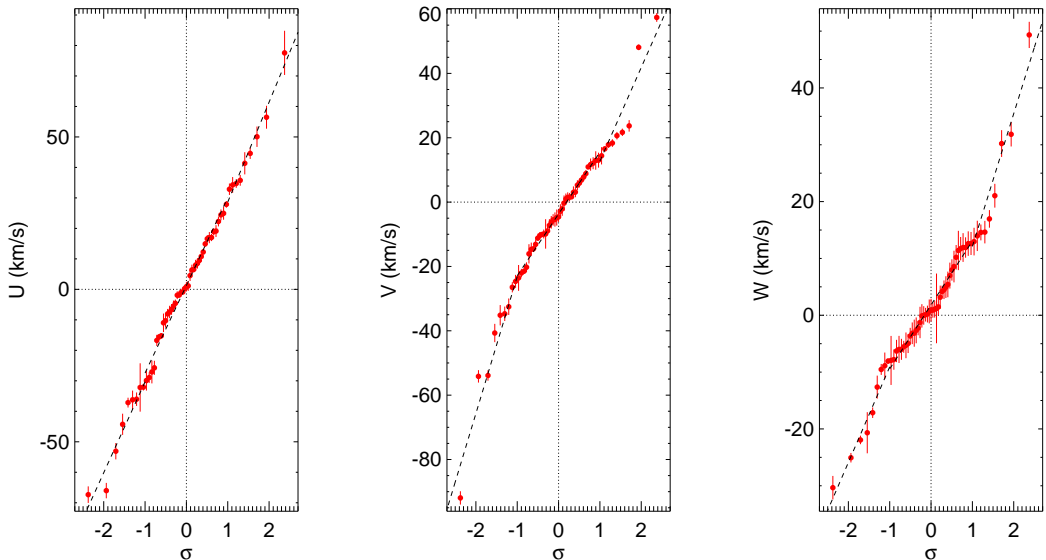


Fig. 12.— Same as Figure 11 for the late-M dwarfs in our sample.

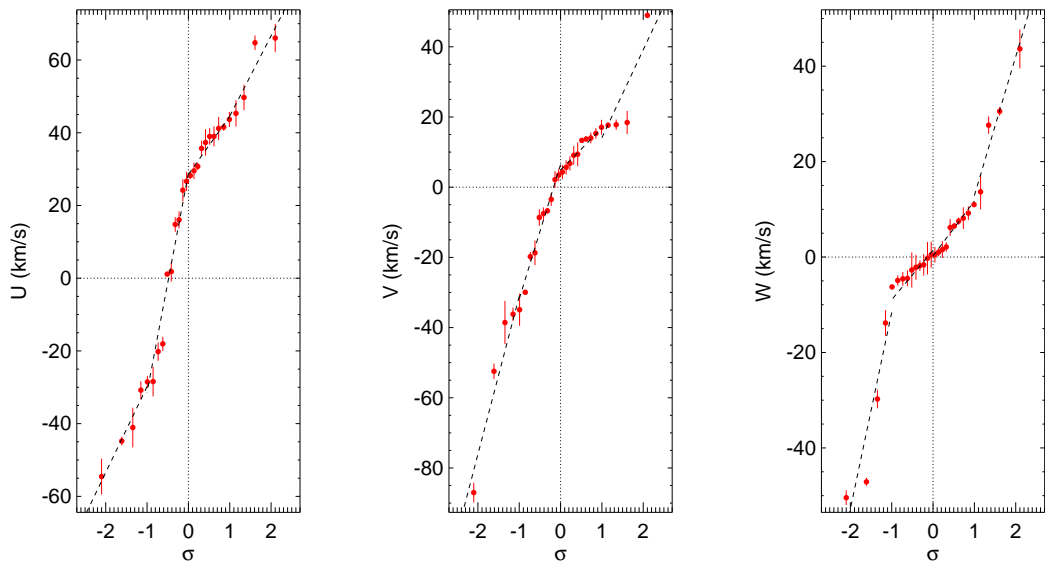


Fig. 13.— Same as Figure 11 for the L dwarfs in our sample. In this case, separate fits are made within the core population for $\sigma > 0$ and $\sigma < 0$, which have significantly different linear slopes.

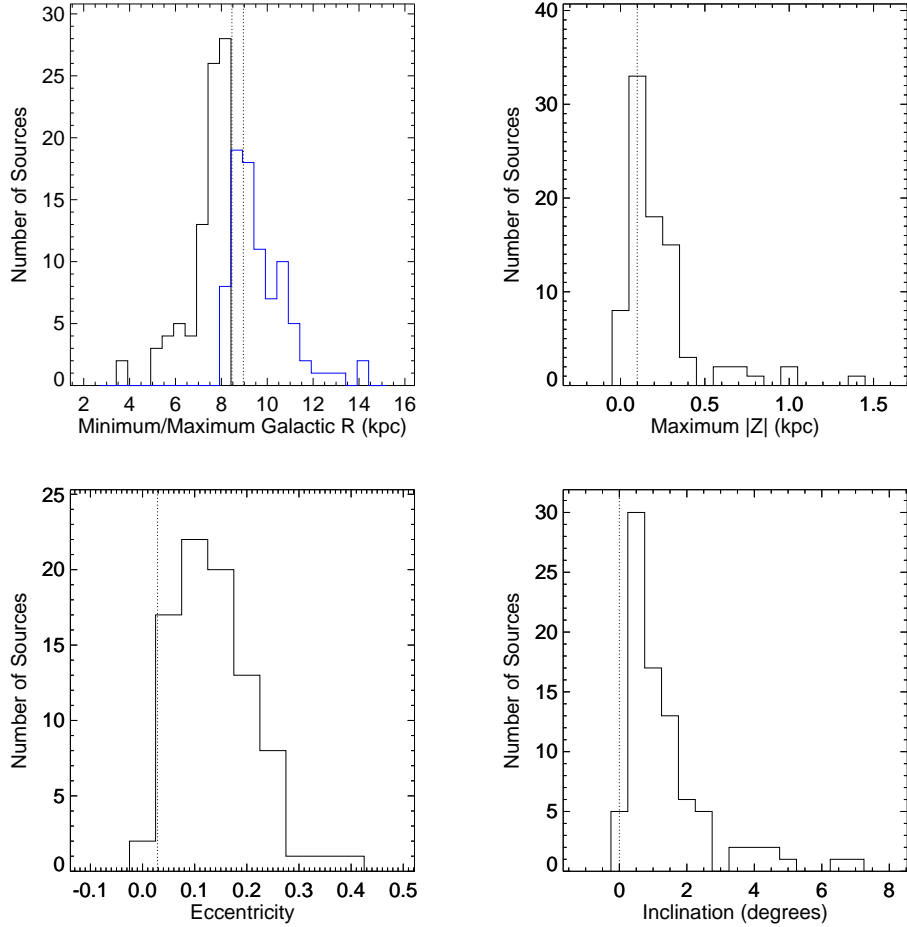


Fig. 14.— Distribution of Galactic orbital parameters for sources in our sample: (upper left) minimum (black) and maximum (blue) Galactic radius, (upper right) maximum absolute vertical displacement, (lower left) orbital eccentricity, and (lower right) orbital inclination. Solar values based on the same orbit calculations and assuming the current position ($R_{\odot} = 8.43$ kpc, $|Z_{\odot}| = 0.027$ kpc) and motion of the Sun relative to the LSR are indicated by the dashed lines.

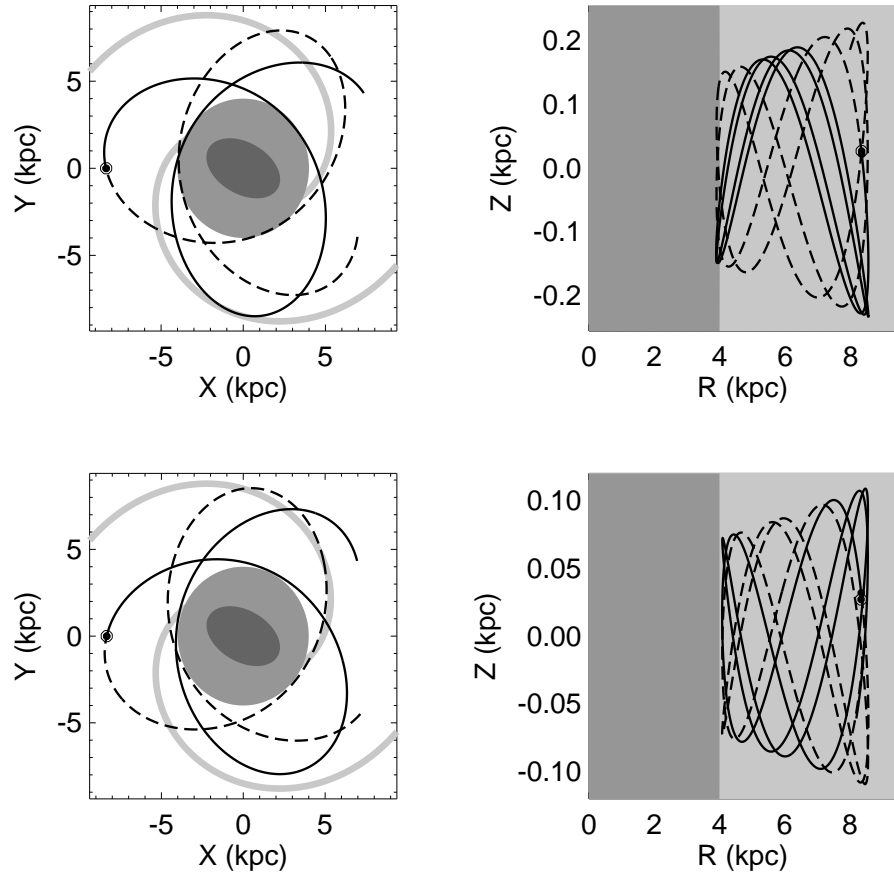


Fig. 15.— Galactic orbits of the thick disk M8.5 J0707–4900 (top) and the intermediate thin/thick disk L1 J0921–2104 (bottom). Panels show the orbit over the past (dashed line) and future (solid line) 250 Myr about the current epoch (solid point, near the current position of the Sun), projected onto the Galactic plane (left) and in cylindrical coordinates (right). Representations of the Galactic bar (darkest gray), bulge (gray), and thin disk/major spiral arms (lightest gray) based on Benjamin (2008); Binney & Tremaine (2008) and Wegg & Gerhard (2013) are also shown.

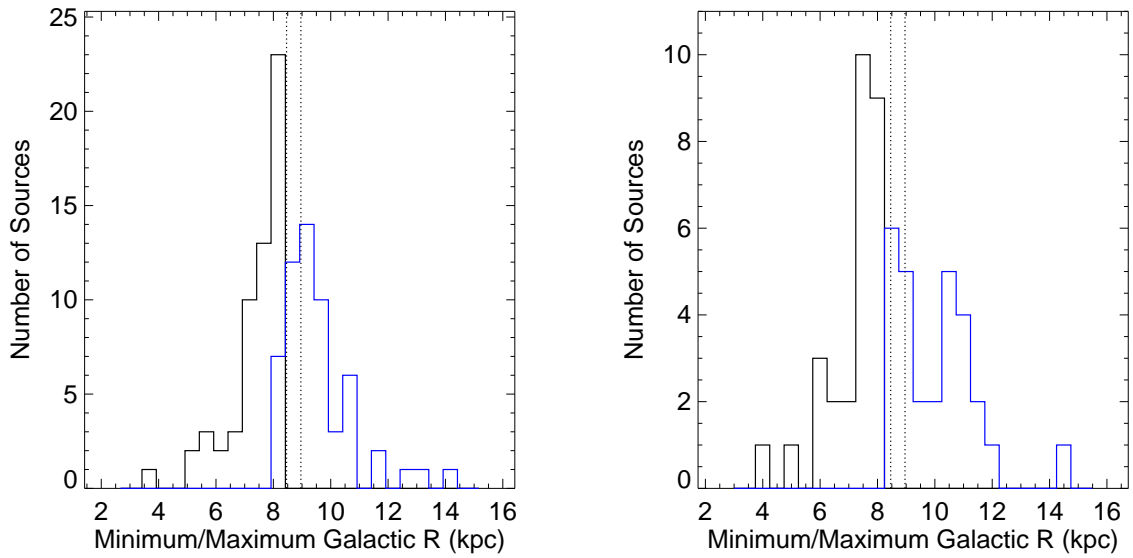


Fig. 16.— Comparison of R_{min} (black) and R_{max} (blue) distributions for the late-M dwarfs (left) and L dwarfs (right) in our sample. Solar values are indicated by vertical dashed lines.

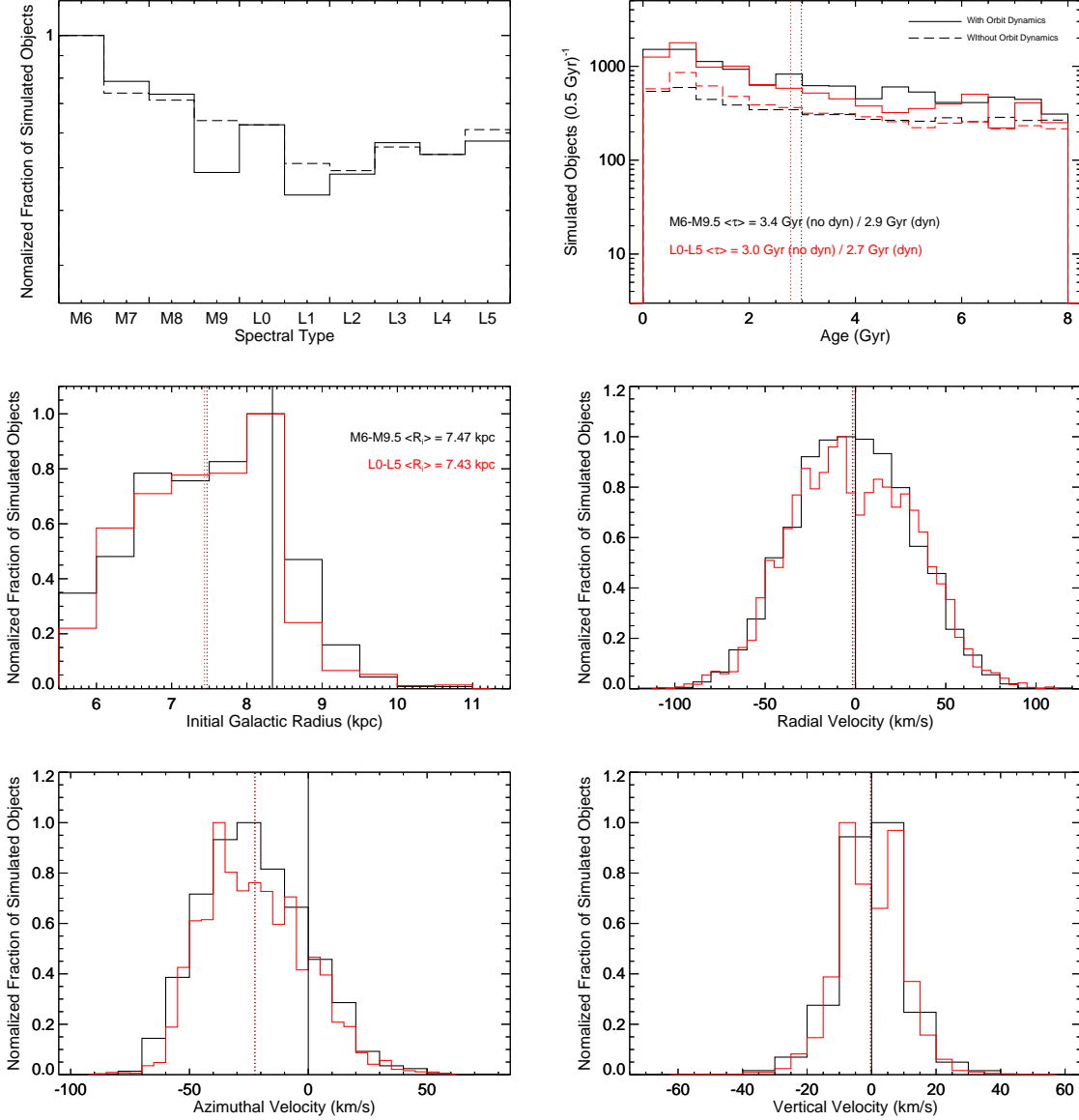


Fig. 17.— Summary of population synthesis, dynamical evolution and local selection simulation for $\beta = 0.0$ and $\alpha = 0.5$. Distributions for M6–M9.5 dwarfs are indicated in black, L0–L5 dwarfs in red. (Upper left): Spectral type distribution before (dashed) and after (solid) dynamical selection. (Upper right): Age distribution before (dashed) and after (solid) dynamical selection; vertical dotted lines indicate mean ages. (Middle left): Initial Galactic radii after dynamical selection. Dotted vertical lines indicate mean radii, solid vertical line indicates the Solar radius (8.43 kpc). (Middle right, lower left, lower right): Galactic azimuthal, radial and vertical velocities in the Local Standard of Rest after dynamical evolution and local selection. Vertical solid lines indicate zero mean velocity, vertical dotted lines indicate mean velocities of the spectral class subsamples.

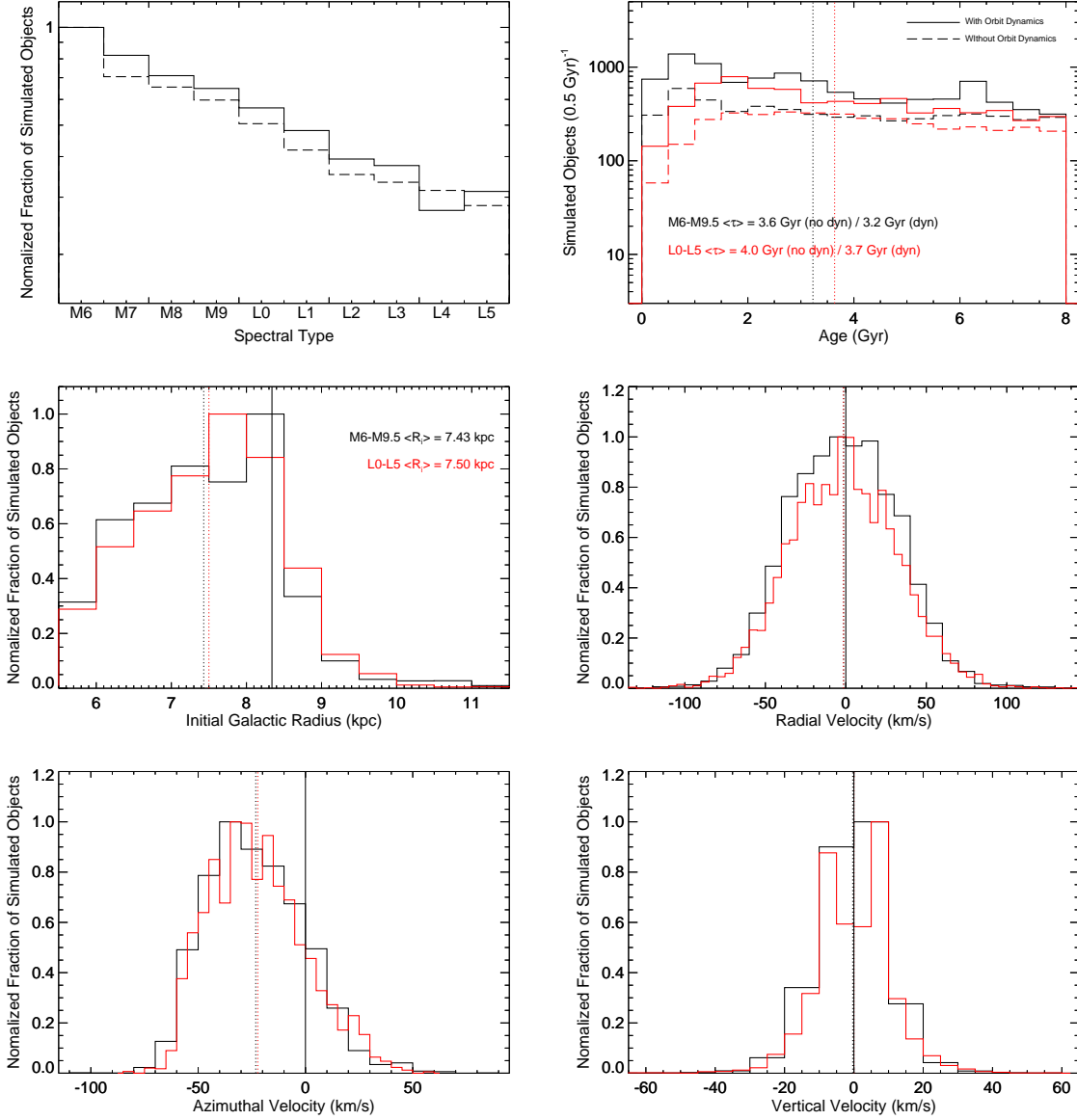


Fig. 18.— Same as Figure 17 but for $\beta = 0.5$ for $M < 0.07 M_{\odot}$ and $\beta = 0.0$ for $M > 0.07 M_{\odot}$. Note the loss of young L (brown) dwarfs in this sample, resulting in an older L dwarf population on average.

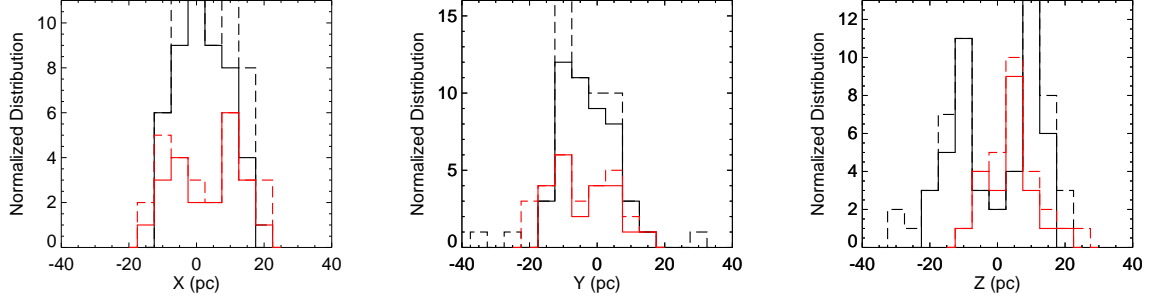


Fig. 19.— Distribution of M dwarfs (black) and L dwarfs (red) in X Y Z spatial coordinates. Dashed-line histograms show the distributions for all sources, solid-line histograms show the distributions for those sources within 20 pc of the Sun.

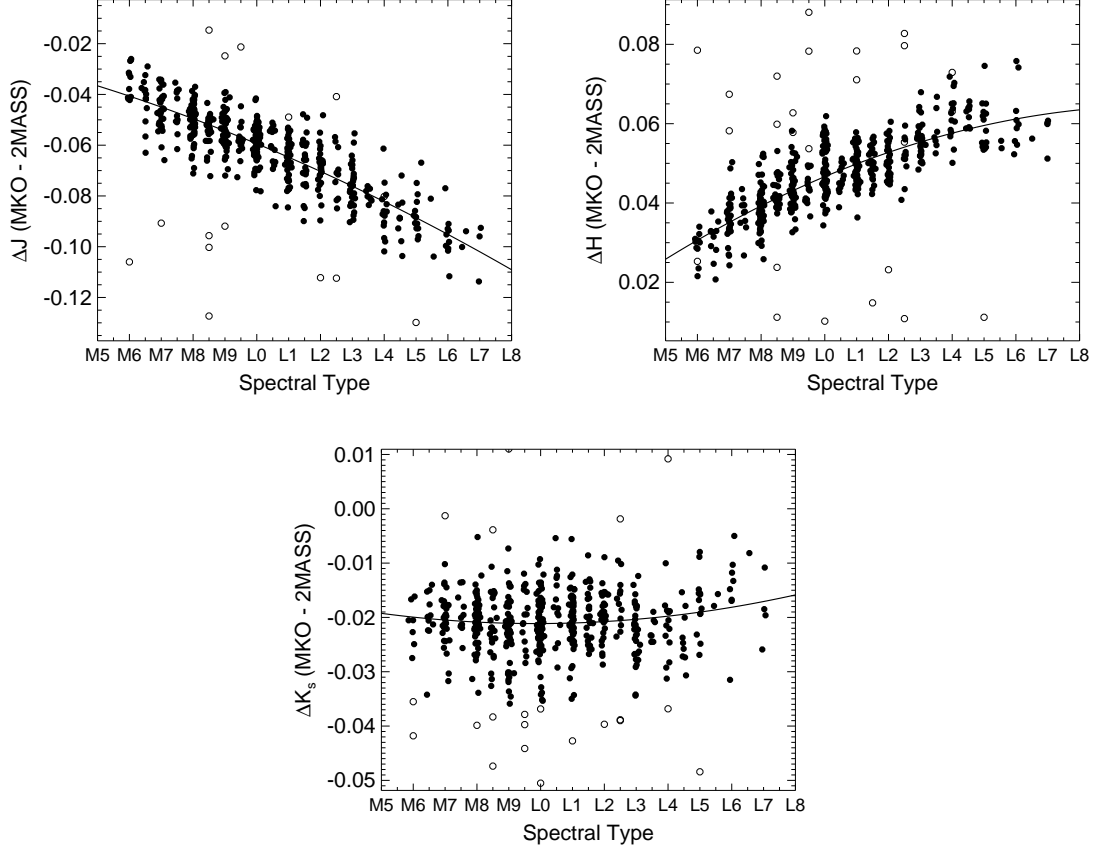


Fig. 20.— Magnitude differences between 2MASS and MKO JHK_s filter systems for M6-L7 dwarfs, based on spectrophotometric measurements from 533 optically-classified, high S/N near-infrared spectra in the SpeX Prism Library. Each point has a random offset in spectral type added to distinguish sources. Open circles are outliers rejected from the second-order polynomial fits.

Table 1. Observational Sample

Source Name	Coordinates (J2000)	Optical SpT	2MASS <i>J</i> (mag)	<i>J</i> − <i>K_s</i> (mag)	μ_{α} (mas yr ^{−1})	μ_{δ} (mas yr ^{−1})	Published		Flag ^b	References ^c
							<i>d</i> ^a (pc)	<i>RV</i> (km s ^{−1})		
J0004−2058	00 04 41.44 −20 58 29.8	M9	12.40±0.02	1.01±0.03	756±8	95±10	(15.5±1.0)	...		28
J0024−0158	00 24 24.63 −01 58 20.1	M9.5	11.99±0.04	1.45±0.04	−80±4	132±6	11.6±0.5	10±3	UR	48; 51
J0041−5621AB	00 41 35.38 −56 21 12.7	M8	11.96±0.02	1.10±0.03	98±6	−50±8	(20.7±1.8)	2.4±1	Li, VB, THA	45; 55, 51
J0102−3737	01 02 51.00 −37 37 43.8	M9	11.13±0.02	1.06±0.03	1456±3	262±4	12.2±0.4	...		34
J0109−0343	01 09 51.17 −03 43 26.4	M8	11.69±0.02	1.27±0.03	360±2	18±2	9.6±0.2	−10.4±0.6	UR	34; 55, 51
J0123−6921	01 23 11.25 −69 21 37.9	M9	12.32±0.02	1.00±0.04	77±2	−25±9	42±5	7.5±0.3	Li, THA	39; 55, 51
J0148−3024	01 48 38.64 −30 24 39.6	M7.5	12.30±0.02	1.08±0.03	−86±8	51±8	(18.8±2.0)	10±3		28; 51
J0248−1651	02 48 41.00 −16 51 21.6	M8	12.55±0.02	1.13±0.03	20±9	−273±12	16.1±1.3	4±3		31; 51
J0331−3042	03 31 30.25 −30 42 38.3	M9	11.36±0.02	1.10±0.03	57±1	−403±6	(9.6±0.6)	23±3		32; 51
J0339−3525	03 39 35.21 −35 25 44.0	M9	10.73±0.02	1.18±0.03	305.8±0.4	270.5±0.4	6.41±0.04	6±3	Li, CAS	38; 56
J0351−0052	03 51 00.04 −00 52 45.2	M7.5	11.30±0.02	1.07±0.03	8.6±1.1	−472.4±1	14.7±0.4	−15±3		42, 49; 51
J0500+0330	05 00 21.00 +03 30 50.1	L4	13.67±0.02	1.61±0.03	13±3	−349.9±1.8	13.5±0.4	15.94±0.16	UB	1; 38; 52
J0517−3349	05 17 37.66 −33 49 02.7	M8	12.00±0.02	1.17±0.03	428±5	−306±4	(15.0±1.4)	31±3		32; 51
J0544−2433	05 44 11.50 −24 33 01.8	M9	12.53±0.02	1.07±0.03	140±30	−690±30	(16.4±1.1)	21±3		22; 51
J0615−0100	06 15 49.34 −01 00 41.5	L1	13.75±0.03	1.21±0.04	226±12	−75±14	(22.4±1.5)	...		2; 23
J0641−4322	06 41 18.40 −43 22 32.9	L3	13.75±0.03	1.30±0.04	215±9	611±9	17.9±1.9	...	UB	1; 24
J0652−2534	06 52 19.77 −25 34 50.5	M9	12.76±0.02	1.24±0.03	−235.6±0.8	82.5±1.3	15.7±0.2	...		2; 38
J0707−4900	07 07 53.27 −49 00 50.3	M8.5	13.23±0.03	1.12±0.04	−10±5	391±7	16.4±0.8	116.4±1.5		21, 49; 59
J0751−2530	07 51 16.45 −25 30 43.2	L1	13.16±0.02	1.17±0.03	−877.7±0.9	142.2±1.4	16.9±0.2	...	UB	38
J0812−2444	08 12 31.70 −24 44 42.3	L2.5	13.82±0.03	1.43±0.04	137.6±1.1	−140.1±1.1	22±0.5	...		2; 38
J0823−4912AB	08 23 03.13 −49 12 01.2	L3	13.55±0.03	1.49±0.04	−154.30±0.12	7.46±0.09	20.76±0.08	...	AB	2; 46
J0830+0947	08 30 32.56 +09 47 15.3	M7.5	11.89±0.02	1.13±0.03	−500±3	−449±4	16.9±1.3	...		35
J0835−0819	08 35 42.56 −08 19 23.7	L6	13.17±0.02	2.03±0.03	−520±9	285±10	8.5±0.8	29.89±0.06	UR, HYA	3; 24; 52, 53
J0847−1532	08 47 28.72 −15 32 37.2	L2	13.51±0.03	1.45±0.04	133.6±1.2	−198.8±1	17±0.3	2.02±0.1		3; 38; 52
J0853−0329	08 53 36.19 −03 29 32.1	M9	11.21±0.03	1.27±0.04	−515.1±0.2	−193.6±0.4	8.48±0.05	6±3	UR	38; 51, 56
J0902+0033	09 02 06.90 +00 33 19.5	M7	12.11±0.02	0.95±0.03	−466±3	−97±3	(19±2)	48±5		26; 60
J0909−0658	09 09 57.49 −06 58 18.6	L1	13.89±0.02	1.35±0.04	−184±3	21±3	24±2	27±3		4; 24; 56
J0921−2104	09 21 14.10 −21 04 44.6	L1	12.78±0.02	1.09±0.03	244±16	−908±17	(14.3±1.0)	80.54±0.11	UB	1; 21; 52, 53
J0923+2340	09 23 08.61 +23 40 15.2	L1	13.85±0.03	1.04±0.04	294±36	−396±20	(23.4±1.6)	−30±4	UB	27; 57
J0949+0806	09 49 22.23 +08 06 45.0	M8.5	12.31±0.02	1.10±0.04	40.2±1.9	−885.8±1.2	16.6±0.5	...		38
J1003−0105	10 03 19.18 −01 05 07.9	M8	12.33±0.02	1.09±0.03	−490±19	22±19	(17.3±1.5)	35±5		41; 60
J1004−3335	10 04 39.29 −33 35 18.9	L4	14.48±0.04	1.56±0.04	243±4	−253±4	18.2±2	...	UB	5; 24
J1045−0149	10 45 24.00 −01 49 57.6	L2	13.16±0.02	1.38±0.03	−492±9	−5±9	(14.9±1.2)	6.31±0.1	HYA	5; 28; 52, 53
J1048−3956	10 48 14.63 −39 56 06.2	M8	9.54±0.02	1.09±0.03	−1176±5	−993±5	4±0.3	−13±3		34; 51
J1054+1214	10 54 41.68 +12 14 08.4	M7.5	12.46±0.02	1.01±0.03	103±18	−80±19	(20±2)	...		21
J1055+0808	10 55 47.33 +08 08 42.7	M9	12.55±0.03	1.18±0.04	−350±20	−100±30	(16.6±1.1)	19±5		22; 60
J1119+0828	11 19 46.47 +08 20 35.6	M7	12.77±0.02	0.87±0.04	368±11	−336±10	(26±3)	−39±5		28; 60
J1121−1313AB	11 21 49.24 −13 13 08.4	M8.5	11.93±0.02	1.19±0.03	−464.2±0.7	−57.0±0.7	15.2±0.5	32±3	VB, RV	42; 51
J1134+0022	11 34 54.93 +00 22 54.1	M9	12.85±0.02	1.18±0.03	401±21	−343±21	(19.0±1.3)	...		21
J1139−3159	11 39 51.16 −31 59 21.4	M9	12.69±0.03	1.18±0.03	−81±4	−28±2	42±5	12±2	Li, TWA	5; 50; 56
J1155−3727	11 55 39.52 −37 27 35.0	L3	12.81±0.02	1.35±0.03	67±5	−778±5	9.6±0.4	45.47±0.11	UB	1; 25; 52, 53
J1221+0257	12 21 27.70 +02 57 19.8	L0	13.17±0.02	1.22±0.04	−115±30	−18±27	(19.5±1.2)	−8.79±0.14		27; 52, 53
J1224−1238	12 24 52.22 −12 38 35.2	M9	12.57±0.02	1.22±0.04	−263±11	−187±11	17±1.2	−6±3		31; 51
J1252+0252	12 52 22.64 +02 52 05.8	M7	12.50±0.02	0.99±0.04	36±4	−278±4	(23±3)	30±5		26; 60
J1309−2330	13 09 21.85 −23 30 35.0	M8	11.79±0.02	1.12±0.03	26.5±1.7	−379.5±1.1	14.4±0.3	19±3		6; 38; 51
J1315−2649AB	13 15 30.94 −26 49 5.13	L5	15.20±0.05	1.73±0.07	−682±13	−282±14	(22±2)	...	VB	21
J1332−0441	13 32 24.42 −04 41 12.6	M7.5	12.37±0.03	1.09±0.03	59±9	14±9	(19±2)	−17±3		28; 51
J1411−2119	14 11 21.31 −21 19 50.3	M9	12.44±0.02	1.11±0.03	−73±8	−70±8	(15.8±1.1)	−1±3	Li	33; 51

Table 1—Continued

Source Name	Coordinates (J2000)	Optical SpT	2MASS <i>J</i> (mag)	<i>J</i> − <i>K_s</i> (mag)	μ_{α} (mas yr ^{−1})	μ_{δ} (mas yr ^{−1})	<i>d</i> ^a (pc)	Published <i>RV</i> (km s ^{−1})	Flag ^b	References ^c
J1422+2116	14 22 24.24 +21 16 07.6	M7	12.44±0.03	0.99±0.03	93±4	−3±4	(22±3)	...		26
J1440+1339	14 40 22.93 +13 39 23.0	M7	12.40±0.02	1.06±0.03	−138.4±1.5	−300.8±1.1	22.2±0.6	−5±3		38; 51
J1456−2809	14 56 38.31 −28 09 47.3	M7	9.97±0.03	1.04±0.04	−470±10	−844±12	6.56±0.09	1±3		48; 49; 51
J1500−0039	15 00 26.35 −00 39 28.1	M6	11.59±0.03	0.95±0.04	−186±3	61±3	(20±4)	−17±5		26; 54
J1501+2250	15 01 08.18 +22 50 02.0	M9	11.87±0.02	1.16±0.03	−24.6±0.3	−57.9±0.4	10.59±0.07	...		36
J1504−2355	15 04 16.21 −23 55 56.4	M7.5	12.01±0.03	0.98±0.04	−339±14	−85±3	(16.3±1.6)	...		7; 29
J1506+1321	15 06 54.41 +13 21 06.0	L3	13.37±0.02	1.62±0.03	−1088±12	4±10	(13.8±1.3)	−0.68±0.11		47; 52, 53
J1510−0241	15 10 16.85 −02 41 07.8	M9	12.61±0.02	1.27±0.03	−404±12	24±6	16.4±1.3	...	UR	48
J1510−2818	15 10 47.86 −28 18 17.4	M9	12.84±0.03	1.15±0.04	−124±5	−46±5	(19.0±1.3)	...		43
J1534−1418	15 34 57.04 −14 18 48.6	M8	11.38±0.02	1.08±0.03	−915±3	−311.0±1	(11.2±1.0)	−76±3		32; 51
J1539−0520	15 39 41.89 −05 20 42.8	L4	13.92±0.03	1.35±0.04	592.9±1.1	105.6±1.8	16.3±0.4	27.3±0.2	UB	8; 38; 52
J1550+1455AB	15 50 08.40 +14 55 17.1	L3.5	14.78±0.04	1.52±0.06	116±26	−169±14	(34±3)	...	VB	27
J1553+1400	15 53 19.93 +14 00 33.7	M9	13.05±0.02	1.23±0.03	−643±8	66±9	(20.9±1.5)	...		5; 28
J1555−0956	15 55 15.73 −09 56 05.5	L1	12.56±0.02	1.11±0.03	933.5±1.9	−781±2	13.4±0.2	14.84±0.1		38; 52, 53
J1607−0442	16 07 31.23 −04 42 09.1	M9	11.90±0.02	1.18±0.03	−1.4±1.9	−414.6±1.2	15.7±0.4	...		38
J1615+0546	16 15 42.45 +05 46 40.0	M9	12.88±0.02	1.14±0.03	136±5	−81±5	(19.2±1.3)	...		5; 44
J1645−1319	16 45 22.11 −13 19 51.6	L1.5	12.45±0.03	1.31±0.04	−352.6±1.1	−799.5±0.7	11.1±0.1	26.58±0.06		9; 38; 52, 53
J1705−0516	17 05 48.34 −05 16 46.2	L0.5	13.31±0.03	1.28±0.04	121.5±1.7	−111.3±1.8	18.2±0.6	12.19±0.11		10; 38; 52, 53
J1707−0558AB	17 07 23.43 −05 58 24.9	L0	12.05±0.02	1.34±0.03	100±8	3±5	(16.5±1.0)	...	VB, UMA	2; 40
J1733−1654	17 33 42.27 −16 54 50.0	L0.5	13.53±0.05	1.18±0.06	81±15	−48±15	(21.6±1.4)	...		2; 23
J1745−1640	17 45 34.66 −16 40 53.8	L1.5	13.65±0.03	1.24±0.04	116±5	−111±19	(20.0±1.4)	...	UB	11; 23
J1750−0016	17 50 24.84 −00 16 15.1	L5.5	13.29±0.02	1.45±0.03	−398±3	195±3	9.2±0.2	...	UB	12; 24
J1845−6357	18 45 05.41 −63 57 47.5	M8.5	9.54±0.02	1.04±0.03	2591.9±1.8	617±3	3.85±0.02	...		30
J2000−7523	20 00 48.41 −75 23 07.0	M9	12.73±0.03	1.22±0.04	60.3±1.9	−106±10	(18.0±1.2)	11.8±1	BPIC	1; 28; 55
J2036+1051	20 36 03.16 +10 51 29.5	L3	13.95±0.03	1.50±0.04	−132±17	−184±18	(18.1±1.6)	19.7±0.5		21; 52
J2037−1137	20 37 07.15 −11 37 56.9	M8	12.27±0.03	1.02±0.03	2±4	−374±8	(16.9±1.5)	−39±3		43; 51
J2045−6332	20 45 02.38 −63 32 06.6	M9	12.62±0.03	1.41±0.04	82±3	−204.3±1.7	24±0.9	0.5±0.5	Li, UR, CAS	3; 38; 55
J2104−1037	21 04 14.91 −10 37 36.9	L3	13.84±0.03	1.47±0.04	594.8±1.6	−290±2	18.9±0.6	−21.09±0.12		38; 52, 53
J2120+1021	21 20 33.87 +10 21 59.1	M8	13.54±0.03	1.12±0.04	121±10	−30±11	(30±3)	−31±5		9; 28; 60
J2200−3038AB	22 00 02.01 −30 38 32.7	M8	13.44±0.03	1.24±0.04	210±48	−64±21	(41±4)	−25±0.14	VB, UR, HYA	40; 55, 53
J2226−7503	22 26 44.40 −75 03 42.5	M8	12.35±0.02	1.11±0.03	48±19	14±19	(17.4±1.5)	15±3		41; 51
J2306−0502	23 06 29.28 −05 02 28.5	M8	11.35±0.02	1.06±0.03	922±2	−472±3	12.1±0.4	−52.8±0.16		35; 58, 51
J2331−2749	23 31 21.74 −27 49 50.0	M7.5	11.65±0.02	1.00±0.04	77±2	759.7±1.3	14.5±0.4	−4±3		35; 51
J2337−0838	23 37 14.91 −08 38 08.4	M8	12.19±0.03	1.00±0.04	248±19	17±19	(16.3±1.4)	...		41
J2346+1129	23 46 45.99 +11 29 09.4	M8	12.80±0.02	1.19±0.03	−392±8	−82±4	(21.5±1.9)	...	UR	42
J2349+1224	23 49 48.99 +12 24 38.6	M8	12.60±0.02	1.04±0.03	18±19	−209±19	(19.6±1.6)	−2±0.1		41; 58, 51
J2351−2537	23 51 50.44 −25 37 36.7	M8	12.47±0.03	1.20±0.04	387±21	163±9	(18.5±1.7)	−3±1.1	UR	37; 53, 51

^aDistances in parentheses are spectrophotometric estimates based on the *M_J*/spectral type relation of Cruz et al. (2003).^bSource flags: (VB) = visual binary, (RV) = radial velocity variable, (AB) = astrometric binary, (Li) = previous reported Li I absorption, (UB) = unusually blue, (UR) = unusually red, (β PMG) = previously identified member of β Pictoris Moving Group, (CAS) = previously identified member of Caster Moving Group, (HYA) = previously identified member of Hyades Moving Group, (THA) = previously identified member of Tucana Horologium Association, (TWA) = previously identified member of TW Hydriæ Association, (UMA) = previously identified member of Ursa Majoris.^bReferences in order of source discovery, astrometry and previously published RV measurement.

References. — Source discovery: (1) Reid et al. 2008; (2) Phan-Bao et al. 2008; (3) Cruz et al. 2003; (4) Delfosse et al. 1999; (5) Gizis 2002; (6) Hall 2002b; (7)Gizis et al.

2000; (8) Cruz et al. 2007; (9) Kendall et al. 2004; (10) McElwain & Burgasser 2006; (11) Kendall et al. 2007; (12) Biller et al. 2006; Source astrometry: (21) Faherty et al. 2009; (22) Schmidt et al. 2007; (23) Phan-Bao et al. 2008; (24) Andrei et al. 2011; (25) Faherty et al. (2012); (26) York et al. 2000; (27) Schmidt et al. 2010; (28) This paper; (29) Lodieu et al. 2005; (30) Henry et al. 2006; (31) Tinney 1996; (32) Bartlett (2007); (33) Caballero (2007); (34) Costa et al. (2005); (35) Costa et al. 2006; (36) Dahn et al. (2002); (37) Deacon & Hambly (2007); (38) Dieterich et al. (2014); (39) Gagne et al. (2014); (40) Hambly et al. (2001); (41) Luyten (1980); (42) Monet et al. (1992); (43) Zacharias et al. (2010); (44) Roeser et al. (2010); (45) Reiners & Basri 2009; (46) Sahlmann et al. (2013); (47) Seifahrt et al. 2010; (48) Tinney et al. (1995); (49) van Altena et al. (1995); (50) Weinberger et al. (2013); Source RV measurements: (51) Reiners & Basri 2009; (52) Blake et al. 2010; (53) Seifahrt et al. 2010; (54) Bochanski et al. (2005); (55) Gálvez-Ortiz et al. (2010); (56) Mohanty & Basri (2003); (57) Schmidt et al. (2010); (58) Tanner et al. (2012); (59) Tinney & Reid (1998); (60) West et al. (2008).

Table 2. Observations

Source	Observation Date (UT)	Integration Time (s)	Airmass	Flux Calibrator	Conditions/Seeing
J0004-2058	2009 Jan 11	800	1.54	Hiltner 600	seeing ~0''.6
J0024-0158	2009 Aug 27	450	1.179	Feige 110	dry, clear, windy, seeing ~1
J0041-5621AB	2009 Aug 28	600	1.329	Feige 110	seeing ~0''.7-0''.8
J0102-3737	2008 Nov 26	600	1.18	HR 3454	seeing ~0''.8-0''.9
J0109-0343	2009 Aug 27	450	1.12	Feige 110	dry, clear, windy, seeing ~1
J0123-6921	2009 Aug 28	600	1.427	Feige 110	seeing ~0''.7
J0148-3024	2009 Aug 29	600	1.005	Feige 110	clear; seeing 0''.5
J0248-1651	2009 Aug 27	600	1.055	Feige 110	dry, clear, windy, seeing ~0''.7
J0331-3042	2009 Aug 29	300	1.009	Feige 110	clear; seeing ~0''.7
J0339-3525	2009 Aug 29	300	1.015	Feige 110	clear; in twilight; seeing ~0''.7
J0351-0052	2009 Aug 28	300	1.138	Feige 110	in twilight, seeing ~0''.7
J0500+0330	2009 Jan 06	2400	1.195	Hiltner 600	clear; seeing ~0''.75
J0517-3349	2009 Jan 06	600	1.12	Hiltner 600	clear; seeing ~0''.75
J0544-2433	2009 Jan 06	800	1.17	Hiltner 600	clear; seeing ~0''.75
J0615-0100	2009 Jan 06	2400	1.13	Hiltner 600	clear; seeing ~0''.75
J0641-4322	2011 Mar 19	900	1.03	Hiltner 600	seeing ~0''.6
J0652-2534	2009 Jan 07	2400	1.5	Hiltner 600	seeing ~1
J0707-4900	2009 Jan 08	1400	1.43	Hiltner 600	seeing ~1
J0751-2540	2009 Jan 07	1800	1.1	Hiltner 600	seeing ~1
J0812-2444	2009 Jan 07	2400	1.06	Hiltner 600	seeing ~1
J0823-4912AB	2009 Jan 07	1800	1.08	Hiltner 600	seeing ~1
J0830+0947	2009 Jan 09	450	1.39	Hiltner 600	seeing ~0''.8
J0835-0819	2009 Jan 08	2000	1.15	Hiltner 600	seeing ~0''.5
J0847-1532	2009 Jan 08	2000	1.07	Hiltner 600	seeing ~0''.5
	2009 Jan 11	2000	1.58	Hiltner 600	seeing ~0''.5
J0853-0329	2009 Jan 08	450	1.12	Hiltner 600	seeing ~0''.5
J0902+0033	2011 Mar 19	600	1.15	Hiltner 600	seeing ~0''.8-0''.9
J0909-0658	2011 Mar 19	1400	1.1	Hiltner 600	seeing ~1.2
J0921-2104	2009 Jan 09	1500	1.14	Hiltner 600	seeing ~0''.8
J0923+2340	2011 Mar 20	1500	1.69	Hiltner 600/EG 274	seeing ~0''.8
J0949+0806	2009 Mar 06	1100	1.37	GD 108	seeing ~0''.8-1
J1003-0105	2011 Mar 19	600	1.17	Hiltner 600	seeing ~1
J1004-3335	2011 Mar 19	1600	1.02	Hiltner 600	seeing ~0''.9
J1045-0149	2009 Jan 09	1800	1.45	Hiltner 600	seeing variable ~0''.75
J1048-3956	2009 Jan 09	150	1.03	Hiltner 600	seeing variable ~0''.75
J1054+1214	2009 Jan 09	600	1.34	Hiltner 600	seeing variable ~0''.75
J1055+0808	2009 Mar 06	900	1.31	GD 108	seeing ~1
J1119+0828	2011 Mar 19	600	1.37	Hiltner 600	some moon glare; seeing ~1
J1121-1313AB	2009 Jan 11	600	1.85	Hiltner 600	seeing ~0''.5
	2009 Mar 06	600	1.08	GD 108	seeing ~1
J1134+0022	2009 Mar 06	1200	1.19	GD 108	seeing ~1
J1139-3159	2009 Mar 06	1050	1.014	GD 108	seeing ~0''.7
J1155-3727	2009 Mar 06	1500	1.02	GD 108	seeing ~0''.8
J1221+0257	2009 Mar 06	1500	1.178	GD 108	seeing ~0''.6
J1224-1238	2009 Mar 06	1050	1.046	GD 108	seeing ~0''.65

Table 2—Continued

Source	Observation Date (UT)	Integration Time (s)	Airmass	Flux Calibrator	Conditions/Seeing
J1252+0252	2011 Mar 19	600	1.45	Hiltner 600	seeing ~1
J1309-2330	2009 Mar 06	450	1.005	GD 108	seeing ~0''.6
J1315-2649AB	2011 Mar 26	3000	1.003	EG 274	clear; seeing ~0''.6
J1332-0441	2009 Mar 06	600	1.097	GD 108	seeing ~0''.5
J1411-2119	2009 Mar 06	900	1.018	GD 108	seeing ~0''.5
J1422+2116	2011 Mar 19	900	1.6	Hiltner 600	seeing~ 1.5-1.6
J1440+1339	2011 Mar 19	900	1.5	Hiltner 600	seeing ~0''.7
J1456-2809	2009 Mar 06	150	1.002	GD 108	seeing ~0''.6
J1500-0039	2011 Mar 19	600	1.25	Hiltner 600	seeing~ 1.25
J1501+2250	2011 Mar 19	900	1.71	Hiltner 600	seeing ~2
J1504-2355	2009 Mar 06	450	1.004	GD 108	seeing ~0''.62
J1506+1321	2009 Mar 06	1800	1.354	GD 108	seeing ~0''.7
J1510-0241	2009 Mar 07	1050	1.13	GD 108	seeing ~0''.6
J1510-2818	2009 Mar 07	1200	1.003	GD 108	seeing ~0''.6
J1534-1418	2009 Mar 07	300	1.036	GD 108	seeing~0''.5-0''.6
J1539-0520	2011 Mar 19	1500	1.16	Hiltner 600	seeing~ 1.5-1.6
J1550+1455AB	2009 Aug 28	3600	1.47	Feige 110	seeing ~1.3
	2009 Aug 29	3600	1.471	Feige 110	clear; 0''.6-0''.9
J1553+1400	2009 Mar 08	1500	1.76	GD 108	seeing ~1
J1555-0956	2009 Mar 08	1200	1.145	GD 108	seeing ~0''.4
J1607-0442	2009 Mar 08	600	1.213	GD 108	seeing ~0''.6
J1615+0546	2009 Mar 08	1200	1.347	GD 108	seeing ~0''.7
J1645-1319	2009 Aug 29	1200	1.079	GD 108	seeing ~0''.7-0''.8
J1705-0516	2009 Mar 08	1200	1.143	Hiltner 600/EG 274	seeing ~0''.7
J1707-0558AB	2011 Mar 20	2400	1.238	Feige 110	clear; variable seeing ~0''.7
J1733-1654	2009 Aug 29	3000	1.034	Feige 110	seeing ~1.1
J1745-1640	2009 May 31	3000	1.024	EG 274	seeing ~0''.9
J1750-0016	2009 Aug 29	2700	1.334	Feige 110	clear; seeing ~1.1
J1845-6357	2009 May 31	200	1.256	EG 274	seeing ~1
J2000-7523	2009 May 31	2000	1.449	EG 274	seeing ~1
J2036+1051	2009 May 31	2950	1.351	EG 274	windy; seeing ~1.2
J2037-1137	2009 Aug 27	750	1.062	Feige 110	dry, clear and windy; seeing ~0''.75
J2045-6332	2009 Aug 27	2700	1.272	Feige 110	dry, clear and windy; seeing ~0''.7
J2104-1037	2009 Aug 27	2700	1.074	Feige 110	dry, clear and windy; seeing ~0''.9
J2120+1021	2009 Aug 29	2400	1.31	Feige 110	clear; seeing ~0''.8
J2200-3038AB	2009 Aug 29	2400	1.002	Feige 110	clear; seeing ~0''.6
J2226-7503	2009 May 31	1500	1.47	EG 274	seeing ~1
J2306-0502	2009 Aug 27	300	1.095	Feige 110	dry, clear and windy; seeing ~0''.8
J2331-2749	2009 Aug 28	450	1.03	Feige 110	seeing ~0''.9
J2337-0838	2009 Aug 27	450	1.073	Feige 110	dry, clear and windy; seeing ~0''.9
J2346+1129	2009 Aug 28	1200	1.336	Feige 110	seeing ~0''.8
J2349+1224	2009 Aug 28	900	1.336	Feige 110	seeing ~0''.9
J2351-2537	2009 Aug 28	600	1.033	Feige 110	seeing ~0''.7

Table 3. Equivalent Widths and Line Strengths of Absorption and Emission Lines

Source	SpT	Li I 6710 Å	Rb I 7802 Å	Rb I 7950 Å	Na I 8186 Å	Na I 8197 Å	Cs I 8523 Å	Cs I 8946 Å	H α 6583 Å	$\log_{10} L_{H\alpha}/L_{bol}$	ζ
J0004-2058	M9	<1.3	1.54±0.17	1.24±0.15	1.7±0.2	2.1±0.3	0.8±0.2	<0.7	-4.2±0.4	-5.04±0.06	0.973±0.018
J0024-0158	M9.5	<0.4	1.62±0.16	1.39±0.18	1.49±0.18	1.59±0.18	1.01±0.14	0.8±0.2	-0.13±0.12	-6.57±0.13	0.56±0.03
J0041-5621AB	M8	0.7±0.2	0.94±0.09	0.70±0.18	1.59±0.12	1.8±0.2	0.55±0.08	<0.7	-22±3	-4.01±0.06	1.208±0.016
J0102-3737	M9	<0.2	1.33±0.11	0.98±0.16	1.83±0.14	2.2±0.2	0.58±0.13	<1.1	-7.24±0.16	-4.76±0.06	1.030±0.004
J0109-0343	M8	<0.4	1.03±0.12	0.59±0.16	1.47±0.17	1.7±0.2	0.56±0.11	<0.9	-3.58±0.12	-4.82±0.06	1.20±0.04
J0123-6921	M9	0.56±0.17	0.93±0.09	0.62±0.13	1.40±0.10	1.66±0.18	<0.5	<0.8	-11.9±1.4	-4.51±0.06	1.28±0.03
J0148-3024	M7.5	<0.4	1.33±0.14	1.09±0.10	1.7±0.2	2.1±0.2	0.37±0.04	<0.6	-7.8±0.8	-4.40±0.06	1.052±0.008
J0248-1651	M8	<0.5	1.15±0.15	0.7±0.2	1.85±0.17	2.0±0.2	0.49±0.13	<0.9	-11.1±1.8	-4.20±0.06	1.14±0.02
J0331-3042	M9	<0.6	1.45±0.14	0.93±0.18	1.9±0.2	2.2±0.3	0.58±0.09	<0.9	-7.9±0.5	-4.72±0.06	1.138±0.015
J0339-3525	M9	0.8±0.3	1.19±0.16	0.64±0.12	1.27±0.15	1.5±0.2	0.79±0.14	<0.9	-0.9±0.2	-5.70±0.06	1.17±0.06
J0351-0052	M7.5	<1.2	0.88±0.08	0.68±0.10	1.75±0.18	1.9±0.3	0.32±0.07	<1.0	-5.8±0.2	-4.51±0.06	1.20±0.03
J0500+0330	L4	<0.9	3.8±0.5	3.4±0.4	1.18±0.15	2.0±0.3	2.5±0.2	1.6±0.2	>-1.1	<-6.5	...
J0517-3349	M8	<0.8	1.5±0.3	1.14±0.14	1.4±0.3	1.7±0.4	0.6±0.2	<1.2	-10.1±0.8	-4.34±0.06	0.863±0.015
J0544-2433	M9	<0.4	1.25±0.14	0.9±0.2	1.46±0.13	2.0±0.3	0.52±0.13	<0.8	-3.6±0.3	-5.03±0.06	1.13±0.02
J0615-0100	L1	<0.3	2.7±0.3	2.2±0.2	1.4±0.2	2.0±0.3	1.39±0.13	1.05±0.12	>-0.6	<-6.5	...
J0641-4322	L3	<1.1	3.0±0.4	2.5±0.3	1.8±0.3	2.2±0.3	1.50±0.13	1.01±0.16	>-0.8	<-6.5	...
J0652-2534	M9	0.5±0.2	1.10±0.16	0.72±0.11	1.26±0.14	1.5±0.2	0.63±0.13	<1.0	>-0.4	<-6.6	1.05±0.03
J0707-4900	M8.5	<0.7	1.5±0.2	1.03±0.13	2.0±0.2	2.1±0.3	0.71±0.14	<0.9	-1.3±0.2	-5.43±0.06	1.01±0.02
J0751-2530	L1	<0.3	2.8±0.3	1.97±0.16	1.70±0.15	2.1±0.2	1.34±0.12	1.09±0.12	>-0.3	<-6.7	...
J0812-2444	L2.5	<0.4	2.9±0.4	2.11±0.17	1.40±0.16	1.9±0.2	1.46±0.10	1.09±0.12	-1.9±0.3	-5.53±0.06	...
J0823-4912AB	L3	2.6±0.4	2.6±0.3	2.0±0.2	0.99±0.14	1.5±0.2	1.58±0.12	0.99±0.13	>-0.8	<-6.5	...
J0830+0947	M7.5	<0.4	1.04±0.11	0.9±0.2	2.0±0.2	2.3±0.3	0.58±0.09	<0.8	-19.9±1.3	-3.95±0.06	1.038±0.013
J0835-0819	L6	<0.5	3.6±0.5	3.7±0.4	1.23±0.09	1.79±0.17	2.8±0.2	1.3±0.3	>-0.5	<-7.3	...
J0847-1532	L2	<0.3	2.6±0.3	2.1±0.2	1.36±0.14	1.74±0.17	1.38±0.10	1.02±0.08	-1.02±0.18	-5.74±0.06	...
J0853-0329	M9	<0.3	1.02±0.09	0.61±0.16	1.51±0.11	1.7±0.2	0.66±0.11	<0.8	-8.8±0.2	-4.60±0.06	1.006±0.015
J0902+0033	M7	<0.6	1.05±0.10	0.77±0.18	1.77±0.11	2.2±0.3	0.37±0.11	<0.6	-5.7±0.2	-4.38±0.06	1.087±0.007
J0909-0658	L1	<1.8	2.0±0.3	1.65±0.16	1.32±0.16	1.9±0.2	1.08±0.08	0.74±0.11	-1.5±0.6	-5.64±0.07	...
J0921-2104	L1	<0.3	3.2±0.3	2.4±0.2	1.70±0.18	2.1±0.2	1.66±0.08	1.36±0.12	>-0.4	<-6.8	...
J0923+2340	L1	<1.6	2.7±0.3	2.25±0.18	1.8±0.2	2.1±0.4	1.53±0.09	1.38±0.09	-1.3±0.6	-5.63±0.07	...
J0949+0806	M8.5	<0.7	1.6±0.2	1.08±0.12	1.88±0.17	2.2±0.4	0.74±0.15	<0.7	-2.3±0.5	-5.17±0.06	1.013±0.011
J1003-0105	M8	<1.4	1.4±0.2	1.0±0.2	1.87±0.14	2.5±0.4	0.74±0.12	<0.5	-7.8±0.7	-4.50±0.06	0.974±0.016
J1004-3335	L4	<1.6	3.1±0.5	3.4±0.3	1.09±0.18	1.7±0.3	2.6±0.2	1.9±0.2	>-2	<-6.4	...
J1045-0149	L2	<0.2	2.5±0.3	1.83±0.14	1.38±0.17	1.7±0.2	1.18±0.09	0.92±0.10	-0.60±0.11	-6.00±0.06	...
J1048-3956	M8	<0.3	1.50±0.16	1.26±0.15	1.9±0.2	2.1±0.3	0.80±0.11	<0.7	-7.4±0.9	-4.52±0.06	0.947±0.004

Table 3—Continued

Source	SpT	Li I 6710 Å	Rb I 7802 Å	Rb I 7950 Å	Na I 8186 Å	Na I 8197 Å	Cs I 8523 Å	Cs I 8946 Å	H α 6583 Å	$\log_{10} L_{H\alpha}/L_{bol}$	ζ
J1054+1214	M7.5	<0.5	1.06±0.11	0.96±0.14	1.74±0.18	2.0±0.3	0.46±0.11	<0.7	-4.6±0.4	-4.56±0.06	1.014±0.008
J1055+0808	M9	<0.6	1.21±0.13	0.92±0.16	1.69±0.16	1.9±0.3	0.58±0.18	<0.6	-1.3±0.3	-5.56±0.06	0.978±0.014
J1119+0828	M7	<4	1.2±0.2	0.7±0.2	1.5±0.2	2.0±0.4	<0.4	<0.8	-1.8±0.9	-4.93±0.06	1.12±0.05
J1121-1313AB	M8.5	<0.5	1.29±0.15	1.04±0.16	1.9±0.2	2.2±0.3	0.75±0.13	<0.6	-9.4±0.4	-4.52±0.06	0.952±0.011
J1134+0022	M9	<0.8	1.19±0.13	0.70±0.13	1.74±0.14	1.9±0.2	0.57±0.11	<0.8	-14.5±0.7	-4.42±0.06	1.136±0.015
J1139-3159	M9	0.6±0.3	0.90±0.12	<0.7	0.97±0.08	0.90±0.15	<0.5	<1.3	-9.4±0.7	-4.67±0.06	1.32±0.02
J1155-3727	L3	<0.2	2.9±0.3	2.4±0.2	1.65±0.15	2.1±0.2	1.88±0.16	1.62±0.17	-2.44±0.16	-5.44±0.06	...
J1221+0257	L0	<0.5	1.7±0.2	1.27±0.14	1.52±0.16	1.8±0.3	0.95±0.10	0.7±0.2	-3.00±0.16	-5.22±0.06	...
J1224-1238	M9	<0.3	1.34±0.16	0.87±0.12	1.7±0.2	1.9±0.3	0.47±0.09	<0.8	-4.5±0.3	-4.95±0.06	1.086±0.012
J1252+0252	M7	<1.3	1.21±0.07	0.97±0.09	1.63±0.18	2.3±0.3	0.47±0.09	<0.6	-6.5±0.7	-4.44±0.06	1.07±0.03
J1309-2330	M8	<0.5	1.5±0.2	1.03±0.17	1.87±0.15	2.1±0.3	0.59±0.10	<1.0	-4.06±0.14	-4.82±0.06	1.078±0.008
J1315-2649AB	L5	<0.9	3.8±0.7	3.3±0.6	1.13±0.13	1.7±0.2	3.5±0.4	2.10±0.13	-53±20	-4.17±0.06	...
J1332-0441	M7.5	<0.4	1.22±0.13	0.83±0.18	1.76±0.18	2.0±0.3	0.39±0.11	<0.7	-7.1±0.5	-4.44±0.06	1.062±0.008
J1411-2119	M9	0.68±0.11	1.17±0.14	0.7±0.2	1.45±0.15	1.6±0.2	0.56±0.13	<0.7	-2.08±0.16	-5.31±0.06	1.123±0.009
J1422+2116	M7	<1.0	1.34±0.11	1.10±0.11	1.6±0.2	2.1±0.3	0.61±0.11	<0.6	-9.9±0.2	-4.18±0.06	0.979±0.006
J1440+1339	M7	<0.5	1.02±0.11	0.72±0.15	1.43±0.16	1.9±0.3	<0.3	<1.0	-7.4±0.2	-4.23±0.06	1.164±0.009
J1456-2809	M7	<0.5	1.27±0.13	0.90±0.13	1.8±0.2	2.1±0.3	0.44±0.08	<0.8	-5.5±0.2	-4.48±0.06	1.030±0.003
J1500-0039	M6	<0.3	0.66±0.05	0.59±0.10	1.51±0.18	1.9±0.3	<0.13	<0.5	-6.0±0.3	-4.11±0.06	1.037±0.004
J1501+2250	M9	<0.4	1.28±0.14	0.92±0.09	1.1±0.2	1.7±0.4	0.83±0.11	0.7±0.2	-3.3±0.4	-5.00±0.06	0.913±0.015
J1504-2355	M7.5	<0.5	1.18±0.14	0.91±0.12	1.8±0.2	1.9±0.3	0.52±0.10	<0.7	-4.9±0.4	-4.59±0.06	1.023±0.007
J1506+1321	L3	<0.3	3.3±0.4	2.9±0.3	1.20±0.13	1.79±0.17	2.00±0.10	1.5±0.2	-0.5±0.3	-6.11±0.06	...
J1510-0241	M9	<0.6	1.31±0.13	0.93±0.13	1.9±0.2	1.9±0.2	0.74±0.09	<0.7	-14.7±1.4	-4.38±0.06	1.020±0.011
J1510-2818	M9	1.2±0.2	1.17±0.13	<0.6	1.38±0.18	1.42±0.18	0.62±0.16	<1.2	-6.1±0.2	-4.85±0.06	1.139±0.016
J1534-1418	M8	<0.5	2.2±0.3	1.7±0.3	2.3±0.4	2.4±0.3	0.77±0.12	<0.8	-1.07±0.15	-5.20±0.06	0.982±0.005
J1539-0520	L4	<0.6	3.7±0.4	3.6±0.4	1.21±0.18	2.0±0.3	2.6±0.3	2.1±0.2	>-1.4	<-6.5	...
J1550+1455AB	L3.5	<2	2.9±0.3	2.3±0.3	1.11±0.11	1.6±0.2	1.62±0.07	1.2±0.2	>-1.8	<-6.4	...
J1553+1400	M9	<0.4	1.16±0.10	0.78±0.12	1.8±0.3	1.7±0.2	<0.5	<0.8	-5.2±0.3	-4.85±0.06	1.18±0.03
J1555-0956	L1	<0.3	2.9±0.3	2.4±0.2	1.8±0.2	2.2±0.3	1.64±0.13	1.35±0.08	-0.6±0.2	-6.00±0.06	...
J1607-0442	M9	<0.5	1.4±0.2	0.8±0.2	1.70±0.14	1.9±0.2	0.52±0.09	<0.9	-10.8±0.6	-4.58±0.06	1.119±0.011
J1615+0546	M9	<0.5	1.34±0.17	0.94±0.15	1.47±0.16	1.7±0.2	0.76±0.12	<0.8	>-0.4	<-6.7	0.982±0.014
J1645-1319	L1.5	<0.2	2.9±0.3	2.16±0.16	1.51±0.14	1.9±0.2	1.49±0.08	1.27±0.08	-2.18±0.10	-5.41±0.06	...
J1705-0516	L0.5	<0.6	2.7±0.3	1.90±0.12	1.2±0.2	1.7±0.2	1.23±0.09	1.12±0.11	>-1.0	<-6.4	...
J1707-0558AB	L0	<0.2	1.25±0.12	0.80±0.12	1.44±0.12	1.7±0.2	0.67±0.10	<0.8	-0.59±0.11	-6.00±0.06	...
J1733-1654	L0.5	<0.6	3.0±0.3	2.6±0.2	1.7±0.2	2.1±0.3	1.68±0.13	1.57±0.09	>-1.3	<-6.5	...

Table 3—Continued

Source	SpT	Li I 6710 Å	Rb I 7802 Å	Rb I 7950 Å	Na I 8186 Å	Na I 8197 Å	Cs I 8523 Å	Cs I 8946 Å	H α 6583 Å	$\log_{10} L_{H\alpha}/L_{bol}$	ζ
J1745-1640	L1.5	<0.4	2.9±0.4	2.3±0.2	1.50±0.14	2.1±0.3	1.59±0.12	1.32±0.06	-1.5±0.3	-5.10±0.06	...
J1750-0016	L5.5	<0.2	4.3±0.4	4.3±0.5	1.16±0.10	1.9±0.2	3.3±0.3	2.14±0.16	>-0.4	<-7.1	...
J1845-6357	M8.5	<0.3	1.7±0.2	1.53±0.12	1.8±0.2	2.1±0.3	0.94±0.13	<1.2	-3.2±0.2	-5.00±0.06	0.953±0.003
J2000-7523	M9	<0.8	0.9±0.3	0.67±0.15	0.86±0.11	1.1±0.2	<0.7	<0.9	-1.6±0.5	-5.53±0.06	1.40±0.03
J2036+1051	L3	<1.0	3.4±0.6	2.1±0.4	1.2±0.3	1.7±0.3	1.79±0.17	1.00±0.14	-11±3	-4.87±0.06	...
J2037-1137	M8	<0.8	1.24±0.13	0.83±0.16	1.75±0.14	2.0±0.2	0.38±0.12	<0.9	>-0.3	<-6.7	1.144±0.010
J2045-6332	M9	1.02±0.10	1.17±0.14	0.63±0.15	1.23±0.10	1.29±0.16	0.68±0.13	<1.0	-1.28±0.13	-5.52±0.06	1.17±0.02
J2104-1037	L3	<0.5	3.0±0.4	2.6±0.3	1.44±0.17	1.8±0.2	1.69±0.13	1.24±0.13	>-0.5	<-6.9	...
J2120+1021	M8	<0.5	1.6±0.2	1.43±0.10	2.0±0.2	2.2±0.3	0.91±0.14	0.6±0.2	-4.5±0.4	-4.81±0.06	0.970±0.009
J2200-3038AB	M8	<0.4	1.34±0.11	1.24±0.12	1.86±0.17	2.2±0.3	1.02±0.17	<1.1	-3.6±0.2	-4.89±0.06	1.054±0.014
J2226-7503	M8	<0.8	1.45±0.15	1.05±0.12	1.74±0.15	2.0±0.3	0.68±0.08	<0.6	-6.1±0.3	-4.56±0.06	1.030±0.011
J2306-0502	M8	<0.6	1.40±0.14	0.9±0.2	1.87±0.17	1.9±0.2	0.45±0.10	<1.0	-4.86±0.18	-4.73±0.06	1.139±0.012
J2331-2749	M7.5	<0.6	1.67±0.16	1.53±0.15	2.2±0.2	2.4±0.4	0.69±0.11	0.58±0.18	-2.25±0.13	-5.01±0.06	0.960±0.006
J2337-0838	M8	<0.5	1.14±0.13	0.80±0.16	1.69±0.14	2.0±0.3	0.44±0.08	<0.6	-9.9±0.4	-4.40±0.06	1.072±0.009
J2346+1129	M8	<0.4	1.30±0.14	0.94±0.15	1.75±0.18	2.0±0.2	0.75±0.10	<0.8	-6.7±0.5	-4.60±0.06	1.06±0.02
J2349+1224	M8	<0.3	1.45±0.18	1.1±0.2	1.8±0.2	2.1±0.3	0.55±0.17	<0.8	-3.85±0.10	-4.84±0.06	1.129±0.011
J2351-2537	M8	<0.4	1.9±0.2	1.47±0.15	1.8±0.2	2.0±0.2	1.1±0.2	0.9±0.2	-10.5±1.1	-4.36±0.06	0.83±0.02

Table 4. Mean Values of Gravity-Sensitive Indices

SpT	#	Na-a + Na-b	VO7900	TiO-b	CrH-a + FeH-a
M7	12	2.84±0.16	1.23±0.11	1.87±0.11	2.17±0.10
M8	20	2.83±0.15	1.24±0.08	2.06±0.10	2.25±0.13
M9	13	2.68±0.14	1.10±0.06	2.04±0.11	2.18±0.12
L0	4	2.47±0.09	1.04±0.14	1.5±0.2	2.7±0.3
L1	8	2.63±0.16	1.08±0.09	1.46±0.11	2.79±0.13
L2	3	2.48±0.12	1.13±0.06	1.33±0.04	2.81±0.08
L3	6	2.43±0.08	1.28±0.13	1.21±0.09	3.02±0.17
L4	3	2.441±0.018	1.37±0.09	1.20±0.08	3.40±0.08
L5	2	2.34±0.02	1.86±0.04	1.063±0.005	3.4±0.2

Table 5. Low Surface Gravity Dwarfs

Source	SpT	Na-a + Na-b		VO7900		TiO-b		CrH-a + FeH-a		Prior YMG	Ref
		Value	Low g?	Value	Low g?	Value	Low g?	Value	Low g?		
Strong Signatures of Low Surface Gravity											
J0909-0658	L1	2.28±0.03	Y?	0.86±0.010	Y?	1.52±0.02	N	2.50±0.02	Y?	N	
J1139-3159	M9 γ	2.151±0.012	Y	0.94±0.004	Y?	2.316±0.017	Y?	1.845±0.007	Y	Y	TWA 1
J1510-2818	M9	2.367±0.014	Y?	1.002±0.004	Y?	2.358±0.016	Y	2.021±0.007	Y?	Y	
J2000-7523	M9	2.183±0.013	Y	0.94±0.005	Y?	2.42±0.02	Y	1.920±0.008	Y?	N	β PMG 2, 3
J2045-6332	M9	2.222±0.009	Y	1.044±0.004	Y?	2.274±0.012	Y?	2.073±0.005	Y?	Y	β PMG 3
Weak Signatures of Low Surface Gravity											
J0041-5621AB	M8	2.385±0.011	Y?	1.282±0.005	N	2.216±0.012	Y?	2.075±0.006	N	Y	THA 2, 3
J0123-6921	M9	2.408±0.014	Y?	1.264±0.006	N	2.049±0.014	N	2.000±0.006	Y?	Y	THA 3
J0339-3525	M9	2.407±0.013	Y?	1.054±0.006	Y?	2.127±0.015	N	2.152±0.007	N	Y?	CAS,ARG 3,4
J0652-2534	M9	2.419±0.011	Y?	1.021±0.004	Y?	2.057±0.013	N	2.172±0.006	N	Y	
J0823-4912	L3	2.29±0.02	Y?	1.110±0.007	Y?	1.240±0.009	N	2.836±0.013	N	Y	
J1411-2119	M9	2.478±0.011	Y?	1.111±0.004	N	2.137±0.012	Y?	2.033±0.005	Y?	Y	

References. — (1) Gizis (2002); (2) Gálvez-Ortiz et al. (2010); (3) Gagné et al. (2014); (4) Ribas (2003).

Table 6. Radial Velocity Measurements

Source	SpT	Line Centers (km s ⁻¹)	SDSS Templates (km s ⁻¹)	MagE Standards (km s ⁻¹)	Adopted Value (km s ⁻¹)	Previous Measures (km s ⁻¹)	Ref.
J0004–2058	M9	−33±5	−26±4	−32.9±0.9	−32.9±2.2	...	
J0024–0158	M9.5	9±7	18±5	4.3±1.6	4.3±2.6	10±3	5
J0041–5621AB	M8	7±4	13±5	5.0±0.8	5.0±2.2	2.4±1.0, 7±3	3, 5
J0102–3737	M9	−2±2	4.5±1.2	−4.9±1.4	−4.9±2.4	...	
J0109–0343	M8	−6±5	2±7	−6.5±0.9	−6.5±2.2	−10.4±0.6, −7±3	3, 5
J0123–6921	M9	13±5	16±3	9.6±1.1	9.6±2.3	7.5±0.3, 11±3	3, 5
J0148–3024	M7.5	15±11	18±4	11.7±1.4	11.7±2.4	10±3	5
J0248–1651	M8	5±5	8±6	2.9±0.8	2.9±2.2	4±3	5
J0331–3042	M9	21±5	27.1±1.4	19.2±0.9	19.2±2.2	23±3	5
J0339–3525	M9	8±8	18±8	5.8±1.3	5.8±2.4	6±3	4
J0351–0052	M7.5	−13±6	−8±3	−11.4±1.0	−11.4±2.2	−15±3	5
J0500+0330 ^a	L4	9±5	...	5.1±1.8	5.1±2.7	15.94±0.16	1
J0517–3349 ^a	M8	−36±7	−26±6	−38.8±1.0	−38.8±2.2	31±3	5
J0544–2433	M9	24±6	28±3	21.1±0.9	21.1±2.2	21±3	5
J0615–0100	L1	−23±7	...	−21.0±1.0	−21.0±2.2	...	
J0641–4322	L3	70±4	...	74.4±1.4	74.4±2.4	...	
J0652–2534	M9	17±6	13±12	11.8±1.2	11.8±2.3	...	
J0707–4900	M8.5	117±10	115±18	113.4±0.8	113.4±2.2	116.4±1.5	8
J0751–2530	L1	35±6	...	32.4±1.1	32.4±2.3	...	
J0812–2444	L2.5	−6±9	...	−3.3±1.0	−3.3±2.2	...	
J0823–4912	L3	13±7	...	12.5±1.3	12.5±2.4	...	
J0830+0947	M7.5	45±6	49±2	41.2±0.9	41.2±2.2	...	
J0835–0819 ^a	L6	37±6	...	40.3±2.0	40.3±2.8	29.89±0.06, 27±2	1, 7
J0847–1532	L2	−1±8	...	−0.8±0.6	−0.8±2.1	2.02±0.10	1
J0853–0329	M9	9±5	16±5	6.7±0.9	6.7±2.2	6±3, 9.5±1.0	5, 4
J0902+0033	M7	46±5	46.7±0.6	41.2±0.8	41.2±2.2	48±5	9
J0909–0658	L1	34±5	34±13	28.6±1.1	28.6±2.3	27±3	4
J0921–2104	L1	81±8	...	80.5±1.3	80.5±2.4	80.54±0.11, 80.0±1.1	1, 7
J0923+2340	L1	−39±4	...	−31.9±0.5	−31.9±2.1	−30±4	6
J0949+0806	M8.5	17±7	25±3	16.2±1.0	16.2±2.2	...	
J1003–0105	M8	22±6	32±4	22.3±1.1	22.3±2.3	35±5	9
J1004–3335	L4	6±8	...	−7.8±1.0	−7.8±2.2	...	
J1045–0149	L2	10±8	...	10.0±1.5	10.0±2.5	6.31±0.10, 7.0±1.1	1, 7
J1048–3956	M8	−14±9	−2±7	−10.8±1.3	−10.8±2.4	−13±3	5
J1054+1214	M7.5	−6±5	−2.7±1.7	−7.3±0.9	−7.3±2.2	...	
J1055+0808	M9	5±10	8±10	5.0±0.9	5.0±2.2	19±5	9
J1119+0828	M7	−50±11	−42±7	−45.1±0.8	−45.1±2.2	−39±5	9
J1121–1313AB	M8.5	33±6	45.1±1.5	33.9±0.6	33.9±2.1	32±3	5
J1134+0022	M9	34±5	43±4	33.2±0.9	33.2±2.2	...	
J1139–3159	M9	8±7	16±12	7.0±1.1	7.0±2.3	12±2	4
J1155–3727	L3	48±8	...	46.4±1.1	46.4±2.3	45.47±0.11, 45.0±1.1	1, 7
J1221+0257	L0	−6±6	−6±4	−8.0±1.7	−8.0±2.6	−8.79±0.14, −9.0±1.4	1, 7
J1224–1238	M9	−1±7	6±4	−2.2±1.0	−2.2±2.2	−6±3	5
J1252+0252	M7	23±10	31±5	21.2±1.3	21.2±2.4	30±5	9

Table 6—Continued

Source	SpT	Line Centers (km s ⁻¹)	SDSS Templates (km s ⁻¹)	MagE Standards (km s ⁻¹)	Adopted Value (km s ⁻¹)	Previous Measures (km s ⁻¹)	Ref.
J1309–2330	M8	19±6	23±3	14.6±0.8	14.6±2.2	19±3	5
J1315–2649AB	L5	−6±10	...	−7.5±1.9	−7.5±2.8	...	
J1332–0441	M7.5	−11±5	−7.4±1.9	−12.3±0.9	−12.3±2.2	−17±3	5
J1411–2119	M9	4±14	6±11	−0.9±1.5	−0.9±2.5	−1±3	5
J1422+2116	M7	−4±7	3±5	−4.2±0.9	−4.2±2.2	...	
J1440+1339	M7	−4±6	−1±4	−5.1±1.2	−5.1±2.3	−5±3	5
J1456–2809	M7	1±5	7±5	0.9±0.9	0.9±2.2	1±3	5
J1500–0039	M6	−13±8	−10±5	−13.3±1.0	−13.3±2.2	−17±5	2
J1501+2250	M9	2±7	20±4	5.9±1.3	5.9±2.4	...	
J1504–2355	M7.5	−27±9	−23.1±1.6	−28.6±1.0	−28.6±2.2	...	
J1506+1321	L3	0±7	...	1.1±1.6	1.1±2.6	−0.68±0.11, −0.9±1.2	1, 7
J1510–0241	M9	−42±6	...	−41.4±1.1	−41.4±2.3	...	
J1510–2818	M9	−14±5	−32±3	−13.3±1.1	−13.3±2.3	...	
J1534–1418	M8	−65±11	−69±15	−70.7±1.1	−70.7±2.3	−76±3	5
J1539–0520	L4	26±7	...	26.6±3.8	26.6±4.3	27.3±0.2	1
J1550+1455AB	L3.5	13±6	...	12.9±0.6	12.9±2.1	...	
J1553+1400	M9	−51±9	−46±3	−53.3±1.1	−53.3±2.3	...	
J1555–0956	L1	14±8	...	14.9±1.0	14.9±2.2	14.84±0.10, 14.5±1.1	1, 7
J1607–0442	M9	15±9	19±4	10.8±0.9	10.8±2.2	...	
J1615+0546	M9	7±7	17±4	6.8±0.9	6.8±2.2	...	
J1645–1319	L1.5	32±13	...	27.0±0.8	27.0±2.2	26.58±0.06, 26.4±1.0	1, 7
J1705–0516	L0.5	10±7	...	11.2±2.1	11.2±2.9	12.19±0.11, 12.2±1.1	1, 7
J1707–0558AB	L0	2±2	11±5	2.9±0.9	2.9±2.2	...	
J1733–1654	L0.5	14±2	...	17.3±1.2	17.3±2.3	...	
J1745–1640	L1.5	28±9	...	26.2±1.1	26.2±2.3	...	
J1750–0016	L5.5	19±3	...	10±14	19.3±3.4	...	
J1845–6357	M8.5	−18±6	−9±3	−18.2±0.5	−18.2±2.1	...	
J2000–7523	M9	−3±22	...	8.0±1.4	8.0±2.4	11.8±1.0	3
J2036+1051	L3	18±10	...	21.5±3.2	21.5±3.8	19.7±0.5	1
J2037–1137	M8	−36±6	−33±2	−38.3±0.9	−38.3±2.2	−39±3	5
J2045–6332	M9	3±3	12±11	5.4±0.9	5.4±2.2	0.5±0.5	3
J2104–1037	L3	−25±2	...	−21.2±1.0	−21.2±2.2	−21.09±0.12, −21±2	1, 7
J2120+1021	M8	−43±9	−37±6	−42.8±0.9	−42.8±2.2	−31±5	9
J2200–3038AB	M8	−23±8	...	−24.3±1.1	−24.3±2.3	−25±0.14, −25.3±1.0	3, 7
J2226–7503	M8	18±10	27±2	16.5±0.9	16.5±2.2	15±3	5
J2306–0502	M8	−55±5	−49±2	−53.8±0.9	−53.8±2.2	−56±3, −52.80±0.16	5, 10
J2331–2749	M7.5	−4±4	0±8	−4.1±1.1	−4.1±2.3	−4±3	5
J2337–0838	M8	−10±7	−6±4	−11.5±1.2	−11.5±2.3	...	
J2346+1129	M8	−1±3	9±6	0.0±1.1	0.0±2.3	...	
J2349+1224	M8	−3±5	2±4	−3.6±0.8	−3.6±2.2	−4±3, −2.00±0.10	5, 10
J2351–2537	M8	−15±10	−5±9	−12.3±1.6	−12.3±2.6	−3.0±1.1, −10±3	7, 5

a

^aMeasured value differs by more than 3σ from previously published value(s); see Section 3.1 and 3.4.

Note. — (1) Blake et al. (2010); (2) Bochanski et al. (2005); (3) Gálvez-Ortiz et al. (2010); (4) Mohanty & Basri

(2003); (5) Reiners & Basri (2009); (6) Schmidt et al. (2010); (7) Seifahrt et al. (2010); (8) Tinney & Reid (1998);
(9) West et al. (2008); (10) Tanner et al. (2012)

Table 7. Final Radial Velocities and Heliocentric Space Motions

Source	SpT	Adopted RV (km s ⁻¹)	U (km s ⁻¹)	V (km s ⁻¹)	W (km s ⁻¹)	<i>P</i> (TD)/ <i>P</i> (D)	Population ^a
J0004–2058	M9	−33±2	−44±3	−13.1±1.5	30±2	0.04	D
J0024–0158	M9.5	4±3	10.8±0.4	21.7±1.2	7±2	0.01	D
J0041–5621AB	M8	5±2	6.5±1.0	1.5±1.3	5±2	0.01	D
J0102–3737	M9	−5±2	−67±3	−22.0±1.3	13±2	0.03	D
J0109–0343	M8	−7±2	−0.9±0.7	1.6±0.7	15±2	0.01	D
J0123–6921	M9	1±2	4.5±1.8	−5±2	5±2	0.01	D
J0148–3024	M7.5	12±2	12.3±0.8	18.3±1.2	−6±2	0.01	D
J0248–1651	M8	3±2	22.3±1.6	−4.6±1.6	±2	0.01	D
J0331–3042	M9	19±2	17.0±1.2	−9.0±1.3	−7.8±1.8	0.01	D
J0339–3525	M9	6±2	−1.9±0.8	7.8±1.2	8±2	0.01	D
J0351–0052	M7.5	−11±2	35.8±1.8	−11.2±0.7	0.2±1.5	0.01	D
J0500+0330	L4	5±3	16±2	−6.7±0.8	−4.9±1.1	0.01	D
J0517–3349	M8	−39±2	44.6±1.8	13±3	49±2	0.50	D/TD
J0544–2433	M9	21±2	41±4	−35±3	−9±2	0.02	D
J0615–0100	L1	−21±2	36±2	6±2	28±2	0.03	D
J0641–4322	L3	74±2	−55±5	−52±2	14±4	0.15	D/TD
J0652–2534	M9	12±2	−4.6±1.2	12±2	−8.1±0.5	0.01	D
J0707–4900	M8.5	113±2	−37.1±1.6	−92±2	−17.1±0.9	14.98	TD
J0751–2530	L1	32±2	−44.8±1.2	4±2	−47.1±0.8	0.30	D/TD
J0812–2444	L2.5	−3±2	30.7±1.0	7±2	11.0±0.2	0.01	D
J0823–4912AB	L3	13±2	1.1±0.2	2±2	−6.3±0.3	0.01	D
J0830+0947	M7.5	41±2	−28.9±1.7	−35±2	−21±4	0.03	D
J0835–0819	L6	40±3	−31±2	−9±2	9.2±1.4	0.01	D
J0847–1532	L2	−±2	28.2±1.0	3.5±1.8	6.5±0.6	0.01	D
J0853–0329	M9	7±2	−1.9±1.3	3.1±1.6	−9.5±1.0	0.01	D
J0902+0033	M7	41±2	−36±3	−20.2±1.5	−8±4	0.01	D
J0909–0658	L1	29±2	−18±2	−7.5±1.8	6.2±1.8	0.01	D
J0921–2104	L1	81±2	37±4	−87±3	8±2	4.90	D/TD
J0923+2340	L1	−32±2	66±4	−19±4	0±3	0.02	D
J0949+0806	M8.5	16±2	34.7±1.4	−54±2	−5.0±1.7	0.08	D
J1003–0105	M8	22±2	−30±3	−7±2	−1±3	0.01	D
J1004–3335	L4	−8±2	41±3	17±2	1.0±0.9	0.01	D
J1045–0149	L2	1±3	−20±3	−3±2	−2±2	0.01	D
J1048–3956	M8	−11±2	0.2±0.4	13±2	−21.9±0.8	0.01	D
J1054+1214	M7.5	−7±2	25±2	12±2	3±2	0.01	D
J1055+0808	M9	5±2	−10±2	−5±2	−3±2	0.01	D
J1119+0828	M7	−45±2	78±7	14±3	−30±2	0.17	D/TD
J1121–1313AB	M8.5	34±2	−15.2±0.9	−26.5±1.6	17.0±1.5	0.01	D
J1134+0022	M9	33±2	56±4	−15±2	32±2	0.07	D
J1139–3159	M9	7±2	0.9±1.6	−2±2	1.5±1.5	0.01	D
J1155–3727	L3	46±2	41.6±1.0	−36±2	−4.5±1.7	0.02	D
J1221+0257	L0	−8±3	2±3	9±3	−2±3	0.01	D
J1224–1238	M9	−2±2	−1.1±1.3	−6±2	−6±2	0.01	D
J1252+0252	M7	21±2	34±3	−16±3	14±3	0.01	D
J1309–2330	M8	15±2	27.9±1.1	−9.9±1.4	−3.6±1.4	0.01	D

Table 7—Continued

Source	SpT	Adopted RV (km s ⁻¹)	U (km s ⁻¹)	V (km s ⁻¹)	W (km s ⁻¹)	$P(\text{TD})/P(\text{D})$	Population ^a
J1315–2649AB	L5	−8±3	−41±5	−39±6	−14±3	0.03	D
J1332–0441	M7.5	−12±2	9.5±1.3	20.6±1.2	−3±2	0.01	D
J1411–2119	M9	−±3	7.9±1.8	5.9±1.3	4.5±1.6	0.01	D
J1422+2116	M7	−4±2	16.6±1.2	17.8±1.0	0±2	0.01	D
J1440+1339	M7	−5±2	18.9±1.1	−21.5±0.9	±2	0.01	D
J1456–2809	M7	±2	6.4±1.7	−14.5±1.0	−5.6±1.1	0.01	D
J1500–0039	M6	−13±2	−11±3	5.3±1.5	9±3	0.01	D
J1501+2250	M9	6±2	14.9±1.0	10.9±0.6	13±2	0.01	D
J1504–2355	M7.5	−29±2	−26±2	0±2	1.1±1.5	0.01	D
J1506+1321	L3	1±3	−28±4	−35±5	44±4	0.30	D/TD
J1510–0241	M9	−41±2	−36±2	−5.5±1.8	−5±2	0.01	D
J1510–2818	M9	−13±2	−6±2	6.9±1.1	4.2±1.0	0.01	D
J1534–1418	M8	−71±2	−66±3	−24±4	−13±2	0.03	D
J1539–0520	L4	27±4	50±3	49.0±0.8	±3	0.12	D/TD
J1550+1455AB	L3.5	13±2	45±4	9±3	−3±4	0.01	D
J1553+1400	M9	−53±2	−53±3	−41±3	11±3	0.05	D
J1555–0956	L1	15±2	65±2	13.32±0.13	−50.4±1.5	1.14	D/TD
J1607–0442	M9	11±2	33±2	−10.1±0.6	−2.3±1.3	0.01	D
J1615+0546	M9	7±2	24.4±1.8	16.6±0.7	0.000±1.6	0.01	D
J1645–1319	L1.5	27±2	44±2	−29.9±0.4	7.5±0.8	0.02	D
J1705–0516	L0.5	11±3	27±3	13.7±0.7	−1.8±1.1	0.01	D
J1707–0558AB	L0	3±2	15±2	17.7±0.8	2.1±1.0	0.01	D
J1733–1654	L0.5	17±2	30±2	15.3±1.5	0.5±1.6	0.01	D
J1745–1640	L1.5	26±2	39±2	14.0±1.5	−4.6±1.4	0.01	D
J1750–0016	L5.5	19±3	24±3	17.8±1.5	30.5±0.9	0.04	D
J1845–6357	M8.5	−18±2	−8.0±1.6	48.1±0.9	−25.1±0.8	0.15	D/TD
J2000–7523	M9	8±2	8.5±1.7	1.5±1.6	0.1±1.2	0.01	D
J2036+1051	L3	22±4	39±3	18±3	1.6±1.8	0.01	D
J2037–1137	M8	−38±2	−6.6±1.8	−33±3	14.6±1.4	0.02	D
J2045–6332	M9	5±2	1.1±1.6	−10.4±1.1	0.9±1.3	0.01	D
J2104–1037	L3	−21±2	−28.5±1.7	−19.8±1.4	−30±2	0.03	D
J2120+1021	M8	−43±2	−17±2	−25±2	12±2	0.01	D
J2200–3038AB	M8	−24±2	−32±8	−1±5	1±6	0.01	D
J2226–7503	M8	17±2	17±2	3±2	−6±2	0.01	D
J2306–0502	M8	−54±2	−32.1±1.1	−53.9±1.6	21±2	0.14	D/TD
J2331–2749	M7.5	−4±2	−15.6±1.0	57.4±1.4	10±2	0.17	D/TD
J2337–0838	M8	−12±2	−7±2	1.0±1.7	13±2	0.01	D
J2346+1129	M8	±2	50±3	23.7±1.8	11.9±1.8	0.03	D
J2349+1224	M8	−4±2	19±2	−3±2	−3±2	0.01	D
J2351–2537	M8	−12±3	−27±4	8.9±1.1	12±3	0.01	D

^aStars assigned to thin disk (D), thick disk (TD) and intermediate between thin and thick disk (D/TD) kinematic populations based on relative membership probabilities $P(\text{TD})/P(\text{D}) < 0.1$, $P(\text{TD})/P(\text{D}) > 10$ and $0.1 < P(\text{TD})/P(\text{D}) < 10$, respectively; see Section 4.1 and Bensby et al. (2003).

Table 8. Velocity Dispersions and Group Kinematic Ages

Sample	N	$\langle U \rangle$ (km s $^{-1}$)	$\langle V \rangle$ (km s $^{-1}$)	$\langle W \rangle$ (km s $^{-1}$)	σ_U (km s $^{-1}$)	σ_V (km s $^{-1}$)	σ_W (km s $^{-1}$)	σ_v (km s $^{-1}$)	Age (Gyr)	Note
All Sources	85	5.4±0.3	-4.9±0.2	1.4±0.3	31.9±0.4	25.0±0.3	15.8±0.3	43.5±0.3	4.8±0.2	Unweighted
	85				38.7±0.6	27.1±0.4	19.6±0.4	51.1±0.6	4.8±0.1	W Weighted
	65				34.4±0.4	21.2±0.4	10.7±0.4	41.8±0.5	4.3±0.2	Core
	36				27±2	34±8	26±2	52±6	8±3	Wing
$d < 20$ pc	70	2.7±0.3	-5.1±0.3	1.1±0.3	31.6±0.4	27.0±0.3	16.5±0.3	44.8±0.4	5.2±0.2	Unweighted
	70				37.7±0.5	28.6±0.4	20.3±0.3	51.5±0.4	4.9±0.1	W Weighted
	54				35.0±0.5	23.2±0.4	11.3±0.4	43.5±0.6	4.8±0.3	Core
	30				23±4	35±7	27±2	51±5	8±2	Wing
Late-M dwarfs	57	1.0±0.3	-5.1±0.3	2.1±0.3	29.7±0.5	24.0±0.2	13.8±0.3	40.6±0.4	4.0±0.2	Unweighted
	57				37.4±0.9	28.5±0.4	15.9±0.4	49.5±0.6	4.5±0.1	W Weighted
	43				28.7±0.6	19.2±0.5	11.3±0.4	36.4±0.5	2.9±0.1	Core
	24				31±3	36±7	20±3	52±5	8±2	Wing
Not Young Late-M	48	0.8±0.4	-6.5±0.3	2.0±0.3	32.3±0.5	25.8±0.3	15.0±0.3	43.9±0.4	5.0±0.2	Unweighted
	48				38.5±0.9	29.3±0.4	16.5±0.4	51.2±0.7	4.8±0.1	W Weighted
Normal Color Late-M	47	1.6±0.3	-6.5±0.3	1.3±0.3	29.8±0.6	25.1±0.3	12.6±0.3	40.9±0.5	4.0±0.2	Unweighted
	47				38.1±1.3	30.5±0.4	13.5±0.4	50.6±1.2	4.7±0.2	W Weighted
L dwarfs	28	14.7±0.5	-4.5±0.4	0.000±0.4	34.7±0.6	27.5±0.6	19.5±0.4	48.4±0.5	6.5±0.4	Unweighted
	28				42.3±0.7	24.7±0.9	24.3±0.6	54.8±0.8	5.5±0.1	W Weighted
	22				37.8±0.9	24.2±0.8	10.1±0.7	46.1±0.8	5.7±0.4	Core
	12				23±4	35±1	35±6	57±7	11±3	Wing
	11				60±2	38±2	10.3±1.4	72±2	19.1±1.8	Core $\sigma < 0$
	11				16±2	11.9±1.5	11.5±1.8	23±2	0.7±0.2	Core $\sigma > 0$
Not Young L	26	16.4±0.6	-4.6±0.5	0.0000±0.4	35.4±0.7	28.5±0.6	20.2±0.4	49.9±0.6	7.1±0.4	Unweighted
	26				43.4±0.8	25.1±0.8	24.8±0.5	55.8±0.7	5.7±0.1	W Weighted
Normal Color Late-L	16	10.1±0.8	-2.0±0.7	3.1±0.5	29.3±0.9	18.9±0.9	16.3±0.8	38.5±1.0	3.4±0.3	Unweighted
	16				34.1±1.3	23.0±1.6	19.6±1.1	45.6±1.3	3.8±0.2	W Weighted
Active L dwarfs	13	21.4±0.7	-6.0±0.8	-0.4±0.5	34.4±1.1	22.4±0.9	20.4±0.8	45.9±1.1	5.6±0.4	Unweighted
	13				43±2	24.0±1.5	27.0±1.1	55.7±1.7	5.6±0.3	W Weighted
Inactive L dwarfs	15	8.7±0.7	-3.1±0.5	0.3±0.5	35.2±0.9	32.0±0.7	19.5±0.5	51.5±0.7	7.8±0.5	Unweighted
	15				39.1±0.8	25.2±0.6	22.1±0.4	51.5±0.7	4.9±0.1	W Weighted
Unusually Red	9	-7.5±1.1	2.6±0.7	4.6±0.9	27.9±1.4	13.3±0.8	8.8±0.9	32.2±1.2	2.0±0.2	Unweighted
	9				28.4±1.3	12.0±0.7	6.3±0.6	31.3±1.2	1.6±0.2	W Weighted
Unusually Blue	11	25.6±0.9	-7.8±0.6	-5.2±0.7	40.4±1.2	38.5±0.7	24.0±0.5	60.7±0.8	12.4±0.9	Unweighted
	11				49.5±1.0	28.8±0.7	26.4±0.5	63.1±1.0	7.0±0.2	W Weighted

Table 8—Continued

Sample	N	$\langle U \rangle$ (km s $^{-1}$)	$\langle V \rangle$ (km s $^{-1}$)	$\langle W \rangle$ (km s $^{-1}$)	σ_U (km s $^{-1}$)	σ_V (km s $^{-1}$)	σ_W (km s $^{-1}$)	σ_v (km s $^{-1}$)	Age (Gyr)	Note
Lithium	9	1.1±0.5	2.0±0.5	1.7±0.5	4.8±0.5	7.2±0.5	5.6±0.4	10.4±0.5	<0.12	Unweighted
	9				4.8±0.5	6.3±0.6	4.5±0.4	9.0±0.5	<0.04	W Weighted
Low Surface Gravity	11	0.10±0.5	1.2±0.5	1.9±0.4	7.8±0.7	7.2±0.5	5.3±0.3	11.9±0.6	<0.12	Unweighted
	11				7.8±0.7	7.2±0.6	4.3±0.3	11.6±0.6	<0.05	W Weighted

Note. — Ages for Unweighted, Core and Warm populations are based on Equation 5 using the full set of parameters given in Aumer & Binney (2009). Ages for the |W|-Weighted populations are based on Equation 4 using parameters $\sigma_{v,0} = 10$ km s $^{-1}$, $\gamma_{v,p} = 1.1 \times 10^4$ (km s $^{-1}$) 3 Gyr $^{-1}$ and $T_\gamma = 5$ Gyr (Wielen 1977).

Table 9. Average Ages of Simulated Populations

β		-0.5				0.0				0.5				1.0				0.0/0.5 ^a				0.5/0.0 ^a			
Dynamic Selection ^b		No		Yes		No		Yes		No		Yes		No		Yes		No		Yes		No		Yes	
α	SpT	$\bar{\tau}$	σ_{τ}	$\bar{\tau}$	σ_{τ}	$\bar{\tau}$	σ_{τ}	$\bar{\tau}$	σ_{τ}	$\bar{\tau}$	σ_{τ}														
-0.5	M6–M9.5	1.5	1.4	1.4	1.3	3.5	2.3	3.0	2.3	6.0	1.8	5.5	2.1	6.9	0.9	6.9	1.0	5.8	2.1	5.5	2.3	3.6	2.3	3.3	2.3
	L0–L5.5	1.5	1.3	1.4	1.2	3.2	2.2	2.8	2.2	5.8	1.9	5.7	1.8	6.9	1.0	6.8	1.0	4.5	2.7	4.1	2.8	4.1	2.0	4.0	2.0
0.0	M6–M9.5	1.5	1.4	1.2	1.1	3.4	2.3	2.9	2.2	6.0	1.7	5.7	1.9	6.9	1.0	6.9	0.9	5.6	2.1	5.5	2.2	3.6	2.3	3.2	2.1
	L0–L5.5	1.4	1.3	1.3	1.2	3.1	2.2	2.6	2.1	5.7	1.9	5.5	1.9	6.8	1.1	6.8	1.0	4.4	2.7	3.9	2.8	4.0	2.0	3.6	2.0
0.5	M6–M9.5	1.5	1.4	1.4	1.3	3.4	2.3	2.8	2.2	6.0	1.8	5.7	2.1	6.9	1.0	6.9	1.1	5.6	2.2	5.2	2.4	3.5	2.3	2.9	2.2
	L0–L5.5	1.4	1.2	1.2	1.1	3.1	2.3	2.6	2.1	5.7	1.9	5.4	2.1	6.9	1.1	6.8	1.2	4.1	2.8	3.7	2.7	4.0	2.0	3.4	2.0
1.0	M6–M9.5	1.4	1.4	1.4	1.3	3.4	2.3	3.0	2.2	5.9	1.8	5.7	2.0	6.9	1.0	6.9	1.2	5.5	2.2	5.2	2.5	3.5	2.3	2.9	2.2
	L0–L5.5	1.3	1.2	1.1	1.1	2.8	2.2	2.3	2.0	5.6	2.0	5.2	2.3	6.8	1.1	6.9	1.1	3.9	2.8	3.1	2.7	3.9	2.1	3.6	1.9

^aDifferent values of β used for brown dwarfs (first number) and stars (second number).

^bRestricted to those sources whose orbits pass within 50 pc of the Sun after given initial Galactic radius and velocity components based on age-dependent dispersion functions; see Section 5.

Table 10. Candidate Members of Young Moving Groups and Associations Based on BANYAN II Analysis

Source	SpT	Moving Group	P_M	P_C	ΔD (pc)	ΔV (km s $^{-1}$)	H α	Li I	Low g	Ref.
J0041–5621AB	M6.5+M9	THA	100	<0.1	7	1.4	Y	Y	N	1,2
J0123–6921	M7.5	THA	99.9	<0.1	11	2	Y	Y	Y	2
J0339–3525	M9	ARG	17	0.3	25	13	Y	(Y) ^a	Y	2
J0823–4912	L1.5	β PMG	30	0.4	23	7	N	Y	Y	3
J1139–3159	M9 γ	TWA	99.6	0.1	21	5	Y	Y	Y	4
J1510–2818	M9	ARG	60	34	24	4	Y	N	Y	5
J2000–7523	M9	β PMG	99	4	20	2	Y	N	Y	1,2
J2045–6332	M9	β PMG	87	0.2	11	8	Y	Y	Y	1,2

^aMarginal detection in MagE data; previously reported detection in Tinney (1998) and Reiners & Basri (2009)

Note. — Moving groups and associations: ABD = AB Doradus Moving Group, ARG = Argus Association, β PMG = β Pictoris Moving Group, THA = Tucana Horologium. P_M gives the probability of membership, P_C gives the probability of field contamination.

References. — (1) Gálvez-Ortiz et al. (2010); (2) Gizis (2002); (3) Sahlmann et al. (2015); (4) Gagné et al. (2014); (5) This paper.

Table 11. Polynomial Coefficients for Magnitude Difference Relations Between MKO and 2MASS Systems

Filter	c_0	c_1	c_2	σ
J	-5.97605e-3	-1.49741e-4	-1.26157e-4	0.0078
H	-8.41293e-2	9.70498e-3	-1.58315e-4	0.0052
K_s	1.02933e-2	-3.16442e-3	7.96614e-5	0.0053

Note. — Coefficients are given for the polynomial relation MKO - 2MASS = $\sum_{i=0}^2 c_i [SpT]^i$ where SpT(M0) = 10, SpT(M5) = 15, SpT(L0) = 20, etc.

REFERENCES

- Allen, P. R., Koerner, D. W., Reid, I. N., & Trilling, D. E. 2005, *ApJ*, 625, 385
- Allers, K. N., & Liu, M. C. 2013, *ApJ*, 772, 79
- Andrei, A. H., Smart, R. L., Penna, J. L., et al. 2011, *AJ*, 141, 54
- Antoja, T., Helmi, A., Dehnen, W., et al. 2014, *A&A*, 563, A60
- Antoja, T., Monari, G., Helmi, A., et al. 2015, *ApJ*, 800, L32
- Aumer, M., & Binney, J. J. 2009, *MNRAS*, 397, 1286
- Baraffe, I., Chabrier, G., Barman, T. S., Allard, F., & Hauschildt, P. H. 2003, *A&A*, 402, 701
- Bardalez Gagliuffi, D. C., Burgasser, A. J., Gelino, C. R., et al. 2014, *ApJ*, 794, 143
- Barenfeld, S. A., Bubar, E. J., Mamajek, E. E., & Young, P. A. 2013, *ApJ*, 766, 6
- Barrado y Navascues, D. 1998, *A&A*, 339, 831
- Bartlett, J. L. 2007, PhD thesis, University of Virginia
- Basri, G., & Marcy, G. W. 1995, *AJ*, 109, 762
- Basri, G., & Reiners, A. 2006, *AJ*, 132, 663
- Bastian, N., Covey, K. R., & Meyer, M. R. 2010, *ARA&A*, 48, 339
- Benjamin, R. A. 2008, in Astronomical Society of the Pacific Conference Series, Vol. 387, Massive Star Formation: Observations Confront Theory, ed. H. Beuther, H. Linz, & T. Henning, 375
- Bensby, T., Feltzing, S., & Lundström, I. 2003, *A&A*, 410, 527
- Berger, E. 2002, *ApJ*, 572, 503
- Berger, E., Basri, G., Fleming, T. A., et al. 2010, *ApJ*, 709, 332
- Bildsten, L., Brown, E. F., Matzner, C. D., & Ushomirsky, G. 1997, *ApJ*, 482, 442
- Biller, B. A., Kasper, M., Close, L. M., Brandner, W., & Kellner, S. 2006, *ApJ*, 641, L141
- Binks, A. S., & Jeffries, R. D. 2014, *MNRAS*, 438, L11
- Binney, J., Dehnen, W., & Bertelli, G. 2000, *MNRAS*, 318, 658
- Binney, J., & Tremaine, S. 2008, Galactic Dynamics: Second Edition (Princeton University Press)
- Binney, J., Burnett, B., Kordopatis, G., et al. 2014, *MNRAS*, 439, 1231

- Blake, C. H., Charbonneau, D., & White, R. J. 2010, ApJ, 723, 684
- Blake, C. H., Charbonneau, D., White, R. J., Marley, M. S., & Saumon, D. 2007, ApJ, 666, 1198
- Bochanski, J. J., Burgasser, A. J., Simcoe, R. A., & West, A. A. 2011, AJ, 142, 169
- Bochanski, J. J., Hawley, S. L., Covey, K. R., et al. 2010, AJ, 139, 2679
- Bochanski, J. J., Hawley, S. L., Reid, I. N., et al. 2005, AJ, 130, 1871
- Bochanski, J. J., Munn, J. A., Hawley, S. L., et al. 2007a, AJ, 134, 2418
- Bochanski, J. J., West, A. A., Hawley, S. L., & Covey, K. R. 2007b, AJ, 133, 531
- Bochanski, J. J., Hennawi, J. F., Simcoe, R. A., et al. 2009, PASP, 121, 1409
- Burgasser, A. J. 2004, ApJS, 155, 191
- . 2007, ApJ, 659, 655
- . 2014, Proceedings of the 2013 International Workshop on Spectral Stellar Libraries, arXiv:1406.4887
- Burgasser, A. J.,Looper, D. L., Kirkpatrick, J. D., Cruz, K. L., & Swift, B. J. 2008, ApJ, 674, 451
- Burgasser, A. J., Melis, C., Zauderer, B. A., & Berger, E. 2013, ApJ, 762, L3
- Burgasser, A. J., Sitarski, B. N., Gelino, C. R., Logsdon, S. E., & Perrin, M. D. 2011, ApJ, 739, 49
- Burke, C. J., Pinsonneault, M. H., & Sills, A. 2004, ApJ, 604, 272
- Burrows, A., Hubbard, W. B., Lunine, J. I., & Liebert, J. 2001, Reviews of Modern Physics, 73, 719
- Caballero, J. A. 2007, ApJ, 667, 520
- Carollo, D., Beers, T. C., Lee, Y. S., et al. 2008, Nature, 451, 216
- Chabrier, G. 2003, PASP, 115, 763
- Chen, B., Stoughton, C., Smith, J. A., et al. 2001, ApJ, 553, 184
- Costa, E., Méndez, R. A., Jao, W.-C., et al. 2005, AJ, 130, 337
- . 2006, AJ, 132, 1234
- Cruz, K. L., Kirkpatrick, J. D., & Burgasser, A. J. 2009, AJ, 137, 3345
- Cruz, K. L., Reid, I. N., Liebert, J., Kirkpatrick, J. D., & Lowrance, P. J. 2003, AJ, 126, 2421

- Cruz, K. L., Reid, I. N., Kirkpatrick, J. D., et al. 2007, AJ, 133, 439
- Cushing, M. C., Rayner, J. T., & Vacca, W. D. 2005, ApJ, 623, 1115
- Dahn, C. C., Harris, H. C., Vrba, F. J., et al. 2002, AJ, 124, 1170
- Dauphole, B., & Colin, J. 1995, A&A, 300, 117
- de la Reza, R., Torres, C. A. O., Quast, G., Castilho, B. V., & Vieira, G. L. 1989, ApJ, 343, L61
- De Simone, R., Wu, X., & Tremaine, S. 2004, MNRAS, 350, 627
- Deacon, N. R., & Hambly, N. C. 2007, A&A, 468, 163
- Dehnen, W. 2000, AJ, 119, 800
- Dehnen, W., & Binney, J. J. 1998, MNRAS, 298, 387
- Delfosse, X., Tinney, C. G., Forveille, T., et al. 1999, A&AS, 135, 41
- Delorme, P., Willott, C. J., Forveille, T., et al. 2008, A&A, 484, 469
- Dieterich, S. B., Henry, T. J., Jao, W.-C., et al. 2014, AJ, 147, 94
- Douglas, S. T., Agüeros, M. A., Covey, K. R., et al. 2014, ApJ, 795, 161
- Dupuy, T. J., Liu, M. C., & Ireland, M. J. 2009a, ApJ, 692, 729
- . 2009b, ApJ, 699, 168
- . 2014, ApJ, 790, 133
- Eisenbeiss, T., Ammler-von Eiff, M., Roell, T., et al. 2013, A&A, 556, A53
- Emerson, J. P., Sutherland, W. J., McPherson, A. M., et al. 2004, The Messenger, 117, 27
- Epcstein, N., et al. 1997, The Messenger, 87, 27
- Faherty, J. K., Burgasser, A. J., Cruz, K. L., et al. 2009, AJ, 137, 1
- Faherty, J. K., Burgasser, A. J., Walter, F. M., et al. 2012, ApJ, 752, 56
- Famaey, B., Pont, F., Luri, X., et al. 2007, A&A, 461, 957
- Faure, C., Siebert, A., & Famaey, B. 2014, MNRAS, 440, 2564
- Fleming, T. A., Schmitt, J. H. M. M., & Giampapa, M. S. 1995, ApJ, 450, 401
- Gagné, J., Lafrenière, D., Doyon, R., Malo, L., & Artigau, É. 2014, ApJ, 783, 121
- . 2015, ApJ, 798, 73

- Gálvez-Ortiz, M. C., Clarke, J. R. A., Pinfield, D. J., et al. 2010, MNRAS, 409, 552
- Gálvez-Ortiz, M. C., Kuznetsov, M., Clarke, J. R. A., et al. 2014, MNRAS, 439, 3890
- Geballe, T. R., Knapp, G. R., Leggett, S. K., et al. 2002, ApJ, 564, 466
- Gilmore, G., & Reid, N. 1983, MNRAS, 202, 1025
- Gizis, J. E. 2002, ApJ, 575, 484
- Gizis, J. E., Monet, D. G., Reid, I. N., et al. 2000, AJ, 120, 1085
- Hall, P. B. 2002a, ApJ, 580, L77
- . 2002b, ApJ, 564, L89
- Hambly, N. C., Davenhall, A. C., Irwin, M. J., & MacGillivray, H. T. 2001, MNRAS, 326, 1315
- Hamuy, M., Suntzeff, N. B., Heathcote, S. R., et al. 1994, PASP, 106, 566
- Hawley, S. L., Gizis, J. E., & Reid, I. N. 1996, AJ, 112, 2799
- Haywood, M., Di Matteo, P., Lehnert, M. D., Katz, D., & Gómez, A. 2013, A&A, 560, A109
- Henry, T. J., Jao, W.-C., Subasavage, J. P., et al. 2006, AJ, 132, 2360
- Henry, T. J., Subasavage, J. P., Brown, M. A., et al. 2004, AJ, 128, 2460
- Ianna, P. A., & Fredrick, L. W. 1995, ApJ, 441, L47
- Jameson, R. F., Lodieu, N., Casewell, S. L., Bannister, N. P., & Dobbie, P. D. 2008, MNRAS, 385, 1771
- Johnson, D. R. H., & Soderblom, D. R. 1987, AJ, 93, 864
- Junqueira, T. C., Lépine, J. R. D., Braga, C. A. S., & Barros, D. A. 2013, A&A, 550, A91
- Jurić, M., Ivezić, Ž., Brooks, A., et al. 2008, ApJ, 673, 864
- Kaiser, N., Aussel, H., Burke, B. E., et al. 2002, in Society of Photo-Optical Instrumentation Engineers (SPIE) Conference Series, Vol. 4836, Society of Photo-Optical Instrumentation Engineers (SPIE) Conference Series, ed. J. A. Tyson & S. Wolff, 154–164
- Kalnajs, A. J. 1991, in Dynamics of Disc Galaxies, ed. B. Sundelius, 323
- Kastner, J. H., Zuckerman, B., Weintraub, D. A., & Forveille, T. 1997, Science, 277, 67
- Kendall, T. R., Delfosse, X., Martín, E. L., & Forveille, T. 2004, A&A, 416, L17
- Kendall, T. R., Jones, H. R. A., Pinfield, D. J., et al. 2007, MNRAS, 374, 445

- King, J. R., Villarreal, A. R., Soderblom, D. R., Gulliver, A. F., & Adelman, S. J. 2003, AJ, 125, 1980
- Kirkpatrick, J. D. 2005, ARA&A, 43, 195
- Kirkpatrick, J. D., Henry, T. J., & McCarthy, Jr., D. W. 1991, ApJS, 77, 417
- Kirkpatrick, J. D., Reid, I. N., Liebert, J., et al. 1999, ApJ, 519, 802
- . 2000, AJ, 120, 447
- Kirkpatrick, J. D., Cruz, K. L., Barman, T. S., et al. 2008, ApJ, 689, 1295
- Kirkpatrick, J. D.,Looper, D. L., Burgasser, A. J., et al. 2010, ApJS, 190, 100
- Kirkpatrick, J. D., Gelino, C. R., Cushing, M. C., et al. 2012, ApJ, 753, 156
- Knapp, G. R., Leggett, S. K., Fan, X., et al. 2004, AJ, 127, 3553
- Konopacky, Q. M., Ghez, A. M., Barman, T. S., et al. 2010, ApJ, 711, 1087
- Kraus, A. L., Shkolnik, E. L., Allers, K. N., & Liu, M. C. 2014, AJ, 147, 146
- Kuzmin, G. 1956, AZh, 27
- Lawrence, A., et al. 2007, MNRAS, 379, 1599
- Lee, K.-G., Berger, E., & Knapp, G. R. 2010, ApJ, 708, 1482
- Lépine, S., Rich, R. M., & Shara, M. M. 2007, ApJ, 669, 1235
- Liu, M. C., Dupuy, T. J., & Leggett, S. K. 2010, ApJ, 722, 311
- Lodie, N., Scholz, R.-D., McCaughrean, M. J., et al. 2005, A&A, 440, 1061
- Looper, D. L., Kirkpatrick, J. D., Cutri, R. M., et al. 2008, ApJ, 686, 528
- López-Santiago, J., Montes, D., Crespo-Chacón, I., & Fernández-Figueroa, M. J. 2006, ApJ, 643, 1160
- Luhman, K. L. 2013, ApJ, 767, L1
- Luhman, K. L., Stauffer, J. R., & Mamajek, E. E. 2005, ApJ, 628, L69
- Lutz, T. E., & Upgren, A. R. 1980, AJ, 85, 1390
- Luyten, W. J. 1980, NLTT Catalogue. Volume_III. 0_to -30_. (University of Minnesota)
- Madau, P., Pozzetti, L., & Dickinson, M. 1998, ApJ, 498, 106

- Magazzu, A., Martin, E. L., & Rebolo, R. 1993, *ApJ*, 404, L17
- Malo, L., Doyon, R., Feiden, G. A., et al. 2014, *ApJ*, 792, 37
- Mamajek, E. E. 2012, *ApJ*, 754, L20
- Mamajek, E. E., & Bell, C. P. M. 2014, *MNRAS*, 445, 2169
- Mamajek, E. E., Bartlett, J. L., Seifahrt, A., et al. 2013, *AJ*, 146, 154
- Marshall, J. L., Burles, S., Thompson, I. B., et al. 2008, in Society of Photo-Optical Instrumentation Engineers (SPIE) Conference Series, Vol. 7014, Society of Photo-Optical Instrumentation Engineers (SPIE) Conference Series
- Martin, E. L., Brandner, W., & Basri, G. 1999, *Science*, 283, 1718
- Martín, E. L., Delfosse, X., Basri, G., et al. 1999, *AJ*, 118, 2466
- McElwain, M. W., & Burgasser, A. J. 2006, *AJ*, 132, 2074
- Minchev, I., & Famaey, B. 2010, *The Astrophysical Journal*, 722, 112
- Miyamoto, M., & Nagai, R. 1975, *PASJ*, 27, 533
- Mohanty, S., & Basri, G. 2003, *ApJ*, 583, 451
- Mohanty, S., Jayawardhana, R., & Barrado y Navascués, D. 2003, *ApJ*, 593, L109
- Monet, D. G., Dahn, C. C., Vrba, F. J., et al. 1992, *AJ*, 103, 638
- Monnier, J. D., Che, X., Zhao, M., et al. 2012, *ApJ*, 761, L3
- Murphy, S. J., & Lawson, W. A. 2015, *MNRAS*, 447, 1267
- Pavlenko, Y. V., Jones, H. R. A., Martín, E. L., et al. 2007, *MNRAS*, 380, 1285
- Pérez Garrido, A., Lodieu, N., Béjar, V. J. S., et al. 2014, *A&A*, 567, A6
- Phan-Bao, N., Bessell, M. S., Martín, E. L., et al. 2008, *MNRAS*, 383, 831
- Pineda, J. S., West, A. A., Bochanski, J. J., & Burgasser, A. J. 2013, *AJ*, 146, 50
- Pirzkal, N., Burgasser, A. J., Malhotra, S., et al. 2009, *ApJ*, 695, 1591
- Quillen, A. C., Dougherty, J., Bagley, M. B., Minchev, I., & Comparetta, J. 2011, *MNRAS*, 417, 762
- Quillen, A. C., & Minchev, I. 2005, *AJ*, 130, 576
- Reid, I. N., Cruz, K. L., Kirkpatrick, J. D., et al. 2008, *AJ*, 136, 1290

- Reid, I. N., Gizis, J. E., & Hawley, S. L. 2002a, AJ, 124, 2721
- Reid, I. N., Hawley, S. L., & Gizis, J. E. 1995, AJ, 110, 1838
- Reid, I. N., Kirkpatrick, J. D., Gizis, J. E., & Liebert, J. 1999, ApJ, 527, L105
- Reid, I. N., Kirkpatrick, J. D., Liebert, J., et al. 2002b, AJ, 124, 519
- Reid, M. J., Menten, K. M., Brunthaler, A., et al. 2014, ApJ, 783, 130
- Reid, N., & Majewski, S. R. 1993, ApJ, 409, 635
- Reiners, A., & Basri, G. 2006, AJ, 131, 1806
- . 2008, ApJ, 684, 1390
- . 2009, ApJ, 705, 1416
- . 2010, ApJ, 710, 924
- Reiners, A., & Christensen, U. R. 2010, A&A, 522, A13+
- Reiners, A., Seifahrt, A., & Dreizler, S. 2010, A&A, 513, L9
- Ribas, I. 2003, A&A, 400, 297
- Roeser, S., Demleitner, M., & Schilbach, E. 2010, AJ, 139, 2440
- Ruiz, M. T., Takamiya, M. Y., & Roth, M. 1991, ApJ, 367, L59
- Sahlmann, J., Burgasser, A. J., Martín, E. L., et al. 2015, A&A, submitted
- Sahlmann, J., Lazorenko, P. F., Ségransan, D., et al. 2013, A&A, 556, A133
- Schmidt, S. J., Cruz, K. L., Bongiorno, B. J., Liebert, J., & Reid, I. N. 2007, AJ, 133, 2258
- Schmidt, S. J., West, A. A., Bochanski, J. J., Hawley, S. L., & Kielty, C. 2014, PASP, 126, 642
- Schmidt, S. J., West, A. A., Hawley, S. L., & Pineda, J. S. 2010, AJ, 139, 1808
- Scholz, R.-D. 2014, A&A, 561, A113
- Schönrich, R., Binney, J., & Dehnen, W. 2010, MNRAS, 403, 1829
- Seifahrt, A., Reiners, A., Almaghrbi, K. A. M., & Basri, G. 2010, A&A, 512, A37+
- Sellwood, J. A., & Binney, J. J. 2002, MNRAS, 336, 785
- Sharma, S., Bland-Hawthorn, J., Binney, J., et al. 2014, ApJ, 793, 51
- Siebert, A., Famaey, B., Minchev, I., et al. 2011, MNRAS, 412, 2026

- Simons, D. A., & Tokunaga, A. 2002, PASP, 114, 169
- Skrutskie, M. F., et al. 2006, AJ, 131, 1163
- Skumanich, A. 1972, ApJ, 171, 565
- Soderblom, D. R., Stauffer, J. R., MacGregor, K. B., & Jones, B. F. 1993, ApJ, 409, 624
- Spitzer, Jr., L., & Schwarzschild, M. 1953, ApJ, 118, 106
- Steinmetz, M., Zwitter, T., Siebert, A., et al. 2006, AJ, 132, 1645
- Stephens, D. C., & Leggett, S. K. 2004, PASP, 116, 9
- Stephens, D. C., Leggett, S. K., Cushing, M. C., et al. 2009, ApJ, 702, 154
- Strömgren, G. 1924, ApJ, 59, 228
- Tanner, A., White, R., Bailey, J., et al. 2012, ApJS, 203, 10
- Tinney, C. G. 1996, MNRAS, 281, 644
- . 1998, MNRAS, 296, L42+
- Tinney, C. G., & Reid, I. N. 1998, MNRAS, 301, 1031
- Tinney, C. G., Reid, I. N., Gizis, J., & Mould, J. R. 1995, AJ, 110, 3014
- Tody, D. 1986, in Society of Photo-Optical Instrumentation Engineers (SPIE) Conference Series, Vol. 627, Society of Photo-Optical Instrumentation Engineers (SPIE) Conference Series, ed. D. L. Crawford, 733—
- Tokunaga, A. T., Simons, D. A., & Vacca, W. D. 2002, PASP, 114, 180
- Toomre, A. 1964, ApJ, 139, 1217
- Torres, C. A. O., da Silva, L., Quast, G. R., de la Reza, R., & Jilinski, E. 2000, AJ, 120, 1410
- Torres, C. A. O., Quast, G. R., da Silva, L., et al. 2006, A&A, 460, 695
- Torres, C. A. O., Quast, G. R., Melo, C. H. F., & Sterzik, M. F. 2008, Young Nearby Loose Associations, ed. Reipurth, B., 757
- van Altena, W. F., Lee, J. T., & Hoffleit, D. 1995, VizieR Online Data Catalog, 1174, 0
- Walkowicz, L. M., Hawley, S. L., & West, A. A. 2004, PASP, 116, 1105
- Wegg, C., & Gerhard, O. 2013, MNRAS, 435, 1874
- Weinberger, A. J., Anglada-Escudé, G., & Boss, A. P. 2013, ApJ, 762, 118

- West, A. A., & Basri, G. 2009, ApJ, 693, 1283
- West, A. A., Bochanski, J. J., Hawley, S. L., et al. 2006, AJ, 132, 2507
- West, A. A., Hawley, S. L., Bochanski, J. J., et al. 2008, AJ, 135, 785
- West, A. A., Hawley, S. L., Walkowicz, L. M., et al. 2004, AJ, 128, 426
- West, A. A., Morgan, D. P., Bochanski, J. J., et al. 2011, AJ, 141, 97
- Wielen, R. 1977, A&A, 60, 263
- Williams, M. E. K., Steinmetz, M., Binney, J., et al. 2013, MNRAS, 436, 101
- Wilson, O. C. 1963, ApJ, 138, 832
- Wright, E. L., Eisenhardt, P. R. M., Mainzer, A. K., et al. 2010, AJ, 140, 1868
- Yoon, J., Peterson, D. M., Kurucz, R. L., & Zagarello, R. J. 2010, ApJ, 708, 71
- York, D. G., et al. 2000, AJ, 120, 1579
- Zacharias, N., Finch, C., Girard, T., et al. 2010, AJ, 139, 2184
- Zapatero Osorio, M. R., Martín, E. L., Béjar, V. J. S., et al. 2007, ApJ, 666, 1205
- Zuckerman, B., Bessell, M. S., Song, I., & Kim, S. 2006, ApJ, 649, L115
- Zuckerman, B., & Song, I. 2004, ARA&A, 42, 685
- Zuckerman, B., Song, I., & Bessell, M. S. 2004, ApJ, 613, L65
- Zuckerman, B., Song, I., Bessell, M. S., & Webb, R. A. 2001, ApJ, 562, L87
- Zuckerman, B., Vican, L., Song, I., & Schneider, A. 2013, ApJ, 778, 5
- Zuckerman, B., & Webb, R. A. 2000, ApJ, 535, 959